To the Graduate Council:

I am submitting herewith a dissertation written by Xiaoxiong Yan entitled "Engineering Model of Ash Deposition and Its Effect on Heat Transfer to Superheater Tubes" I have examined the final copy of this dissertation for form and content and recommend that it be accepted in partial fulfillment of the requirements for the degree of Doctor of Philosophy, with a major in Mechanical Engineering.

Roy J. Schulz

Roy J. Schulz, Ph. D., Major Professor

We have read this dissertation
and recommend its acceptance:

Ching-Yi Lo

Lloyd W. Crawford

K R Kimble

Accepted for the Council:

C W Minkel

Associate Vice Chancellor
and Dean of The Graduate School

Engineering Model of Ash Deposition and Its Effect on Heat Transfer to Superheater Tubes

A Dissertation

Presented for the

Doctor of Philosophy

Degree

The University of Tennessee, Knoxville

Xiaoxiong Yan

May, 1994

DEDICATION

To my grandparents, Zongying Zhang and Jici Yan

For their gracious love.

And

To my wife Qi Sun and daughter Sunny

For their love and support.

ACKNOWLEDGEMENTS

I would like to thank Dr. Roy Schulz, chairman of my dissertation committee and my committee members, Dr. Ching-Fang Lo, Dr. Lloyd Crawford and Dr. Kenneth Kimble for their valuable suggestions and assistance in improving my dissertation. I am especially grateful to Charles L. Wagoner, supervisor of my graduate research assistantship for his support throughout the development of this research. A special thanks goes out to Richard Attig, John Alan Howlett, Brad Winkleman, Bob Douglas, Douglas Jackson, Marvis White, John Dace, John Foote, and Philip Sherrill for their help.

ABSTRACT

A generally applicable theory is presented which attempts to explain how ash deposits form, with or without the presence of sticky particles and surfaces. Some experimental and modeling results are described. Ash deposition due to inertial impaction and thermophoresis was calculated. Boiler design specification, loads, coal properties, boiler operation choices, and locally-entrained ash characteristics are input in terms of superheater tube diameter, steam temperature, flue-gas temperature, particle velocity, gas and particle density, gas velocity, multiple time increments, particle diameter distributions, and dust loading with elemental analyses for multiple narrow-range particle-diameter bins plus calculated viscosity for impacting particles. The total heat flux of the superheater tube is calculated. Calculated two-dimensional deposition resulting from the inertial impaction and the resulting total heat flux are compared with measurement data from the +20MWt magnetohydrodynamic (MHD) facility at the University of Tennessee Space Institute (UTSI) and the Fuels Evaluation Facility (FEF) at the Pittsburgh Energy Technology Center (PETC). The numerical and experimental results are in the good agreement. The influence of several variables including time, tube diameter, gas velocity, particle density, particle size distribution, and dust loadings on ash deposition are discussed.

TABLE OF CONTENTS

LIST OF TABLES

LIST OF FIGURES

Figure PAGE

NOTATION

$\tilde{A}$: Stiff matrix
a: Coefficient of diffuse reflection, dimensionless
$\underline{B}$: A matrix
bin: Number of bins
C: Constant
D: Tube diameter, meter
D_i: Fick diffusion coefficient
DCM: Distribution of chemical composition
DL: Total dust loading, $kg \cdot m^{-3}$
d: Particle diameter, meter
d_i: Thickness of the ash deposition layer accumulated on segment, meter
EA: Elemental Analysis
e: Coefficient of restitution
e^h: Error
F_t: Force, N
F: Factor, dimensionless
G: Matrix
g: Gravity
H: The projection of the tube height, meter
h: Convection coefficient, $W \cdot m^{-2} K^{-1}$
h_l: Characteristic length of an element, meter
h_r: Radiation heat transfer coefficient, $W \cdot m^{-2} K^{-1}$
I: Parameter
J: Parameter
K: Thermal conductivity, $W \cdot m^{-1} K^{-1}$
L: Length of tube, meter
Le: Lewis number, dimensionless
M: Molecular weight
m: Mass of particle, kg
m: Mass flux, $kg \cdot s^{-1}$
Nu: Nusselt number, dimensionless
n: Number of nodes in finite element method
P: Matrix
Pr: Prandtl number, dimensionless
p: Pressure, $N \cdot m^{-2}$
poro: Porosity of ash deposit
Q: Matrix
q: Heat flux, $Btu \cdot ft^{-2} \cdot hr^{-1}$
R: Radius of tube, meter
Re: Reynolds number, dimensionless
r: Radius of particle, meter

SP: Staying probability
Stk: Stokes number, dimensionless
Stk_e: Generalized Stokes Number, dimensionless
s: Distance from stagnation point, meter
s_0 Penetration distance, meter
T: Temperature, K
$\underline{T}$: Matrix
t: Time, second
U_p: Particle rebound velocity, $m \cdot s^{-1}$
u: True solution in finite element method
V: Velocity, $m \cdot s^{-1}$
V_p: Particle approach velocity, $m \cdot s^{-1}$
V_∞: Free stream velocity, $m \cdot s^{-1}$
W: Weight percentage
x: x coordinates, meter
y: y coordinates, meter

Greek Symbols

ρ: Density, $kg \cdot m^{-3}$
μ: Viscosity, $m^2 \cdot s^{-1}$
α_i: Constant in test function
α_t: Thermal diffusion factor
β: Local collection efficiency
β_c: Total collection efficiency
β_v: Mean velocity in thermal equilibrium, $m \cdot s^{-1}$
β_i: Constant in test function
γ_i: Constant in test function
θ: Impacting angle
ω: Concentration
ε: Emissivity, dimensionless
ε_l: Lennard-Jones molecular interaction energy parameter
ψ: Linear interpolation functions
π: Pi
κ: Boltzmann constant, 1.3806×10^{-23} $J \cdot K^{-1}$
δ: Delta function
δ_1: Criteria of convergence
δ_2: Criteria of convergence

η: Dynamic viscosity, $N \cdot s \cdot m^{-2}$

τ_i : Thermophoretic parameter

σ_i: Lennard-Jones molecular size parameter

σ: Stefan-Boltzmann constant, 5.6696×10^{-8} $W \cdot m^{-2} \cdot K^{-4}$

Ω: Domain

Γ: Boundary

Superscript

e: Element

Subscript

g: Gas stream

p: Particle

w: Wall

∞: Free Stream

Miscellaneous Acronyms

ADP: Ash Deposition Probe

CFBL: Chemical Frozen Boundary Layer

CFFF: Coal-Fired Flow Facility

DOE: U. S. Department of Energy

FEF: Fuels Evaluation Facility

MHD: Magnetohydrodynamic System

NASA: National Aeronautics and Space Administration

PETC: Pittsburgh Energy Technology Center

SHTM: Superheater Test Module

TS: Test Section

UTSI: University of Tennessee Space Institute

CHAPTER I

GENERAL INTRODUCTION

1.1 Background

Fire-side deposition has long been recognized as a major problem in coal-fired steam generators and magnetohydrodynamic (MHD) systems. The economic losses that can be attributed directly or indirectly to the growth of ash deposition in such units are considerable, especially if these units are shut down because of ash deposition causing an extended outage for off-line cleaning or repair of damaged heat-transfer surface.

Many universities, laboratories, and energy companies have expended considerable amount of effort in understanding and predicting the behavior of coal ash deposition in these units. Empirical techniques are the traditional methods which relate laboratory and pilot-scale measurements of the fuel characteristics with the design, performance and coal ash behavior of the steam generators. Almost all empirical methods are based on experimental techniques designed to analyze coal samples and/or measure relative values of ash deposition rates. These tests are conducted in the laboratory or in pilot-scale units under conditions that cannot directly simulate the necessary wide variety of utility boiler design and operational parameters. The scaling-up process for specific commercial applications produces significant limitations and inaccuracy.

In the foreword of Erich Raask's book titled Mineral Impurities in Coal Combustion: Behavior, Problems, and Remedial Measures [1985] William T. Reid wrote:

"The state of the art in this field has been based largely on empiricism, even though science and theory have been applied in a widely varying degree. For example, determining the fusibility of coal ash, a basic property in assessing coal behavior, as done most commonly has little relation to the rheology of silicate systems. And yet this basic property of ash at high temperatures almost certainly must influence the thickness of slag on heat-receiving surfaces and so affect heat transfer. Hence, applying empirical measurements to predict the behavior of an unfamiliar coal in a given boiler furnace can be unreliable -- and often is. Yet the more technically sound methods of measuring fundamental flow characteristics of coal-ash slags have not contributed much as yet to predicting ash behavior, except under limited conditions. It has been realized for many years that ash characteristics must be related to boiler configuration and to operating conditions in assessing the likelihood of ash-related problems, yet such three-pronged studies are few, and generalized relationships are not yet available. Perhaps the growing realization that coal will be our main source of energy for generating electricity for the coming century will lend emphasis to our need for more basic information on coal-ash behavior under real-life conditions."

In order to comprise the three-pronged effort proposed by Reid, a generic engineering approach to the study of ash deposits has been defined and described by Wagoner and Wessel [1986]. The approach develops and uses calculations and measurements from several engineering disciplines and has considerably improved the demonstrated limitations for predicting coal ash behavior .

The generic engineering approach is a systematic approach unifying several engineering disciplinary activities as they pertain to ash deposits and boiler performance. This approach seeks to combine fundamental engineering relationships in a way that identifies and responds to all the key variables influencing both deposits and the process of heat transfer. The result is a generalized engineering method for quantitative measurement and calculation of the effect of fire-side deposits and soot blowing on real-time performance of heat transfer surfaces in steam generators. The generic approach is subdivided into five broad categories:

1. Characteristics of fuels
2. Characteristics of entrained particles
3. Mass transfer
4. Heat transfer
5. Deposit strength

These categories are addressed with regard to the design and the transient and cyclic nature of normal operation of the steam generator.

There are few studies on the dynamic interdependence between heat and mass transfer which describe how the deposit growth and removal processes affect local instantaneous heat absorption rates. Wagoner and Wessel [1986] presented some results for combining effects of heat and mass transfer on a single heat exchange tube. In their model, 100% particle staying probability was assumed, which means that if the particle hits the tube, it will stick to it. The local collection or target efficiency of a tube is based on the dimensions of the cylindrical tube. However, 100% particle staying probability is not always a reality for dry particles. Furthermore, as ash deposits collect on the tube surface, the resulting shape of the surface is no longer perfectly cylindrical. The local collection efficiency (local means at different points on the surface) should be dependent on the shape of ash deposits, and staying probability must be a function of time and location.

The current U.S. Department of Energy-sponsored MHD development program at The University of Tennessee Space Institute (UTSI) recently completed the design, construction and operation (Proof-of-Concept testing) of an integrated bottoming cycle heat recovery/seed recovery (HRSR) subsystem using coal as the primary fuel. As part of the general program of system design and performance analysis of the CFFF, the present dissertation research was undertaken to develop an improved procedure for predicting ash deposition characteristics and their effects on heat transfer to superheater tubes.

1.2 Objective

The goal of this project was to follow the generic engineering approach and set up a complete second generation, two-dimensional numerical model of the ash deposition process which would combine heat and mass transfer principles to predict the transient changes in the shape of ash deposits and total heat flux of heat exchange surfaces such as superheater tubes. The model expressed in a Fortran-based computer code, will be developed to predict not only the deposition of a specific fly ash in a pilot-scale furnace, but also would serve as a rational way to scale up information (site specific data) for MHD systems and conventional pulverized coal-fired steam generators at an electric utility station. Hence, applications planned for the model include engineering interpretation and site-specific scaling of data from the UTSI MHD HRSR, and predicting the deposition of fly ash in conventional pulverized coal-fired furnace for a superheater tube in a cross flow.

1.3 General Approach

The present study can be divided into three different parts, which include calculation of the flow field around a heat transfer tube, the tube mass transfer calculation, and the tube heat transfer calculation. The flow field calculated is a potential cross flow over a single vertical heat exchange tube as shown in figure 1.1*. The inertial impaction (definition in chapter 2) layer and the thermophoretic layer are included in the mass transfer calculation. After completing the mass transfer calculations, the shape of ash deposits can be determined. Heat transfer parameters (temperature distribution and total

*All figures may be found in Appendix B.

heat flux rate for superheater) are then calculated by assuming that the shape of ash deposits does not change during a short interval of time. Characteristics of the fuels and the entrained fly ash (e.g, species, concentration and particle size distribution etc) are given as input data. The thermal properties of ash deposition are not only a function of temperature, but also a function of chemical composition of the ash and the particle size distribution.

CHAPTER II

FORMATION OF ASH DEPOSITION

2.1 Introduction

The study of ash deposits on superheater tubes involves the analyses of several mechanisms. The coal ash (which may contain potassium sulfates and/or carbonates in the case of the coal-fired MHD program) may be present in the gas stream in different phases (solid, liquid or vapor) and a variety of chemical species, depending on the chemical composition of coal ash (and MHD seed) and the prevailing gas temperature. Depending on the combustion conditions, coal fly ash components may have a very wide particle size distribution range. Depending on the composition, particle density, and particle size distribution of ash components, ash particles may contact the tube via different mechanisms and at different rates.

When the ash particle is relatively large (solid particle, condensed vapor, or liquid drop with a diameter greater than 10 μm for most heat transfer tube sizes), it may fail to follow the gas streamlines around the superheater tube and thus impinge upon the tube; this mechanism is called inertial impaction. Smaller particles (diameter of 5 μm or less), in general, will be swept past the tube, but may deviate sufficiently from the streamlines to enter the boundary layer around the tube. From there, these particles may eventually hit the tube due to the mass concentration difference between the boundary layer and tube wall. If the surface is cooled, an additional driving force due to the boundary layer temperature gradient may be present giving further deposition; this mechanism is called inertially enhanced thermophoresis. If the particle's diameter is much less than 5 μm, there may be a mass transfer due to concentration and temperature differences between the gas stream and the tube surface. The concentration gradient causes Brownian diffusion, and the temperature gradient affects thermophoresis. We can thus divide the available deposition mechanisms into three main categories: impaction, inertially enhanced thermophoresis and diffusion (Brownian and thermophoretic). However, depending on the operational conditions and the configuration of the tubes, other mechanisms may exist such as eddy inertial impaction, vapor condensation, etc.

No matter which mechanism causes the ash particles to move to the surface, whether or not this results in deposition depends to a great extent on the physical nature of the ash particle and the surface on which particle hits. The theory related to how ash particles will deposit on the tube surface will be discussed in this chapter.

2.2 Background

There are two mechanisms for ash deposition due to inertial impaction.

The first mechanism considers sticky regimes (or elastic-plastic impact). Initially, when the tube is perfectly clean, only those particles which arrive at the surface in a sticky condition contribute to deposition formation. Sticky refers to the surface conditions, and not to any electrostatic charge effects. In the present work, no account is made for electrostatic particle deposition. If the surface temperature is low enough, the molten particles which stick solidify upon cooling. As the thickness of the deposit increases, the temperature at its surface may become high enough so that a few particles remain sticky even after cooling to the surface temperature. At this point the deposit becomes a much more efficient collector, because the sticky portion of its surface now collects both sticky and non-sticky particles.

In general, ash deposits due to inertial impaction create the thick ash deposit layer on the front side of the superheater tube. Often it is assumed that particles adhere to the tube surface or to the deposit only because of the sticky nature of the surfaces. There is an implied relationship that reductions in heat transfer efficiency are primarily related to the physical properties and size of the deposit produced by inertial impaction. However, a very complex situation exists in relating heat transfer rates to the type and nature of deposition. For example, for continued operation, the ash entering the steam generator must equal the ash leaving the steam generator. Therefore, the net deposition must equal zero for continued operation. Sticky particles can be assumed to have a relatively low viscosity which provides a reasonable explanation for stickiness; however, these same low viscosity particles and deposit, if present, would produce very high deposit strengths by way of extremely rapid deposit sintering (less than one second). Sintering is the process by which a granular or powdery material is fused by temperature into a simple solid. In this case, sootblowers would have great difficulty in removing the deposits and maintaining the net balance of zero for ash entering and leaving the steam generator. In other words, for normal operation, deposits must have strengths that are low enough to be controlled by soot blowing. Additionally, calculations show that significant changes in the size of a massive deposit on the leading edge of a tube can have very little effect on tube heat transfer efficiency. Whereas, conversely, calculations show that extremely thin layers of thermophoretically deposited ash can produce very major effects on heat transfer efficiency. Dry, powdery deposits have very low conductivity and emissivity values, but are usually easy to remove by sootblowing. These types of deposits are associated with the rapid and significant reductions in heat transfer rates. However, sticky particles are associated with deposits having high thermal conductivity and high emissivity values. In general, sticky particles have much less influence on heat transfer, but can severely impact the effectiveness of soot blowing and cleaning.

Deposits on furnace wall and tubes are identified as *slag* by most authors, and deposition in the radiant furnace of a pulverized coal-fired utility boiler is called *slagging.* Also deposition on superheater tubes in the convective section is usually called *fouling.* Strength is developed in the superheater fouling deposits by the process of *sintering*, as described above.

Raask [1985] summarized the general relation between the viscosity and sintering events as shown in Table 2.1. The author also gave the general relation between the sintering events and difficulties of the removal process as shown in Table 2.2. In Table 2.1, Where x is radius of the interface, assumed to be circular, r is radius of the spherical particles; x and r are defined in Figure 2.1. The magnitude of x/r which is used by Frenkel [1945] and Howlett [1994] is a function of time and viscosity.

Many references indicate that rapid and major reductions in heat transfer rates are associated with powdery deposits, even in the case of deposits with minimal thickness. Raask [1985] reported the following relationship between deposit thermal conductivity and emissivity and physical nature of the deposit in a table summarizing the work of many investigators as shown in Table 2.3.

In a normally operating steam-generation system, most heat-exchange surfaces experience deposits which can be controlled by soot blowing. Significant percentages of these surfaces may have powdery deposits with very low adhesive/cohesive strengths, which nonetheless significantly reduce heat transfer rates, especially in the case of superheater tubes during the period closely following soot blowing. As a result, the powdery deposits exert a significant influence on limiting the average heat transfer efficiency of the heat-exchange surface.

Table 2.1 Sintering and Slagging Regimes as Defined by Viscosity: Typical Bituminous Coal Ash

Event	Viscosity ($N \cdot s \cdot m^{-2}$)	Viscosity (Poise)	Temperature (K)	Temperature °F
Onset of sintering	10^9 - 10^{11}	10^{10} - 10^{12}	1200 - 1300	1700-1880
Medium-rate sintering	10^7 - 10^9	10^8 - 10^{10}	1300 - 1400	1880-2060
Rapid sintering	10^5 - 10^7	10^6 - 10^8	1400 - 1550	2060-2330
Formation of nonflowing slag	10^3 - 10^5	10^4 - 10^6	1550 - 1650	2330-2510

Table 2.2 Degree of Sintering Based on the Ratio of Neck Bond Radius to Particle Radius (x/r)

Value of x/r	Degree of sintering	Comment
0.001	Onset of sintering	The deposit with this degree of sintering on boiler tubes has no significant cohesive strength and would probably fall off under the action of gravity and boiler vibration.
0.01	Slightly sintered matrix	The deposit on boiler tubes would probably be removed by soot blowing.
0.1	Strongly sintered deposit	The deposit on boiler tubes would be difficult to remove by soot blowing.
> 0.3	Slagging	The ash particles lose their original identity and the deposit on boiler tubes cannot be removed by soot blowing.

Source: Raask, Erich, Mineral Impurities In Coal Combustion. Behavior, Problems, and Remedial Measures. Hemisphere Publishing Corporation, New York (1985).

Table 2.3 Relationship between Deposit Thermal Conductivity and Emissivity and Physical Nature of the Deposit

	submicron size particles, powdery	inertially impacted particles, sintered	inertially impacted particles, slag
thermal conductivity, $W \cdot m^{-1} \cdot K^{-1}$	0.03	1.1	3.0
emissivity	0.1-0.2	0.5-0.7	0.6-0.8

2.3 Sticky or Powdery Regimes

Characteristics of fire-side deposits can and do cover wide ranges, from molten or solidified slag to sintered ash particles to non-cohesive powders. The following illustrate several important examples of deposit characteristics.

Walsh et al. [1990] have presented an in-depth treatment of the deposition of sticky particles on a tube in cross flow operated under ultra low-viscosity slagging conditions (representing a very high gas temperature regime that does not exist in any current commercial superheater application) with the tube-metal temperature controlled at 810 K (1000 °F), the gas temperature at 1752 K (2694 °F), and the gas velocity at 15.1 $m \cdot s^{-1}$ (50 $ft \cdot s^{-1}$). Coal-ash deposits on the upstream stagnation line of the tubes were reported with a bulk density of 1100 $kg \cdot m^{-3}$. The authors described sticking probability for ash particles in their test apparatus as "zero below 1450 K and unity above 1450 K", a temperature which they concluded implied a well-defined melting point. They considered a particle with a viscosity of 8 Pa·s (80 poise) to be perfectly sticky. Most superheater tubes in commercial coal-fired boiler designs operate at gas temperatures near but below 1478 K (2200 °F). The design gas temperature is usually chosen to be significantly lower than the minimum ash-fusion temperature for the design coal.

Wessel and Wagoner [1986] made successful predictions of powdery-deposit shapes and heat-transfer effects using a value of unity (100%) for local staying probabilities for thermophoretic mass transport around the entire circumference of the superheater tube for the tests reported, even for refractory-like sorbent particles. Local staying probabilities used for inertial impaction were 100% at the upstream stagnation line of the superheater tube for all particles. A non-linear relationship was used for calculating local staying probabilities for inertial-impacted particles which gave probabilities that decreased rapidly as distance from the stagnation line increased, and finally dropped to zero at approximately 90 degrees around the circumference of the tube from the stagnation point. Their publication stressed the importance of sampling and evaluating locally-entrained fly ash rather than coal ash produced in the laboratory using ASTM ashing techniques because of major potential differences in ash quantity and quality. Experimental work was conducted by Wessel and Wagoner [1986] with a coal-fired 1.76 MWt small boiler simulator (SBS) at the Babcock & Wilcox Alliance Research Center using a cyclone burner and equipped with a simulated superheater tube and sootblower. Controlled tube-metal temperature was 839 K (1051 °F) with a gas temperature of 1468 K (2183 °F), and a gas velocity of 3.4 $m \cdot s^{-1}$ (11.2 $ft \cdot s^{-1}$). Powdery deposits on the upstream stagnation line were reported with bulk density of 660 $kg \cdot m^{-3}$ for coal only, and 521 $kg \cdot m^{-3}$ for coal with upper-furnace sorbent injection. Corresponding measurements for deposit-on-tube porosities were 0.725 and 0.814, respectively. Porosity is defined as one minus ratio of bulk density divided by true density. Bulk density for an ash sample is the ratio of ash weight and volume, and true density is particle density from measurement. Heat flux reductions of approximately 50% were observed with sorbent injection within periods of five hours between soot blowing.

Wagoner [1989] substantiated that sticky particles/surfaces were not feasible conditions for deposits which remain powdery and do not possess significant adhesive or cohesive strengths. Viscosities greater than 10^9 Pa·s (10^{10} poise) were indicated for powders.

Srinivasachar et al. [1988] conducted laboratory experiments to determine the critical particle viscosity for 28 or 53 μm particles to stick with impact velocities of 1 $m \cdot s^{-1}$. At viscosities greater than 10^8 poise, no particles deposited on the probe which utilized two diameter (0.049" and 0.125") tubes in cross flow, while at viscosities less than 10^8 poise, a constant fraction of "sticky" particles deposited on the surface of an uncooled probe. With an uncooled probe, which does not simulate a superheater heat-exchange tube, thermophoresis would not occur and impacting particles could not be decelerated in the thermophoretic layer.

Wagoner, Foote, and Attig [1990] described powdery deposits of non-sticky coal ash inside the tubes of a 200 hp fire-tube boiler converted for burning micronized coal with very high ash-fusion temperatures and 2.7% ash as-fired. Tube-metal temperature was 422 K (300 °F), and gas temperatures associated with the powdery deposits ranged from approximately 1478 K (2200 °F) to 450 K (350 °F). The thickest deposits, 7.6 mm (0.3 in) in 40 hours, occurred at gas temperatures near 644 K (700 °F).

Byers and Calvert [1969] described a non-sticky surface layer that was formed and retained by thermal forces. A photograph was presented that showed the powdery deposit on the inside wall of a tube carrying small, non-sticky, dry particles entrained in 900 °F gas with a tube wall temperature of 80 °F. They included three references to development of a dust sampler using thermal force (via thermophoresis) with essentially 100% collection efficiency for particles smaller than about 2 μm.

2.4 Non-sticky Particle Regimes

If sticky particles hit a surface, they will stay on it regardless of surface conditions unless "sandblasted" by inertial impaction of large refractory particles. However, depending on the physical nature of the surface, non-sticky particles may or may not stay. The second mechanism of ash deposits due to inertial impaction considers non-sticky particle deceleration and retention. It assumes that the sticking of particles is due to a thin coating of low viscosity material on the surface of deposit on a tube. In this case, the contact volume established on collision between a particle and the surface is determined by the thickness of the low viscosity surface layer, the diameter of the particle, and the inertia of the particle. If the layer is thick enough, the particle will be stopped.

Both inertial impaction mechanisms assume that there is a sticky substance or a thin coating of material which retains particles on the heat-transfer surface. However, these mechanisms would not apply to a clean tube without sticky particles, as described by Wagoner and Yan [1991]. The authors have developed and presented a model which shows how ash can deposit without involving sticky particles or surfaces.

Their theory of the procedure of deposition formation is divided into two steps: 1) initial deposit formation which is due to elastic particles impacting an elastic (clean) heat-transfer surface. 2) secondary deposit formation which is due to elastic particles impacting the thermophoretic dust layer. Regardless of the mechanism of mass transfer, all particles have a velocity greater than zero when they contact the surface of a heat exchanger. Therefore, if a particle is to deposit, it first must be decelerated, then subsequently be retained. Retention can be thought of as a staying probability for non-sticky particles. Also, all particles can be described in a broad sense as impacting or colliding with the external surface of the heat exchanger because their velocity exceeds zero. This description is not restricted to the inertial-impaction mass-transport mechanism, but includes other mechanisms, such as thermophoresis, as well.

It is useful to define a coefficient of restitution, *e*, for a normal impact as seen in Figure 2.2 on a tube surface by

$$e = \left| \frac{U_p}{V_p} \right|$$

where V_p is the approach velocity of the particle before impact, and U_p is the rebound velocity of the particle after impact on the same straight line. For a perfectly elastic particle collision $e = 1$, but in more realistic collisions, such as non-sticky particles colliding with a clean superheater tube surface, $e < 1$. For inelastic collisions associated with plastic or viscous-elastic sticky particles, $e < 1$. If the bodies stick together after collision, $e = 0$.

Dahneke [1971] presented a rebound theory with a discussion of adhesion energy and the coefficient of restitution. Rao and Whitby [1977, 1978] presented experimental data showing the drastic reduction in impaction efficiency for dry particles impacting on dry, solid surfaces. Ellenbecker et al. [1980] have studied the decrease in the collection efficiency of fly ash by mats of stainless steel fibers when particle kinetic energy was higher than a certain value. In both references, it is concluded that $0 < e < 1$ (as opposed to either 0 or 1). Tsai et al. [1990] proposed a model to calculate the coefficient of restitution and the critical speed in both the elastic and plastic regimes, based on the energy loss models and the energy conservation principle. However, $e = 0$ or $e = 1$ is assumed in the present research study and analytical model for impaction. Details of the effect of erosion of the powdery layer by inertial impaction remain unknown to this point and are not treated herein.

Thus, the present research assumes that perfectly sticky particles have a coefficient of restitution equal to zero (0) when contacting a clean (elastic) heat-exchange surface, and perfectly elastic particles (the ultimate case of non-sticky) have a coefficient of restitution equal to one when contacting a clean heat-exchange surface.

Table 2.4 summarizes the hypothetical mechanisms proposed in the present investigation of how powdery deposits could be formed from non-sticky particles. Table 2.5 then presents the expected results of particle to particle bonding, heat transfer, and soot blowing effectiveness for each of the particle deposition mechanisms of Table 2.4.

a. Theory for Initial Deposit Formation with Non-Sticky Particles on Clean Tube

When hot combustion gases flow over the cooling surface of a heat-exchanger tube, "thermal forces" exist due to the temperature gradient between the gas and tube surface. Waldmann [1961] has established an expression for the total force exerted on a small spherical particle with radius r and velocity V_p

$$F_t = -\frac{32\,r^2}{3\,\beta_v}\left[\left(1+\frac{\pi\,a}{8}\right)pV_p + \frac{K}{5}\frac{dT}{dr}\right] \qquad (2.1)$$

$$\beta_v = \sqrt{\frac{8\,\kappa T}{\pi\,m}} \qquad (2.2)$$

where βv is the mean velocity in thermal equilibrium, p is the pressure of gas stream, a is the coefficient of diffuse reflection, κ is Boltzmann constant, and K is the thermal conductivity. There are two types of terms in Equation 2.1: pressure and thermal terms. Assuming that particles (size less than 5 μm)

Table 2.4 Proposed Mechanisms for Particle Retention or Rebound After Contact With Operational Heat Exchanger

Contact Mode	Particle Deceleration	Reason for Retention On Tube or In Deposit
1. Large or Small Elastic Particles Impacting Sticky Deposit	Stops Via Deposit Surface Viscosity Plus Surface Tension (Wets Particle)	Deposit Surface Tension
2. Small Elastic Particles Contacting Elastic Tube Metal Surface	Stops Via Post-Impact Thermophoretic Drag after Several Rebounds	Thermophoretic Force: Initiates a Powdery Thermophoretic Layer
3. Large Elastic Particles Impacting Elastic Tube Metal Surface	Slows Slightly (Not Perfectly Elastic) and Rebounds	None
4.Large or Small Sticky Particles Impacting Elastic Tube Metal Surface	Stops Via Particle Surface Viscosity Plus Surface Tension (Wets Tube Surface)	Particle Surface Tension
5. Large Elastic Particles Impacting Powdery Deposit with a Thickness Less Than a Minimal Deceleration Penetration Thickness	Slows And Rebounds: Produces Erosion Via "Sandblasting"	None
6. Large Elastic Particles Impacting Powdery Deposit with a Thickness Greater Than a Minimal Deceleration Penetration Thickness	Stops Via Penetration Impulse Force (Apparent Impact Viscosity)	Stays if Penetration Exceeds Particle Radius Via Embedding in Powdery Thermophoretic Layer
7. Large or Small Sticky Particles Impacting Sticky Deposit	Stops Via Particle & Deposit Surface Viscosity Plus Surface Tension (Mutual Wetting)	Particle & Deposit Surface Tension

Table 2.5 Proposed Relationships Among Contact Mode, Deposit Strength, and Thermal Resistance

Contact Mode	In-Deposit Particle to Particle Bonding	Reduction in Heat Transfer Following Successful Soot Blowing	Loss of Soot Blower's Ability to Maintain Near-Clean-Tube Heat Transfer Rates
1. Large or Small Elastic Particles Impacting Sticky Deposit	Via Wetting & Sintering; Melting (Slagging) in Extreme Cases	Small to Medium Loss	Ranges From Medium to Complete Loss
2. Small Elastic Particles Contacting Elastic Tube Metal Surface	No Bonding; Thermophoretic Packing Force	Very High Loss; Very Rapid Effect	Small to Medium Loss
3. Large Elastic Particles Impacting Elastic Tube Metal Surface	No Bonding	No loss	No Loss; No Deposit Left to Clean
4.Large or Small Sticky Particles Impacting Elastic Tube Metal Surface	Very Rapid Sintering or Slagging	Small to Medium Loss	Ranges From Medium to Complete Loss
5. Large Elastic Particles Impacting Powdery Deposit: Thickness Less Than Deceleration Penetration	No Bonding	No Loss, Heat Transfer Increase	Leading Edge of Tube Cleaned Via Particle "Sandblasting"
6. Large Elastic Particles Impacting Powdery Deposit: Thickness Greater Than Deceleration Penetration	No Bonding; Thermophoretic Packing Force Transmitted From Small Particles Which Surround The Large, Embedded Particles	Small to Medium Loss	No Loss
7. Large or Small Sticky Particles Impacting Sticky Deposit	Stops Via Particle & Deposit surface Viscosity Plus Surface Tension (Mutual Wetting)	Small to Medium Loss	Ranges From Medium to Complete Loss

inside the boundary layer move forward to the tube surface with a certain velocity as in Figure 2.2 (a), the pressure force term is positive and the thermal force term is negative. It is not necessary that the particles move normally to the tube surface. With a perfectly elastic collision, the particle will rebound from the tube as in Figure 2.2 (b). After the collision, both the pressure and thermal forces are negative, resulting in the deceleration of the rebounding particles. The particles will repeat this process, but each time particle momentum and rebound distance are reduced. Based on impact-rebound calculations made for different particle sizes, using Equation (2.1), Figure 2.3 was created to show that an 1 μm particle is brought to rest more easily than a 5 μm particle, but both require less than 1.5 seconds to reach a rebound distance of less than 1 μm. Even with a perfectly elastic series of collisions and without considering other deceleration forces, it appears that the combined forces model could be an explanation for particle deceleration and deposition on a tube surface.

After the particles are stopped by series of collisions, depending on the magnitude of the thermal force, they may stay on the tube. Epstein [1929] first derived the following expression for the thermophoretic force on a spherical particle in a gas at rest in which there exists a temperature gradient

$$F_t = \frac{-9\pi r \mu^2}{\rho_g T}\left(\frac{K_g}{2K_g + K_p}\right)\frac{dT}{dr} \qquad (2.2)$$

where μ is gas viscosity, K_g is gas thermal conductivity, K_p is particle thermal conductivity and ρ_g is gas density. Calculations were made using Equation 2.2 based on typical superheater temperatures of 1422 K (2100 °F) for the gas and 866 K (1100 °F) for the tube metal. A temperature gradient of 566 K across a distance (hot combustion-gas to the cooler tube, or resulting tube-deposit thickness) of approximately 3.2 mm (171 $K \cdot mm^{-1}$, or 0.171 $K \cdot \mu m^{-1}$) would produce a thermal force equal to the gravitational force on a 5 µm Al_2O_3 particle. An 1 µm Al_2O_3 particle would only require a gradient of 7 $K \cdot mm^{-1}$, and a 0.5 µm Al_2O_3 particle could be retained with as little as 2 $K \cdot mm^{-1}$. Thus thermal force can be larger than gravitational force and can hold a small stationary particle against a heat-exchange or deposit surface.

For small particles (<5 µm) colliding with a clean tube surface, post-impact thermophoretic deceleration could occur after each of a series of perfectly elastic collisions, even though the "immediate" coefficient of restitution equalled one (1) for each collision. Rebound distance would decrease after each bounce, leading to zero velocity as seen in Figure 2.3 from Wagoner and Yan [1991]. Particles will stay on tube surface if the thermal force exceeds gravitational force. A dust layer would form and increase in thickness.

b. Theory for Secondary Deposit Formation of Non-Sticky Particles on Existing Deposit

Once small particles (<5 μm) form a thin thermophoretic layer, large particles (>10 μm) will collide with and penetrate into this layer. Deceleration could occur via a powder penetration resistance force (see comments on *impulse-force* relations in next section). If the thermophoretic layer thickness is greater than the penetration depth required for deceleration, the retention could be accomplished with the particle embedded in the thermophoretic layer. It is assumed that the penetration depth must equal or exceed the particle radius in order for retention to occur. If the deposit layer thickness is less than the deceleration penetration depth, erosion of the thermophoretic layer could occur.

The depth that a particle penetrates after colliding with the surface of a powder is related to its change in linear momentum via impulse, which is defined as the product of (deceleration) force and the (stopping) time during which the force acts on the particle. If the mass of the particle and its velocity at the moment of contact with the powder are known, the penetration depth can be measured and the average stopping force can be calculated. Conversely, the penetration depth can be measured directly in laboratory experiments. The units of impulse are N·s in the SI notation.

The deceleration force also can be viewed as a resistance to penetration. This analogy can be extended to the concept of expressing the impulse deceleration force as an apparent impact viscosity of a powder. This approach is based on the penetration depth (using a penetrometer analogy) and has merit for numerical modeling because a similar treatment can be used for slag flow viscosity and powder impact viscosity. The apparent impact viscosity of a powder can be expressed as Pa·s, dyne·s·cm^{-2} or poise, i.e. any of the units currently used to describe the viscosity of slag flow. This concept was described by Wagoner and Yan [1991].

If a sample of powder is loaded into an open container without applying a compressive force, the powder at room temperature can simulate a powder deposit layer with a temperature gradient that produces a thermophoretic force equal to gravitational force.

2.5 Experimental Measurements of Impact Penetration and the Resulting Theoretical Impact Viscosities

Ball drop experiments have been conducted at University of Tennessee Space Institute (UTSI) by Wagoner and Yan [1991] for three powders. Table 2.6 has bulk density and porosity data measured during the ball-drop tests. The steel balls used for these tests had four different diameters. Additionally, four diameters of lead balls were used. A short length of 0.25 mm diameter

Table 2.6 Physical Characteristics of Three Powders

	MHD Fly Ash	Fine Al_2O_3	Coarse Al_2O_3
True density, g·cc^{-1}	2.67	3.97	3.97
Bulk density, g·cc^{-1}	0.422	0.991	1.73
Porosity	0.83	0.75	0.56

Shakespeare OMNI-FLEX monofilament fishing line was glued to a spot on each ball to provide a convenient and inexpensive way to measure penetration depth during these preliminary experiments. For each ball, 2 to 4 drop heights were tested. At each height, the ball was dropped 6 to 10 times on previously-unaffected areas of the powder surface. Penetration depths were measured. The powder was poured into a 490 ml container in a reproducible manner without compressing or shaking. The surface was struck level with a straight edge. The container was 8.4 cm in diameter, and 9.8 cm deep. In the container, the powder was compacted by gravitational force, which as shown earlier, was likely to be less than in-deposit thermophoretic force at certain temperature gradient near the tube.

Samples included a composite MHD fly ash sample collected by the electrostatic precipitator during test LMF4-U conducted in CFFF as well as coarse and fine Al_2O_3 powders that were tested as potential candidates for Pittsburgh Energy Technology Center (PETC) Fuels Evaluation Facility (FEF) tests. Raask [1966] gave an expression for the approximate depth of penetration (s_0) of a spherical body as

$$s_0 = \frac{2\, v_p\, r^2\, \rho_p \sin\theta}{9\,\eta} \qquad (2.3)$$

where ρ_p is particle density, θ is impact angle and η is viscosity of deposit surface layer. Equation 2.3 was used to calculate impact viscosities from measured penetration depths. Figure 2.4 shows a comparison of impact viscosities (η) for MHD fly ash and fine Al_2O_3 powder. Detailed characterization of the alumina powders is included in Smouse and Wagoner [1991]. Data measured at UTSI were fitted with power curves (>0.98 correlation coefficients), and the resulting equations were used to extrapolate to particle diameters in the 10 to 100 µm range. Figure 2.5 shows a comparison of impact viscosities measured for coarse and fine Al_2O_3 powders supplied by Scott Smouse of DOE PETC. Figure 2.6 shows Leeds & Northrup Microtrac particle size measurements made at PETC for the alumina samples.

There is a strong sensitivity of the penetration distance (s_0) to particle diameter for both the impacting and imbedded particles. Table 2.7 shows the extrapolated apparent impact viscosity values for impacting alumina particles in the 10 to 100 µm size range. Although future in-situ measurements will be needed to quantify powder viscosities, the data in Table 2.7 can be used for a general examination of the feasibility of the concept. Calculated powder viscosities were used with Equation 2.3 to estimate penetration depths for impaction of alumina powders by Al_2O_3 particles having a range of six diameters and two velocities. Penetration depths for fine Al_2O_3 powder are shown in Table 2.8. Penetrations from 8 µm to 212 µm were predicted for decelerating the various particle combinations with velocities from 1,829 to 914 $cm \cdot s^{-1}$ (60 to 30 $ft \cdot s^{-1}$). The deposit thicknesses from the experimental program are reported by Smouse and Wagoner [1991]. Table 2.9 shows the lower end of the velocity range where one-diameter penetration and retention could be possible for 10 μm impacting particles.

A laboratory technique has been developed by Wagoner and Yan [1991] at UTSI to characterize powders at room-temperature in terms of impact penetration resistance. This approach could be very useful in future studies. Published equations for viscous capture of particles (via slag viscosity and surface tension) can be extended for dry powders via the concept of apparent impact viscosity. In spite of the extrapolation required from measured data obtained from large balls to small particles, the experimental method and the powder compaction characteristics developed by the single "retention" force (gravity) used in the experiments, should lead to a significant improvement in the ability to evaluate important heat-transfer effects of fire-side deposits more specifically and accurately. The concept and equations developed in this chapter will be used for the calculation of mass transfer in the next chapter.

Table 2.7 Extrapolated Impact Viscosity for Three Powders for Small Particles

Impacting Particle Diameter, μm	MHD ESP Fly-Ash Composite Sample(Poise)	Coarse Al_2O_3 Powder (Poise)	Fine Al_2O_3 Powder (Poise)
100	0.62	0.93	0.18
80	0.54	0.78	0.15
60	0.45	0.61	0.11
40	0.35	0.44	0.08
20	0.22	0.25	0.04
10	0.14	0.14	0.02

Table 2.8 Predicted Deceleration-Penetration Depths for Coarse Al_2O_3 (elastic) Particles Impacting Fine, Powdery Al_2O_3 Deposit on PETC FEF Superheater Tube

Impacting Velocity $m \cdot s^{-1}$	Impacting Al_2O_3 Particle Diameter, μm	Deceleration Penetration Depth, μm	Ratio Between Column 2 and Column 1
18.29	100	212	2.1
18.29	80	166	2.1
18.29	60	120	2.0
18.29	40	77	1.9
18.29	20	36	1.8
18.29	10	17	1.7
9.14	100	106	1.1
9.14	80	83	1.0
9.14	60	60	1.0
9.14	40	38	0.9
9.14	20	18	0.9
9.14	10	8	0.8

Table 2.9 The Lower End of the Velocity Range Where One-diameter Penetration and Retention Could be Possible

Layer	Impact Particle	Impact Particle Size (μm)	Impacting Velocity (m/s)
MHD Fly Ash	MHD Fly Ash	10	9.59
Coarse Al2O3 Powder	Al2O3	10	6.32
Fine Al2O3 Powder	Al2O3	10	1.00

CHAPTER III

CALCULATION OF MASS TRANSFER

3.1 Inertial Impaction

If we consider a dust-laden gas stream flowing uniformly along a duct in which is placed a circular cylinder, the streamlines approaching the cylinder will diverge and will in fact make no contact with the cylinder at all. However, large particles (diameter greater than approximately 5 μm) will not follow the streamlines exactly and will tend to continue in a straight path, resulting in a possible collision with the cylinder. The chance of a particle actually touching the cylinder depends on its velocity, the drag force on the particle, and its position relative to central streamline, etc. The mass of the particles collected on a surface can be expressed in terms of the collection efficiency of the surface. The total collection efficiency is the ratio of the mass of the particles collected on the cylinder to the mass of the particles contained in the volume of space swept by the cylinder. Local collection efficiency is defined as the ratio of the mass of the particle collected in a small arc (control volume) to the mass of the particle contacting the control-volume area.

Inertial impaction not only causes problems in power generation systems, but also in other industrial disciplines. The formation of ice on aircraft surfaces during flight through supercooled water droplets may also degrade both aircraft performance and operational safety. An enormous amount of research has been done to study the problems related to accretion of ice on the aircraft and ash deposits on the superheater tube. In all publications, flow is assumed to cross a single target, except for Schuh et al. [1989], who studied the ash particle motions in flow past a bank of tubes. There are tube banks instead of a single tube in the superheater; however, the single tube model is very useful for simulating the condition of a tube in the front row of a tube bank which is subject to the most severe deposition.

Brun et al. [1952] predicted the accretion of ice on a cylinder and compared the numerical results with measurement data. The calculation of the flow field was based on a circular cylinder in a uniform, potential, and incompressible flow in two dimensions and without circulation. The conventional forms of the equations for the drag force of a body in a fluid has been used for solving the particle trajectories. The authors found that the total collection efficiency is a function of the Stokes number (*Stk*) and the parameter *I*, where

$$\mathrm{Stk} = \frac{\rho_p d_p^2 V_\infty}{18 \mu_g R} \qquad (3.1)$$

$$I = \frac{\mathrm{Re}_0^2}{\mathrm{Stk}} \qquad (3.2)$$

and

$$\mathrm{Re}_0 = \frac{\rho_g d_p V_\infty}{\mu_g} \qquad (3.3)$$

Re_0 is a free-stream particle Reynolds number, ρ_p is the particle density, d_p is the particle diameter, V_∞ is the free stream gas velocity, μ_g is the gas viscosity and R is the cylinder radius. Israel and Rosner [1983] proposed the use of a generalized Stokes Number to determine the total collection efficiency. The generalized Stokes number is defined as

$$Stk_e = Stk\ F(Re_0) \tag{3.4}$$

Where $F(Re_0)$ is the non-Stokes particle drag correction factor. The authors found that the total collection efficiency is a function of the generalized Stokes number. Wessel and Righi [1988], and Wessel and Wagoner [1986] successfully predicted the ash deposits on a superheater tube by using the method described by Brun [1952] to calculate the flow field and use the generalized Stokes number to calculate the total collection efficiency. The local collection efficiency is a non-linear function of the total collection efficiency and location. Almost all methods developed for studying inertial impaction involve calculating the total collection efficiency or the local collection efficiency in terms of the parameters described earlier. Often the predictions provide an integrated, one-dimensional view of deposition. If one wants to consider a clean superheater tube and a short cumulative time period for deposit collection, the cylindrical shape limitation might not be too restrictive. However, as a deposit grows, the shape changes, and produces a significant effect on local collection efficiencies and impaction. This must be considered if one is to follow the real-time development of a deposit from a recently cleaned tube to the next cleaning (soot blowing) occurrence.

In order to predict the ash deposition due to inertial impaction in two-dimensions, the calculation of the flow field and the local collection efficiency must not only be accurate for the clean tube, but also around the irregular shape. A general procedure for this type of aerodynamic prediction for arbitrary two-dimensional shapes has been developed by NASA. Berkowitz et al. [1988] and Wright [1993] in NASA developed a method and a program, called LEWICE, which meets these requirements. The Douglas two-dimensional potential flow program developed by Hess and Smith [1967] has been incorporated in LEWICE to calculate flow field about an arbitrary body. In aeronautical applications, this is usually a wing, nose, or cowl surface. A program developed by Frost et al. [1982] is integrated into the procedure and provides for the calculation of particle trajectories from free stream up to the body surface where they are captured.

In the NASA LEWICE program, the surface of the body geometry is defined by segments joining a set of discrete body coordinates as shown in Figure 3.1. The notation *s* represents the distance along the body surface measured from the stagnation point. The value of *s* is defined as negative on the lower surface and positive on the upper surface.

In the segments joining body coordinates, the total collection efficiency defined earlier can be expressed as in Figure 3.2, and mathematically given by

$$\beta_c = \frac{y_{max}}{H} = \frac{1}{H}\int_{s_l}^{s_u} \beta \, ds \qquad (3.5)$$

where y_{max} is the vertical distance between the droplet release points of the upper and lower surface tangential trajectories, H is the forward projection of the body height, s_u and s_l are the upper and lower surface impingement limits, and ß is a local collection efficiency defined earlier and can be expressed as in Figure 3.2

$$\beta = \frac{dy_0}{ds} \qquad (3.6)$$

.

The particle trajectories and impingement points are used to establish the relationships between the particle's initial position (x_0, y_0) and the position where it impinges on the body surface, specified by the surface distance, s. The local collection efficiency is calculated by first calculating particle trajectories and producing a plot of particle release point, y_0, vs. surface impact distance, *s*. As Equation 3.4 indicates, the local collection efficiency is a function of the surface distance and can be determined by differentiating the curve with respect to *s*. The derivative at the center of each body segment is calculated by first determining the four y_0 vs. *s* points whose *s* values are closest to the *s* value of the body segment at which the local collection efficiency is desired. These four points are then fit with a quadratic polynomial using the method of least squares. The local collection efficiency at the desired s location is determined by differentiating the polynomial. The LEWICE program developed by NASA and industry personnel has been specifically developed to predict the deposition of glaze or rime ice on aerodynamic bodies. This dissertation developed a modified version of the LEWICE procedure to predict the formation of ash deposits on heat transfer tubes, depending on gas condition, tube diameter, particle sizes and chemistry, temperature, and so forth, as described in previous chapters. Therefore, except for the general method for determining local tube capture efficiencies for inertially impacting particles, the specific details for the process of deposition, including inertial impact, thermoporesis, etc., have been established in the dissertation research described herein.

If the local collection efficiency at *s* location is greater than zero, the particle will contact the surface. However, whether it stays on the surface depends on the physical natures of the particle and surface. Walsh et al, [1990] defined the sticking probabilities as

$$SP = \begin{cases} \dfrac{\eta_c}{\eta} & \text{if } \eta_c < \eta \\ 1 & \text{if } \eta_c > \eta \end{cases} \qquad (3.7)$$

where η_c is defined as a critical viscosity for the impacting particle and is equal to 8 Pa·s-1. There are many publications discussing the calculation of ash viscosity as a function of temperature and chemical composition Watt and Fereday [1969] gave an expression by using regression analysis:

$$\log(\eta) = \frac{10^7 C_1}{(T+123)^2} + C_2 \quad (3.8)$$

and

$$C_1 = 0.00835\, SiO_2 + 0.00601\, Al_2O_3 - 0.109 \quad (3.9)$$

$$W(SiO_2)+W(Al_2O_3)+W(Fe_2O_3)+W(CaO)+W(MgO)=100 \quad (3.10)$$

where *W* represents the weight percentage of the particular chemical species, and selected elemental analyses are normalized to 100%. The value of C_2 is calculated from the expression

$$C_2 = 0.0415W(SiO_2)+0.0192W(Al_2O_3)+$$
$$0.0276W(Fe_2O_3)+0.0160W(CaO)-4.92 \quad (3.11)$$

Kalmanovitch and Melvin [1991] presented a method to calculate the slag viscosity

$$\ln(\eta) = \ln(I) + \ln(T) + \frac{1000\,J}{T} \quad (3.12)$$

where *J* is determined from chemical composition, and

$$\ln(I) = -(0.2812\,J + 11.8279) \quad (3.13)$$

Both references used regression analysis based on the elemental analysis and viscosity measurement by using the rotational viscometer at temperature above 2000 °F. However, the references have no experimental data showing the relationship between elemental analysis and viscosity at low temperatures (1100 °F to 2000 °F) which represents superheater tube metal surface or deposit surface temperatures. Both equations underestimate the viscosity value at the low temperature range. Figure 3.3 shows the measurement of slag viscosity for MHD test and numerical data by using equation 3.9.

In the present research, the staying probability is defined for UTSI MHD test and PETC test as:

$$SP = \begin{cases} 0. & \text{if } \eta_c < \eta \\ 1. & \text{if } \eta_c > \eta \end{cases} \qquad (3.14)$$

If the particle viscosity is greater than the critical viscosity, the particle is sticky, and *SP*=1 regardless of the physical nature of the surface. If the particle viscosity is less than the critical viscosity, the particle is non-sticky, and whether it stays in site or not depends on its interaction with the deposition layer. A value of the critical viscosity of Kalmanovitch and Melvin [1991] is used currently in the UTSI model calculation, however other values can be input as appropriate. In order to calculate the penetration depth, two parameters must be calculated: the surface layer viscosity and the impact angle. Since there is no better correlation between the viscosity and elemental analysis, the surface layer viscosity is still calculated by using Equation 3.6, even if it underestimates the viscosity at low temperature range.

However, this calculation gave good results for tubes at the TS1 and CS1 locations at UTSI MHD test facility. It is very important that the relationship between the viscosity and elemental analysis be developed by experiment in low temperature range, in a future study. After the calculation of the surface layer viscosity, it must be determined whether the surface layer is sintered material or powder. If the surface layer viscosity is greater than the critical viscosity, the layer is considered to be powdery, and the extrapolated equations developed in Chapter II are used to calculate the viscosity. If the surface layer viscosity is less than the critical viscosity, the layer is considered to be sintered and current viscosity is used for the layer. The particle trajectories and the target surface are used to establish the relationship between impact angle (θ) and the position where the particle impinges on the surface, specified by x and y. The curve of the particle trajectories near the surface is calculated by using a cubic spline fit. The tangents of two curves at the impingement point are calculated by differentiating the curves of the target surface and the particle trajectory at the impingement point with respect to x. The difference between the two derivatives is the impacting angle (θ). After calculating the impact angle and layer viscosity for each surface or body element, Equation 2.3 is used to calculate the penetration distance. If the deposition layer thickness is greater than or equal to the impacting particle diameter and the penetration distance is less than deposition layer thickness, staying probability is set equal to one. Otherwise the staying probability is equal to zero.

The local ash accumulation rate ($\dot{m}$) on each surface element can be expressed as

$$\dot{m} = \sum_{i=1}^{bin} \beta_i \, SP_i \, W_i \, DL \, V_\infty \, \Delta A \qquad (3.15)$$

Where *bin* is the number of bins, W_i is weight percentage of the particular bin, β_i is the local collection efficiency for the particular bin, SP_i is staying probability of each bin, ΔA is the surface area of the element, and DL is the total dust loading. The distribution of a chemical composition (*DCM*) in each surface element or deposit surface layer element is defined as .

$$DCM^j = \sum_{i=1}^{bin} SP_i \, W_i \, (EA_i)^j \, \frac{\beta_i}{\beta_c} \qquad (3.16)$$

where superscript *j* represents the chemical composition, *EA* is the weight percentage of the particular species for the particular bin (original data are from ash elemental analysis) and βc is the total collection efficiency for multiple bins, which is defined as

$$\beta_c = \sum_{n=1}^{n} \beta_i \, SP_i \, W_i \qquad (3.17)$$

The distribution of the chemical composition (*DCM*) is used to calculate the surface layer viscosity for the deposition process at the next time step. Table

3.1 shows a typical case for coal only. Table 3.1, Equation 3.16 and Equation 3.17 are used for the calculation of β_c and DCM . β_c is equal to 0.36 and *DCM* is equal to 20%.

Table 3.1 Information for the Calculation of DCM

Bin	1	2	3
Particle Size (μm)	9.	6.	4.5
Species	SiO_2	SiO_2	SiO_2
Weight percentage of each bin, W	40%	40%	20%
Weight percentage of Species, EA	18%	22%	24%
Collection efficiency, β_i	0.5	0.4	0
Sticky probabilities, SP_i	1	1	0

This ash deposit growth rate must be interpreted as the thickness of the ash deposition accretion on the surface of the geometry. The thickness of the ash deposition layer accumulated on a particular segment is given by the equation

$$d_i = \frac{\dot{m}\,\Delta t}{\rho_p\,\Delta A\left(1.-\text{poro}\right)} \tag{3.18}$$

where ρ_p is the true density of the impacting particles, ΔA is the surface area of element, Δt is a time increment specified by the user and *poro* is the porosity of ash deposits.

The new ash deposition surface is formed by adding the ash deposition thickness, d_i, in the direction perpendicular to each segment. The adjacent end points of each of these new segments are then averaged to obtain the new coordinates describing the ash deposition surface.

3.2 Diffusion

If a chemical species *i* and air flow over a surface and the concentration of species *i* at the surface differs from that in the free stream, a concentration boundary layer will develop. Fick's law is used to find mass transfer due to the concentration boundary layer;

$$\dot{m}_i = -D_i \rho \, \nabla \omega_i \tag{3.19}$$

Where D_i is the Fick diffusion coefficient for species *i* transported in the prevailing mixture, and ω_i is the local mass fraction of species *i*. ρ is density of the prevailing mixture.

If there is a temperature boundary layer due to a cool tube surface, the submicron particles will move toward the surface due to the "driving force"- $\nabla(\ln T)$. Rosner [1983] expressed the mass transfer rate due to the temperature and concentration boundary layers as

$$\dot{m}_i = -D_i \, \rho \left(\nabla \omega_i + \alpha_t \, \omega_i \, \nabla(\ln T) \right) \tag{3.20}$$

where α_t is thermal diffusion factor.

Both numerical calculations and experimental measurements demonstrate that submicron particle deposition rates (diameter < 5 μm) can be increased by orders of magnitude as the result of temperature gradients. Rosner [1984] conducted an experiment to show that the ash deposition rate of 0.7 μm MgO particles decreased to zero, if the ratio of the wall temperature and the free stream gas temperature approached 1. Rosner [1984] calculated the mass transfer rate for a gas with 10 $m \cdot s^{-1}$ velocity and 1200 K temperature over a 5 cm diameter tube at a temperature of 800 K. The mass flow rate due to the temperature gradient was 200 times greater than the rate due to Brownian diffusion for 0.1 μm particles. Rosner et al. [1983], Gökoglu et al. [1984], and Srivastava et al. [1979] discussed the effects of thermophoresis for small particles.

Rosner et al. [1978, 1979], Gökoglu et al. [1984], and Fred et al. [1979] have studied the deposition of Na_2SO_4 from combustion gases both theoretically and experimentally with consideration of the multicomponent "chemical frozen" boundary layer (CFBL). The following equation was used to calculate the mass flux due to the diffusion.

$$\dot{m}_j = \frac{1}{2}\frac{M_j}{M} F(turb) \sum_{i=1}^{N_Q} \frac{D_i \rho}{L} F(Soret)\, Nu_{m_i} \left\{ \left(\omega_{i,\infty} - \omega_{i,w}\right) - \tau_i \frac{F(ncp)}{F(soret)}\, \omega_{i,w} \right\} \qquad (3.21)$$

Where *F(soret), F(ncp), and F(turb)* are correction factors for thermophoresis, non-constant properties across the mass transfer boundary layer, and free-stream turbulence, respectively. The subscript *j* represents Na_2SO_4, M_j is molecular weight of Na_2SO_4, M is mixture molecular weight, τ_i is a thermophoretic parameter, L is the tube length, and Nu_{mj} is a mass transfer Nusselt number, i representing the specific Na carrier, and No representing the number of Na carriers. Authors considered four different Na carriers: Na_2SO_4, $NaOH$, Na , and $NaCl$. Gŏkoglu et al. [1984] developed the NASA lew143 program for the mass transfer rate calculation of heavy molecular due to thermophoresis.

The CFBL analysis for species thermal deposition was developed and applied to UTSI MHD test results and to PETC test results. The modified CFBL program applied to species Na_2SO_4, K_2SO_4, $CaCO_3$, Fe_2O_3, and Al_2O_3. Five Na carriers assumed are Na_2SO_4, $NaOH$, Na, $NaCl$ and Na_2CO_3. Four K carriers assumed are K, KOH, K_2CO_3, and K_2SO_4. Four Fe carriers assumed are Fe, FeO, Fe_3O_4 and Fe_2O_3 Four Al carriers assumed are AlO, Al_2O, $AlOH$, and Al_2O_3. Equation 3.18 is still used, but it is applied for multicomponent deposition, where now the subscript j represents Na_2SO_4, K_2SO_4, $CaCO_3$, Fe_2O_3 or Al_2O_3, respectively.

The thermophoretic parameter (τ_i) was introduced by Gŏkoglu et al. [1984] to include the effect of thermal diffusion in mass transfer. The thermophoretic parameter (τ_i) is a function of the thermal diffusion factor (α_t), Lewis number (Le), and gas and tube surface temperatures. Rosner et al. [1980] gave information about the thermal diffusion factor (α_t) for a number of species.

In order to calculate the Fick diffusion coefficient (D_i) and thermal diffusion factor (α_t), the Lennard-Jones molecular interaction energy (well-depth) parameter (ε_l) for the species and Lennard-Jones molecular size parameter (σ_l) must be obtained. Svehla [1962] provided ε_l/κ and σ_l data for a number of species, where κ is the Boltzmann constant. He also gave some methods to calculate ε_l/κ and σ_l for different species. All molecular weights and melting points for any chemical composition are from Weast's CRC Handbook of Chemistry and Physics (CRC) [1987]. The mole fractions of the species corresponding with the gas and wall temperatures are obtained by using the NASA General Chemical Equilibrium Program (NASA SP-273) of Gordon et al. [1971].

Since the accretion of the deposition layer due to diffusion is very thin (usually 1 mm or less in a very long operation time), the thermophoretic layer does not affect the shape of the surface. However, we have to consider the effects of the thermophoretic layer in the calculation of heat transfer and impacting particle penetration.

CHAPTER IV

CALCULATION OF HEAT TRANSFER

4.1 Introduction

The models and procedures developed for the prediction of ash deposits on the superheater tube have been discussed in the previous chapter. There are many references concerning the deposition process, but there is little discussion in the literature about the total heat flux lost due to ash deposits on the superheater tube. Only Wagoner and Wessel [1986] gave numerical results by using a finite difference scheme and constant thermal properties in each domain. There are two difficulties in obtaining numerical results, the first due to irregular ash deposit shape and the second due to variable thermal properties. In order to overcome these difficulties, a finite element method has been developed and applied in this research to calculate temperature distribution and total heat flux of representative superheater tubes at the specific time during deposition periods.

4.2 Finite Element Method

As mentioned in the previous chapters, we consider a hot gas in cross flow over a single tube as shown in Figure 4.1. The tube surface, which may or may not be clean, exchanges heat with the gas by radiation and forced convection. The steam inside the tube is at a very high temperature and pressure. Typical operating practice allows fluctuation of ± 5 K in the superheated steam outlet temperature, so we can assume constant temperature over the inside tube surface. Because of the steam flow inside the tube there is a steam-side fouling build up (scale) which resists heat transfer. The following assumptions are proposed for the heat transfer model:

1. Steady state heat transfer
2. Three conduction layers (ash, tube and steam-side scale)
3. Constant temperature over the inside tube surface
4. Convection and radiation on the outside tube surface
5. No heat generation inside ash deposit, tube and steam-side scale
6. Neglect the thermal contact resistance between solid materials

Under these assumptions, the differential equation governing the heat conduction in the cartesian coordinate system can be written as

$$\frac{\partial}{\partial x}\left(K\frac{\partial T}{\partial x}\right)+\frac{\partial}{\partial y}\left(K\frac{\partial T}{\partial y}\right)=0 \qquad (4.1)$$

with boundary conditions

$$T = \text{Constant} \qquad \text{on surface 1} \qquad (4.2\ a)$$

$$K_n\frac{\partial T}{\partial n}+h\,(T-T_\infty)+\sigma\,\varepsilon\,(T^4-T_\infty^4)=0 \qquad \text{on surface 2} \qquad (4.2\ b)$$

where T is the temperature, σ is Stefan-Boltzmann constant, ε is the emissivity, h is convection heat transfer coefficient, K is the thermal conductivity and K_n is the thermal conductivity in a direction normal to the surface. The thermal conductivities are functions of temperature, location, porosity (or degree of sintering), and chemical compositions

$K = K_1(x,y,T)$	inside ash deposits
$K = K_2(T)$	inside metal tube
$K = K_3(T)$	inside steam-side scale

Since the thermal conductivity of ash is dependent on the chemical composition and temperature, and it varies with location, K_1 is function of location and temperature. Thermal conductivities of the metal tube and the steam-side scale are just a function of the local temperature.

Since there is a T^4 term in the boundary condition, the Equation 4.2 b is non linear. In order to define a linear equation for the boundary condition on the surface 2, we define a radiation heat transfer coefficient h_r as

$$h_r = \sigma \varepsilon (T^2 + T_\infty^2)(T + T_\infty) \tag{4.3}$$

Then the boundary condition on surface 2 can be written as

$$K_n \frac{\partial T}{\partial n} + h(T - T_\infty) + h_r (T - T_\infty) = 0 \tag{4.4}$$

We multiply Equation 4.1 with a test function υ (assumed to be differentiable once with respect to x,y) and integrate over the whole domain.

This gives the variational form of Equation 4.1 as

$$0 = \iint_{\Omega} (K \frac{\partial \upsilon}{\partial x}\frac{\partial T}{\partial x} + K \frac{\partial \upsilon}{\partial y}\frac{\partial T}{\partial y})\, d_x d_y + \int_{\Gamma} \upsilon\, (h + h_r)(T - T_{\infty})\, d_S \quad (4.5)$$

The symbol Ω denotes the whole domain, and Γ denotes its boundary.

Suppose that T is approximated by the expression,

$$T = \sum_{i=1}^{n} \psi_i T_i \qquad (4.6)$$

where T_i are the values of T at the points (x_i, y_i), ψ_i are linear interpolation functions and n represents the number of nodes of each element. For the three-node element as shown in Figure 4.2, T can be expressed as

$$T(x,y) = c_1 + c_2\, x + c_3\, y \qquad (4.7)$$

The equation must satisfy the nodal conditions, and

$$\begin{aligned} T(x,y) &= T_i & &\text{at } (x=x_i,\ y=y_i) \\ T(x,y) &= T_j & &\text{at } (x=x_j,\ y=y_j) \qquad (4.8) \\ T(x,y) &= T_k & &\text{at } (x=x_k,\ y=y_k) \end{aligned}$$

This leads to the linear system of equations

$$\begin{bmatrix} T_i \\ T_j \\ T_k \end{bmatrix} = \begin{bmatrix} 1 & x_i & y_i \\ 1 & x_j & y_i \\ 1 & x_k & y_k \end{bmatrix} \begin{bmatrix} c_1 \\ c_2 \\ c_3 \end{bmatrix} \qquad (4.9)$$

The solution of Equations 4.9 yields

$$c_1 = \frac{1}{2\,\Delta A}\left((x_j\, y_k - x_k\, y_j)\, T_i + (x_k\, y_i - x_i\, y_k)\, T_j + (x_i\, y_j - x_j\, y_i)\, T_k\right) \tag{4.10 a}$$

$$c_2 = \frac{1}{2\,\Delta A}\left((y_j - y_k) T_i + (y_k - y_i) T_j + (y_i - y_j) T_k\right) \tag{4.10 b}$$

$$c_3 = \frac{1}{2\,\Delta A}\left((x_j - x_k) T_i + (x_k - x_i) T_j + (x_i - x_j) T_k\right) \tag{4.10 c}$$

Where ΔA is the area of the triangle element given by

$$\Delta A = \frac{1}{2}\begin{vmatrix} 1 & x_i & y_i \\ 1 & x_j & y_j \\ 1 & x_k & y_k \end{vmatrix} \tag{4.11}$$

i, j and *k* are not equal and permute in a natural order as shown in Figure 4.2. Note that the nodes are numbered counterclockwise.

Substituting for c_1, c_2 and c_3 from Equation. 4.10 into Equation 4.7, we obtain

$$T(x,y) = T_1\,\psi_1 + T_2\,\psi_2 + T_3\,\psi_3 = \sum_{i=1}^{3} T_i\,\psi_i^{(e)} \tag{4.12}$$

where ψ_i are the linear interpolation functions for the three-node triangular element and can be written as

$$\psi_i^{(e)} = \frac{1}{2\,\Delta A}(\alpha_i + \beta_i\, x + \gamma_i\, y) \qquad i=1,2,3 \tag{4.13}$$

where

$$\alpha_i = (x_j\, y_k - x_k y_j) \quad (4.13\ a)$$

$$\beta_i = (y_j - y_k) \quad (4.13\ b)$$

$$\gamma_i = (x_k - x_j) \quad (4.13\ c)$$

The interpolation functions have following property

$$\psi_i(x_j, y_j) = \delta_{ij} \quad (4.14\ a)$$

$$\sum_{i=1}^{3} \psi_i = 1 \quad (4.14\ b)$$

Substituting $T = \Sigma\ \psi_i T_i$ and $\upsilon = \psi_i$ into the variation form equation 4.5 for every element gives

$$(Q^{(e)} + G^{(e)})\ \vec{T}^{(e)} = P^{(e)} \quad (4.15)$$

where

$$Q_{ij}^{(e)} = \iint_{\Omega^{(e)}} \left(K \frac{\partial \psi_i}{\partial x} \frac{\partial \psi_j}{\partial x} + K \frac{\partial \psi_i}{\partial y} \frac{\partial \psi_j}{\partial y} \right) dx\, dy \quad (4.16)$$

$$G_{ij}^{(e)} = (h^{(e)} + h_r^{(e)}) \int_{\Gamma^e} \psi_i\, \psi_j\, ds \quad (4.17)$$

$$P_i^{(e)} = (h^{(e)} + h_r^{(e)}) \int_{\Gamma^e} \psi_i\, T_\infty\, ds \quad (4.18)$$

Substituting the Equation 4.13 into Equations 4.16, 4.17 and 4.18 , we obtain

$$Q^{(e)} = \frac{1}{4\, \Delta A} \iint_{\Omega^{(e)}} \begin{bmatrix} \beta_i & \gamma_i \\ \beta_j & \gamma_j \\ \beta_k & \gamma_k \end{bmatrix} \begin{bmatrix} K & 0 \\ 0 & K \end{bmatrix} \begin{bmatrix} \beta_i & \beta_j & \beta_k \\ \gamma_i & \gamma_j & \gamma_k \end{bmatrix} dx\, dy \quad (4.19)$$

$$Q^{(e)} = \frac{K}{4\,\Delta A}\begin{bmatrix} \beta_i\beta_i & \beta_i\beta_j & \beta_i\beta_k \\ \beta_i\beta_j & \beta_j\beta_j & \beta_j\beta_k \\ \beta_i\beta_k & \beta_j\beta_k & \beta_k\beta_k \end{bmatrix} + \frac{K}{4\,\Delta A}\begin{bmatrix} \gamma_i\gamma_i & \gamma_i\gamma_j & \gamma_i\gamma_k \\ \gamma_i\gamma_j & \gamma_j\gamma_j & \gamma_j\gamma_k \\ \gamma_i\gamma_k & \gamma_j\gamma_k & \gamma_k\gamma_k \end{bmatrix} \quad (4.20)$$

The integral in $G^{(e)}$ and $P^{(e)}$ depends on the edge which lies on the heat flux boundary surface. If the edge ij is on the boundary surface, then

$$G^{(e)} = (h^{(e)} + h_r^{(e)}) \int_{s_i}^{s_j} \begin{bmatrix} \psi_i\psi_i & \psi_i\psi_j & 0 \\ \psi_i\psi_j & \psi_j\psi_j & 0 \\ 0 & 0 & 0 \end{bmatrix} ds \quad (4.21\text{ a})$$

$$P^{(e)} = (h^{(e)} + h_r^{(e)})\, T_\infty \int_{s_i}^{s_j} \begin{bmatrix} \psi_i \\ \psi_j \\ 0 \end{bmatrix} ds \quad (4.21\text{ b})$$

where s_i and s_j are the location of nodes i and j respectively. Tao [1985] gives the integral of Equation 4.21 as

$$\int_{s_i}^{s_j} \psi_i\psi_i \, ds = \frac{s_{ij}}{3} \qquad \text{if } i = j \quad (4.22\text{ a})$$

$$\int_{s_i}^{s_j} \psi_i\psi_j \, ds = \frac{s_{ij}}{6} \qquad \text{if } i \neq j \quad (4.22.\text{b})$$

$$\int_{s_i}^{s_j} \psi_i \, ds = \frac{s_{ij}}{2} \quad (4.22.\text{c})$$

$$\int_{s_i}^{s_j} \psi_j \, ds = \frac{s_{ij}}{2} \tag{4.22.d}$$

where s_{ij} is the length of the edge *ij*, and

$$G^{(e)} = \frac{(h^{(e)} + h_r^{(e)}) s_{ij}}{6} \begin{bmatrix} 2 & 1 & 0 \\ 1 & 2 & 0 \\ 0 & 0 & 0 \end{bmatrix} \tag{4.23 a}$$

$$P^{(e)} = \frac{(h^{(e)} + h_r^{(e)})}{2} \begin{vmatrix} 1 \\ 1 \\ 0 \end{vmatrix} \tag{4.23 b}$$

If the edge *ik* lies on the boundary surface s2 (instead of the edge ij), the matrices *G* and *P* would be given by

$$G^{(e)} = \frac{(h^{(e)} + h_r^{(e)}) s_{ik}}{6} \begin{bmatrix} 2 & 0 & 1 \\ 0 & 0 & 0 \\ 1 & 0 & 2 \end{bmatrix} \tag{4.24 a}$$

$$P^{(e)} = \frac{(h^{(e)} + h_r^{(e)}) s_{ik}}{2} \begin{vmatrix} 1 \\ 0 \\ 1 \end{vmatrix} \tag{4.24 b}$$

If the edge *jk* lies on the boundary surface s2 (instead of the edge ij), the matrices *G* and *P* would be given by

$$G^{(e)} = \frac{(h^{(e)} + h_r^{(e)}) s_{jk}}{6} \begin{bmatrix} 0 & 0 & 0 \\ 0 & 2 & 1 \\ 0 & 1 & 2 \end{bmatrix} \tag{4.25 a}$$

$$P^{(e)} = \frac{(h^{(e)} + h_r^{(e)}) s_{jk}}{2} \begin{bmatrix} 0 \\ 1 \\ 1 \end{bmatrix} \tag{4.25 b}$$

Equations (4.16) for every element yields the linear system

$$\sum_{e=1}^{E} \left([K^{(e)}] + [H^{(e)}] \right) T^{(e)} = \sum_{e=1}^{E} P^{(e)} \qquad (4.26)$$

or

$$\tilde{A}\,\underline{T} = \underline{B}$$

Where E is number of elements, $\tilde{A}$ is n by n matrix, $\underline{T}$ and $\underline{B}$ are 1 by n matrices, and n is the number of nodes. Before solving this linear system, we have to impose the essential boundary condition on the inner steam side surface. If node k lies on boundary surface 1, T_k = a known constant , and we have

$$a_{kk} = 1$$

$$b_k = T_k$$

$$b_i = b_i - a_{ik} T_k$$

$$a_{ik} = a_{ki} = 0$$

where

$$i=1,2,\ldots\ldots,k-1,k+1,\ldots.,n, \qquad i \neq k$$

This procedure enables us to retain the original order of the matrix, and the imposed boundary conditions are printed as part of the solution.

After incorporating the essential boundary condition, the linear system is solved to obtain the nodal temperatures. With solved nodal temperatures on boundary surface 2, the total heat flux can then be calculated. The total heat flux is obtained by summing the heat flux of each element which lies on the boundary surface 2.

Since there is a radiation term in the boundary condition, the problem is nonlinear. Thus an iteration process must be used to calculate the effect of the radiation term. The iteration procedure consists of the following:

1. set the iteration number as I=1 and assume $h_r^{(e)}=0$
2. solve the Equation (4.26) and find T on every node
3. find the new value of $h_r^{(e)}$ for each element using the definition Equation 4.3
4. if I>1, test for the convergence of the method using the following criteria

$$\left| \frac{(h_r^{(e)})_I - (h_r^{(e)})_{I-1}}{(h_r^{(e)})_{I-1}} \right| < \delta_1 \tag{4.27 a}$$

and

$$\left| T_I - T_{I-1} \right| < \delta_2 \tag{4.27 b}$$

where $\delta 1$ and $\delta 2$ are specified small numbers. If these criteria are satisfied then the method is assumed to have converged. Hence stop the method by taking

$$T(x,y) = T_I(x,y)$$

On the other hand, if either of the inequalities of Equation 4.27 are not satisfied, set the new iteration number as I=I+1, go to step 2. If I is greater than 30, the program will stop the iteration and output the results.

Figure 4.3 shows the flow chart of the finite element program, FEM2D, which is developed in this dissertation.

4.3 Mesh Generation

A program was required to fit a two-dimensional element mesh to the deposit and tube geometry. The MESHGEN program was developed to create the mesh. The mesh is generated by two steps:

1) generate a mesh for the metal tube and steam-side scale.

2) generate a mesh for the ash deposits.

First the mesh is generated for a rectangle, then it is converted to a mesh for the cylinder and steam-side scale. Second, search the nodes which make up the ash deposits and metal tube interface, then extended the lines from each node, until they meet the ash deposit surface, then the mesh on the domain created by these lines and ash surface is generated as for a rectangle. The typical mesh generated by MESHGEN is shown in Figure 4.4.

The boundary surface is very important. Elements and nodes which are on the boundary surface must be identified by MESHGEN for future use in main program (FEM2D). Szczygiel et al. [1991] presented a simple algorithm for identification of the discrete curves bounding 2-D regions. It consists of two stages:

1. searching for the boundary elements
2. sorting the boundary elements to form closed contours

The first stage is based on the simple fact that all the edges of the finite elements appearing in only one element must belong to the boundary of the entire domain. An equivalent and equally obvious statement is that the edges common to two elements must lay within the domain. The edges of the finite elements are defined by the connectivity array. The computations are arranged in three nested loops, The external one is over all elements defined by the connectivity array. The medium loop is over all edges of the current finite element. Within the internal loop the selected edge is sought for in all elements not yet considered. If such an edge is not found, then the current one is a boundary element. All boundary elements are stored in the boundary array.

The second stage is a rearrangement of the matrix obtained in the first stage. The algorithm employs the obvious fact that each boundary element has one common node with the preceding and succeeding boundary elements. The calculations are performed within one loop extending over the boundary elements selected in the first step and stored in the connectivity array. For a given boundary element, another one having the same node is sought. If such a boundary element is found, it is assigned as the next element in the contour and marked as a processed element. The search in the next steps of the loop is performed over elements not yet processed. If no element having a common node with a given element if found, then the latter should have a common node with the first boundary element in the contour. Otherwise, an error in the preparation of the connectivity array has been committed which produces an appropriate message and causes the program to stop.

4.4 Test of the Convergence of FEM2D Code

Numerical schemes have convergence problems. It has been proved that the error $e^h = u - u^h$ in the finite element method satisfies

$$N(e^h, e^h) < C h_l^2 \qquad (4.28)$$

Where u denotes to true solution and u^h denotes the approximation. $N(e^h, e^h)$ represents the inner products of e^h. C is a constant independent of u and u^h and h_l is the characteristic length of an element. For the whole domain, h_l is defined as maximum of h_l for all elements.

The final result is thus a bound of order h_l^2 for the error. Computation shows this bound to be completely realistic, and in practice the error $N(e^h, e^h)$ is almost exactly proportional to h_l^2, beginning even at very crude meshes. Error estimates of the type in Equation 4.28 are very useful because this gives an idea of the accuracy of the approximate solution, whether we know the true solution or not. While the estimate gives an idea of how rapidly the finite element solution converges to the true solution, it does not tell us when to stop refining the mesh.

The convergence of the FEM2D code has been tested for a cylinder with inside temperature T_1 = 866 K, and gas temperature T_2 = 1388 K. The outside radius R_2 = 2.54 cm and inside radius R_1 = 2.032 cm. The thermal conductivity of the tube is K = 25 $W \cdot m^{-1} \cdot K^{-1}$. There is only convection between gas stream and tube surface and the convection heat transfer coefficient (h) is 80 $W \cdot m^{-2} \cdot K^{-1}$. The heat transfer rate may be expressed as

$$q''_r = \frac{R_1 (T_1 - T_2)}{\frac{1}{h} + \frac{R_1 \ln(R_2/R_1)}{k}} \qquad (4.29)$$

Under these conditions, the analytical solution of the heat transfer rate is 41384.7006 $W \cdot m^{-2}$ (13123.0886 $Btu \cdot h^{-1} \cdot ft^{-2}$). The Figure 4.5 shows the error vs. characteristic length of the element. It shows that error is proportional to h_l^2, and proves that the FEM2D code is convergent.

4.5 Thermal Properties

It has been documented in many references that thermal conductivity and emissivity vary under different boiler operating conditions, and this changes the total heat flux rate from the tube. Wall et al. (1979) stressed the importance of making measurements of both the emissivity and thermal conductivity in operating boilers because in-situ values could be significantly different than those found using customary laboratory techniques.

For the powdery deposit regime, Boow and Goard (1969) have determined the emissivity of glass powders, and laboratory-prepared and boiler ashes, of different sizes at 775 K. From the results they obtained an expression:

$$\varepsilon = 0.3 \log(d) + 0.16 \qquad (4.30)$$

where ε is the emissivity and is d is the particle diameter in μm. They also have shown that the thermal conductivity of unsintered ash depends on the particle size, and from the experimental results they deduced an equation:

$$\log(K) = (0.56 \log(d)) - 1.63 \qquad (4.31)$$

for iron-containing ash, where K is the thermal conductivity in $W{\cdot}m^{-1}{\cdot}K^{-1}$ and d is the particle diameter in μm.

For sinter/slag ash, Mulcahy et al. (1966) have measured the emissivity of coal ash and boiler at different temperatures, and a typical emissivity/temperature relationship was given. Wall et al. (1993) gave a review for ash thermal conductivity at sinter/slag condition. The thermal conductivity of the metal tube at different temperatures and different scales is obtained from Steam [1992].

Depending on the viscosity of the deposit layer, FEM2D program can handle powdery and sticky deposit layers.

The convection heat transfer coefficient between the gas stream and tube is calculated by using the empirical correlation due to Hilpert

$$\frac{\bar{h} D}{K} = C_1 \, Re_D^{C_2} \, Pr^{1/3} \qquad (4.32)$$

Where Re_D is the Reynolds number, and C_1 and C_2 are constant. All properties are evaluated at the film temperature. Equation 4.32, and the constants C_1 and C_2 are from Incropera and DeWitt [1990]. The convection heat transfer coefficient is treated as an overall constant in the current study. However it should be treated as a variable along the circumference of tube in the future study.

CHAPTER V

RESULTS AND DISCUSSION

5.1 Introduction

In this chapter, the numerical results of the mass and heat transfer analysis for ash deposits on superheater tubes are first compared with available experimental data. Subsequently, the effects of other operating conditions on the ash deposition and the total heat flux will be discussed. Absoft MacFortran II [1992] language was used for all computer programs. The computer programs were compiled under MPW Shell [1989]. A Macintosh Quadra 900 computer with a 68040 CPU and 28.7 MB of RAM was chosen for these calculations.

5.2 Mass Transfer Comparison

The superheater test module (SHTM) at the UTSI CFFF (Figure 5.1) experiences the flue gas environment and tube temperatures expected in MHD superheaters, permitting evaluation of fouling, corrosion, and heat transfer in such devices. In order to characterize thickness development and width growth of the deposit base in contact with the initially clean tube surface during test LMF5-J, a rotatable, 2.5" diameter tube called the ash deposition probe (ADP) was installed behind Test Section One (TS1) in the SHTM. Video images of the probe were recorded by a video camera looking in a glass port beside the ADP. The ADP and port locations are shown in Figure 5.2.

Two six-hour test runs were completed successfully with the air-cooled ash deposition probe (ADP). The tube-metal temperature was controlled manually at approximately 1100 °F. All automatic sootblowers ahead of the ADP probe were turned off in order to keep the ash deposit on the ADP undisturbed. Preceding each test period, the local ADP sootblower was activated to provide a clean probe surface at time zero. Video images were obtained showing the development of the ash deposit thickness. At one-hour intervals the ADP was rotated 90° for a very brief period to photograph the width of the deposit, then returned to its normal orientation. The width and the thickness of the deposit are defined in Figure 4.1.

Tables 5.1 and 5.2 contain the results from computerized image analysis of digitized VCR images. A Macintosh IIfx computer with a 68030 CPU was used for these measurements. The Macintosh computer was equipped with a Quickcapture frame grabber made by National Instruments. Video recordings were made with a Panasonic WD-6000 camera and input to the frame grabber was provided via a Magnavox VR 9610AT01 VCR operating with an SP speed setting. Image analysis software was NIMH Image, Version 1.41.

Simultaneous experiments were conducted during the first six-hour test period that involved MHD-system operation at variable K_2/S ratios that were lower than the normal operation value of K_2/S of 4.2. This influenced the rate of buildup of the ash deposit, and somewhat less deposition occurred during the first run than the second. The second run had normal K_2/S ratios of 4.2, and there was little variation in this parameter throughout the second run. These effects are shown in Figures 5.3 and 5.4. Error bars indicate a precision of $\pm\sigma$. In addition to illustrating an increased rate of deposition, Figure 5.4 has an excellent correlation coefficient ($\approx$0.99) for the theoretically-expected linear relationship.

The width of the deposits were essentially constant after four to six hours. However, measurements of width were difficult to obtain early in the test periods. A comparison of Table 5.1 and 5.2 shows that the second run had a slightly greater width.

In order to numerically model the ADP conditions, the following information was necessary and thus obtained. Hot gas velocity at the ADP location was measured twice during the test by using a Pitot tube, both measurements giving 31 feet per second. Ash samples collected from the baghouse were used to determine particle size distribution via an Environmental Protection Agency-Southern Research Institute five-stage series cyclone that is designed to produce an equally spaced particle size cut (D50) on a logarithmic scale within the range of 0.1-10 µm. The particle size distribution from the five stage cyclone for the LMF5-G test and its curve fit is

Table 5.1 ADP Measurement Data for LMF5J Test Based on Montana Rosebud Coal with Variable K_2/S Ratio for Run 1

Hours since ADP soot-blowing	0.0	1.0	2.0	3.0	4.0	5.0	6.0	Pre-cision, ±σ
Clock time & date	03:00 9/24/93	04:00 9/24/93	05:00 9/24/93	06:00 9/24/93	07:00 9/24/93	08:00 9/24/93	09:00 9/24/93	
Average front-edge deposit thick-ness, mm	NA	2.3 (0.09")	3.0 (0.12")	2.5 (0.10")	3.3 (0.13")	3.6 (0.14")	5.6 (0.22")	±0.25 (±0.01")
Average front-edge deposit linear width, mm	NA	NA	NA	NA	57.2 (2.25")	56.4 (2.22")	NA	±1.27 (±0.05")

shown in Figure 5.5. Montana Rosebud Coal was used for the LMF5 test series. An AMRAY® scanning electron microscope (SEM) was used for photographing samples collected from stage 1 of the five stage cyclone and also the ADP tube. The largest particle in stage 1 measured 9 μm in diameter, but some particles with an 11 μm diameter were measured in the sample of ash from the ADP tube. Therefore, 11.5 μm diameter was assumed to be the maximum particle diameter for the curve fitting purposes. There is approximately 10% seed in the condensed phase when hot gas temperature is 2300 °F and the K_2/S ratio is around 4.2, according to Foote et al. [1993], so the total dust loading corresponding to particle sizes from 5 μm to 11.5 μm is

Table 5.2 ADP Measurement Data for LMF5J Test Based on Montana Rosebud Coal with 4.2 K_2/S ratio for Run 2

Hours since ADP soot-blowing	0.0	1.0	2.0	3.0	4.0	5.0	6.0	Pre-cision, ±σ
Clock time & date	09:12 9/24/93	10:12 9/24/93	11:12 9/24/93	12:12 9/24/93	13:12 9/24/93	14:12 9/24/93	15:12 9/24/93	
Average front-edge deposit thick-ness, mm	NA	1.8 (0.07")	2.0 (0.08")	3.6 (0.14")	4.3 (0.17")	6.1 (0.24")	7.4 (0.29")	±0.25 (±0.01")
Average front-edge deposit linear width, mm	NA	NA	NA	NA	59.4 (2.34")	61.2 (2.41")	61.2 (2.41")	±2.03 (±0.08")

3.48 $g{\cdot}m^{-3}$. Using the Fereday equation, equation 3.6, the ash particle viscosity is much less than 10^8 Poise. Particles with viscosity this low are classified as sticky, which means that the staying probability is one for all particles at any location. After the test, the ash deposit on the ADP was examined, and the deposit was completely molten. The porosity of the ash deposit on the ADP tube is assumed to be zero. The true particle density is obtained from the ash sample collected on front side of the ADP tube under these conditions, at 2.372 $g{\cdot}cc^{-1}$. Tables 5.3 and 5.4 show the particle size distribution used in the calculation for comparison to MHD test results.

Under the conditions described earlier, the numerical results for the ash

Table 5.3 Particle Size Distribution of Rosebud Coal Only

Bins	1	2	3	4	5
Particle Size, μm	6.	14.	24.	35.	45.
Weight Percentage,%	16.	18.	20.	22.	24.

Table 5.4 Particle Size Distribution of Rosebud Coal Plus Seed

Bins	1	2	3	4	5
Particle Size, μm	5.5	7.5	8.8	10.2	11.5
Weight Percentage,%	16.	20.	21.	21.	22.

deposition shape from Run 2 are shown in Figure 5.6. Figure 5.7 and 5.8 show the comparison of the numerical and measured results for the ash deposition thickness and width. The numerically calculated thicknesses are greater than the experimental measurements. There are three reasons that could account for this: 1) The maximum particle diameter is overestimated by using 11.5 μm diameter as maximum particle diameter in the curve fitting, even if 11 μm diameter particles were observed from the ADP ash sample. 2) The staying probability is overestimated by just assuming 100% staying probability, even if sticky particles impact on the sticky surface. 3) The impacting particle may "sandblast" the deposition layer, which is a mechanism of the surface layer erosion due to inertial impaction not considered in this study. The numerically calculated widths are less than the experimental measurements; this can be attributed to the difficulties of measurement, as well as the movement of the partially liquid ash deposits toward the sides.

Figure 5.9 shows the local collection efficiency *(β)* vs. distance from stagnation point *(s)*. An increase in particle diameter relative to the tube diameter causes an increase of the local collection efficiency, since an increase in the free-stream momentum of the ash particle makes it easier for the large particles to hit the cylinder. Figure 5.10 shows the chemical composition (SiO_2 and K_2O) distribution vs distance from stagnation point *(s)*. Since the local collection efficiency at each location, and the elemental analysis of fly ash for each particle size are different, the deposit layer's viscosity and thermal properties can vary around the circumference of the tube.

Figure 5.11 shows the numerical results for the thermophoretic layer. It shows that as the temperature gradient increases between the surface and gas, the thermophoretic layer growth rate, or the mass transfer rate due to "thermal drive force", increases. However, no experimental data exists with which to compare these calculated results.

In conclusion, the measurement technique for measuring the mass transfer rate due to inertial impaction was a good choice and, in general, the results of the measurement and numerical analysis are in good agreement.

5.3 Heat Transfer Comparison

Smouse and Wagoner [1991] conducted an experiment in the PETC Fuels Evaluation Facility (FEF) to investigate specific details of deposit formation mechanisms without the presence of "sticky" surfaces and particles.

Smouse et al. [1988] presented the design details of the FEF. The combustor was fired with natural gas at or exceeding its nominal coal rating of 0.5 million Btu/hr during all tests to yield a flue gas velocity of 61 $ft \cdot sec^{-1}$ at the simulated superheater tube (i.e., fouling probe) at temperatures in the range of 1975-2100 °F. The air-cooled fouling probe, which was constructed from a 1" diameter 316 stainless steel tube, was maintained at 1100 °F. A blend of the fine and sieved coarse aluminum oxide powders was prepared in a ratio of 18/1 that resembled the particle size distribution of fly ash from pulverized coal combustion. Figure 2.5 shows the fine and coarse aluminum oxide powders particle size distribution. The blend's ash particle size distribution is shown in Figure 5.12. Table 5.5 shows the particle size distribution used in the calculation. This powdery particle density was 3.97 $g \cdot cc^{-1}$ and had a melting point of 3700 °F. Two tests were conducted by injecting this powder into the FEF at different rates, as shown in Table 5.6. The lower injection rate and the higher injection rate were equivalent to the ash input when firing a bituminous coal with an ash content of approximately 10% and 22% at full loading, respectively.

Figure 5.13 shows the numerical results for the ash deposition shape in the first hour for the lower injection rate case. The dust loading data are from the injection rate and an isokinetic sampling, respectively. A porosity of 0.65 was assumed according to Wessel and Wagoner [1986]. As noted earlier in this work, it was assumed that all non-sticky particles that contacted the deposit surface were captured in the deposit layer if the deposit layer was

Table 5.5 Particle Size Distribution of Al_2O_3 Powder

Bins	1	2	3	4	5
Particle Size, μm	5.	6.	7.	9.1	12.5
Weight Percentage, %	24.	27.	18.	22.	9.

Table 5.6 Dust Loading of 18/1 Blend for Two Tests at PETC FEF

Injection Rate	Isokinetic Sampling at Downstream
4.1 lb/hr	2.5 lb/hr
8.7 lb/hr	4.5 lb/hr

greater than the particle penetration distance. The FEF observations were as follows: during a 4.25-hour total test period, with lower dust loading, the deposit approached 51 mm (2") in height several times during the test before partial shedding. The deposit did not exhibit any sign of melting, sintering or fusion. For comparison, Figure 5.13 shows 9 mm/hr growth at the stagnation point by using the dust loading from the isokinetic sampling rate, and 23 mm/hr growth by using the dust loading from the injection rate. Therefore, the conclusion follows that using the injection rate dust loading is a better choice for the calculation of mass transfer due to inertial impaction, resulting in reasonable agreement with FEF observations.

The total heat flux was calculated for the FEF lower dust loading case under different conditions. As mentioned earlier, a submicron deposit layer with emissivity ranging from 0.1 to 0.2 reduces heat transfer to the tube dramatically. Figure 5.14 shows the effect of the thermophoretic layer's emissivity on heat transfer. The calculation proved that the thermophoretic layer building up causes dramatic decreases in total heat flux. For the calculations shown in Figure 5.14 no scale was assumed on the inside of the tube. However, such scale, which usually has low thermal conductivity, is another main source which affects the predicted and actual heat flux. Since the probe in the PETC FEF test was air-cooled, there was no solid scale inside the tube. However, there still could be a very thin layer inside the tube caused by deposit of charring of oil vapor present in the compressed air cooling medium (the compressed cooling air was not filtered and it contains some oil vapor from the compressor). Figure 5.15 shows the effect of 20 μm thin layer with thermal conductivity 0.06 $W \cdot m^{-1} \cdot K^{-1}$ on total heat flux; it shows that consideration of even very fine or thin scale layers in heat transfer calculations is necessary for accuracy. Based on results shown in Figure 5.14 and 5.15, a 20 μm thin layer and 0.2 emissivity for the thermophoretic layer were assumed for additional calculations. Figure 5.16 shows the predicted total heat flux based on two dust loadings: the dust loading data are from the injection rate and the isokinetic sampling. Figure 5.16 also proves that using the injection rate dust loading is better than using the isokinetic sampling dust loading, for predicting deposition and heat transfer. Very good agreement between the numerical and measured data was obtained on this basis.

During the UTSI LMF5-G MHD tests, the average heat fluxes for the CS3 tube banks were measured. At this location, the average gas velocity was 20 $ft \cdot sec^{-1}$, the average gas temperature was 1500 °F, and all CS3 tubes had a 2.5" outside diameter; all seed was in the condensed phase according to Foote et al. [1993]. The porosity of ash deposits is 0.3. Under these conditions, and using particle size distribution from Figure 5.12 for coal plus seed, the ash deposition shape is predicted as shown in Figure 5.17. The average heat flux of CS3 tube banks from measurement is compared with the total heat flux from the numerical prediction for the single CS3 tube as shown in Figure 5.18. Three reasons why the numerical results are greater than the measured data are: 1) Some tubes in the tube bank are close to the refractory wall and may have lower heat flux rates due to lower gas velocity, whereas the numerical results are for a single tube in a large uniform stream, so that greater than average heat flux rate are expected; 2) since CS3 is a water cooled tube, the scale build up inside the tube might be greater than 20 µm, thus leading to lower experimental heat fluxes since assumed 20 µm scale was used in the calculations. 3) since the average heat flux data chosen was from a period of time between two sootblowing occurrences during the test, the thickness of the thermophoretic layer was not known. However, a clean tube was assumed for the calculation of the thermophoretic layer at time zero, hence, an underestimation of the thermophoretic layer will result in an overestimated total heat flux. Unfortunately, there is no accurate data for the thickness of the steam-side scale and thermophoretic layer at this time.

5.4 Some Factors That may Affect Mass and Heat Transfer

In this section, the effect of changing some of the operating conditions will be discussed. For any specific condition not discussed, the condition is the same as that used for the calculation of deposition and heat flux for a single tube at the CS3 location, as discussed in Chapter 5.3.

The velocity of the flue gas is a very important consideration when inertial impaction is involved. Figure 5.19 shows the ash deposit with gas velocity 20 $ft \cdot sec^{-1}$ and 60 $ft \cdot sec^{-1}$ and constant tube diameter (2.5") for an MHD visual site-specific computer simulation. The range in velocity might have been created by operational changes (boiler load) or design considerations, for example. It shows that the deposit shape is extremely sensitive to changes of gas velocity. However, even though ash deposits are larger due to higher velocity, the total heat flux increases with the gas velocity.

An illustration of the importance of the diameter of the superheater tube is shown in Figures 5.21 and 5.22. With inertial impaction of fly ash occurring on the leading edge of the superheater tube, the shape, thickness, and mass of the deposit changes significantly as the tube diameter changes. The total heat flux increases as the tube diameter decreases, due to the increases of the convection heat transfer coefficient.

So far, Figures 5.19-5.22 illustrate the combined effect of the tube diameter and the flue gas velocity. These observations are especially significant when one considers that deposition probes with outside diameters in the range of 1" to 2" are often used by many investigators for "relative" deposition measurements and fuel evaluation in pilot-scale testing. If the small diameter tubes are placed in a test section with reduced cross-sectional area in an effort to produce desired flue-gas velocity, the risk is high that the walls of the constricting section ahead of the tube location will remove fly-ash particles selectively because of high target efficiency for specific particle diameters, thus changing particle size distribution and dust loading at the superheater tube site. Since the relative effects may be different for different ash particle-density/particle-size distributions, relative test results may not always be reliable. The total heat flux comparisons prove that the effects of radiation and forced convection on the total heat flux are more important than the effect of the thermal conductio of the ash deposition.

Additional details of the effects of fly-ash particle density are shown in Figure 5.23 and 5.24, with the former displaying visual computer simulations. The higher density particles (5.18 $g \cdot cc^{-1}$), which would be produced from the oxidation of pyrite, contact a wider portion of the circumference of the tube and have a higher probability of contacting the tube surface. However the thickness build-up is less at the stagnation point with the higher density particles because the deposit density also is higher (equal to the particle density, because of the same porosity assumption for the calculation). The net effect is a deposit with a more blunt shape for the Fe_3O_4 particles. The total heat flux predicted for the two cases is very close. However, it cannot be conclude that the particle density effect on the heat transfer can be neglected in practice. In the present calculation, the same particle size distribution and porosity were used in both calculations, this would not be true in general practice. Generally speaking, the particle size distribution and porosity will change as the particle density varies.

Compared to the ASTM coal ash data in Table 5.9, the ash elemental analysis values are quite different for the cyclone-sized data (by stage, S-1, S-2, etc.) in Tables 5.7 and 5.8 from the isokinetic sampling of MHD flue gas taken downstream from the superheater near the ESP inlet during LMF5-F periods firing coal alone or coal plus seed. Also significant differences in composition occur by ash particle size. The effect of using MHD potassium-containing seed plus coal vs. firing only Montana Rosebud coal during a six-hour period is shown in Figure 5.25. The fly ash produced while firing coal alone exhibits a much more massive deposit on the 2.5" OD tube in the computer simulation. Also the deposit contacts far more of the tube circumference around the leading edge, and it has more of a blunt shape. These results are produced by the changes in particle size distribution of the fly ash. In this case, massive ash deposits on the front side definitely reduce the total heat flux as shown in Figure 5.26.

Figure 5.27 shows the total collection efficiency for the five cases discussed earlier. The collection efficiency increases with increasing particle size and gas velocity, because an increase in the free-stream momentum of the droplet with respect to a cylinder increases the forces necessary to force the droplet around the cylinder. An increase in the cylinder size decreases the collection efficiency, since the large cylinders cause the flue-gas streamlines to start moving around the cylinder at an actual greater distance (not in terms of ratio to cylinder radius) ahead of the large cylinder than of the small cylinder.

Table 5.7 Elemental Analysis of Coal Only for MHD Test

	Stage 1 9.87 μm	Stage 2 6.30 μm	Stage 3 4.63 μm	Stage 4 2.68 μm	Stage 5 1.60 μm
SiO_2	19.93 %	21.60 %	22.39%	23.50%	24.24%
Al_2O_3	11.78 %	12.15 %	12.82%	13.55%	14.07%
Fe_2O_3	2.99 %	2.50 %	2.97%	3.04%	3.29%
TiO_2	0.74 %	1.65 %	1.96%	1.41%	1.28%
CaO	12.34%	12.91%	14.38%	15.03%	17.44%
MgO	2.25 %	2.56 %	2.89%	3.26%	3.97%
Na_2O	0.91 %	1.73 %	6.08%	4.96%	1.99%
K_2O	29.97%	30.12%	24.91%	21.74%	18.56%
SO_3	16.09%	14.28%	13.57%	10.57%	10.93%
CO_2	N/A	N/A	N/A	N/A	N/A

Table 5.8 Elemental Analysis of Coal Plus Seed for MHD Test

	Stage 1 9.87 μm	Stage 2 6.30 μm	Stage 3 4.63 μm	Stage 4 2.68 μm	Stage 5 1.60 μm
SiO_2	7.45%	0.24%	4.94%	3.80%	3.85%
Al_2O_3	4.01%	2.99%	1.60%	0.67%	0.38%
Fe_2O_3	1.12%	0.85%	0.58%	0.36%	0.30%
TiO_2	0.30%	0.24%	0.17%	0.09%	0.11%
CaO	5.54%	4.59%	2.87%	1.79%	1.67%
MgO	1.09%	0.97%	0.43%	0.41%	0.37%
Na_2O	0.92%	6.02%	0.76%	4.64%	0.79%
K_2O	49.75%	47.40%	50.27%	51.12%	53.37%
SO_3	11.07%	12.12%	12.75%	13.46%	12.86%
CO_2	13.57%	15.15%	14.45%	N/A	16.14%

Table 5.9 ASTM Elemental Ash Analyses for Coal Ash

SiO_2	37.26 %
Al_2O_3	15.37 %
Fe_2O_3	4.11 %
TiO_2	0.74 %
CaO	21.92%
MgO	3.25 %
Na_2O	0.39 %
K_2O	1.01 %
SO_3	11.20%
CO_2	N/A

CHAPTER VI

CONCLUSIONS AND RECOMMENDATIONS

A site-specific, fundamental engineering approach has been developed for predicting the shape, thickness, and chemical composition of ash deposit layers on superheater tubes as a function of time. This method is based on coupled analytical models for particle deposition and subsequent ash layer formation on the tubes, as well as for heat transfer for the superheater tubes. Deposition is modeled by both inertial impaction as well as thermophoretic processes. Both sticky and non-sticky particles, as well as tube surface conditions, can be accounted for in the model for prediction of deposition and heat transfer rates.

Numerical results from the model have been compared to experimental data, the results have been generally good even though the entrained flyash sample input data were obtained for the MHD test from samples collected downstream from the superheater. The model shows that heat transfer predictions can be sensitive to scale deposit layers on the steam side of the superheater tubes, as well as oil vapor char film on the inside of air-cooled tubes. The present research also shows the effects of change of dust loading, gas velocity, gas temperature, steam temperature, tube diameter, chemical composition of ash size fraction, particle size distribution, and particle density on ash deposition and total heat flux for superheater tubes. As stressed by

Wagoner et al. [1991], it is necessary to accurately measure the "local conditions" just upstream of the superheater tubes in order to have sufficient knowledge to give the effects of these conditions on superheater tube performance.

This research has provided a comprehensive description of the physics of the deposition process for two-dimensional systems. In particular, the effects of sticky and non-sticky particles, and surface conditions on deposition have been summarized in tables, and an explanation of how deposits could be formed of non-sticky particles on non-sticky surface has been presented for the first time.

Although great progress has been made, a considerable amount of deposition research and development of the engineering model remains. In particular, for the model, the following enhancements are suggested: 1) variable thermal properties in the finite element method for the deposit layer, 2) effects of freestream turbulence on particle deposition rates and heat transfer, 3) more accurate surface convective heat transfer coefficient incorporated in the model. Experimentally, the following data bases need to be assembled: 1) flyash particle sizes and velocities measured just upstream of the superheater tubes, 2) better measurements of flyash viscosity and surface tension in sintering-temperature range, and better correlations between ash elemental composition, sintering strength, viscosity, and surface tension.

LIST OF REFERENCES

LIST OF REFERENCES

Absoft, "Absoft MacFortran II Reference Manual", Version 3.2, 2781 Bond Street, Rochester Hills, MI 48309, 1992.

Berkowitz, Brian M, and Riley James T., " Analytical Ice Shape Predictions for Flight in Natural Icing Conditions", NASA Contractor Report 182234, 1988.

Boow, J. , and Goard, P.R.C., "Fireside Deposits and Their Effect on Heat Transfer in a Pulverized Coal Fired Boiler, Part 3- The Influence of The Physical Characteristics of the Deposit on its Radiant Emittance and Effective Thermal Conductance", Jour. Inst. Fuel, 44,412., 1969.

Brun, R.J., Lewis, W., Perkins, P.J., and Serafini J.S., "Impingement of Cloud Droplets on a Cylinder and Procedure for Measuring Liquid-Water Content and Droplet Sizes in Supercooled Clouds by Rotating Multicylinder Method", NASA Report 1215, 1955.

Byers, R. Lee and S. Calvert, "Particle Deposition From Turbulent Streams By Means of Thermal Force", I&EC Fundamentals, Vol. 8, No. 4, pp 645-655, 1969.

Dahneke, Barton, "The Capture of Aerosol Particles by Surfaces", Journal of Colloid and Interface Science, Vol. 37, No. 2, October, 1971.

Epstein, H.A., Z. Phys. 54, 537, 1929.

Ellenbecker, M. J., Leith, D., and Price, J. M. "Impaction and Particle Bounce at High Stokes Numbers", Journal of the Air Pollution Control Association, November 1980, Volume 30, No. 11.

Epstein, P. S., "Contribution to the Theory of Radiation", Zeitschr. Physik., 54, p537 ,1929.

Foote, J., P., Winkleman, B., C., and Giel, T. V., "Particle Effects on Gas Optical Properties and Radiation Heat Transfer in an MHD Furnace", Proceedings 31st Symposium on Engineering Aspects of Magnetohydrodynamisc, June 29- July 1, 1993, Whitefish, Montana, page VII 5.1- 5.6.

Frenkel, J.J., "Viscous Flow of Crystalline Bodies under the Action of Surface Tension", Jour Phys. (Moscow), 9, page 385, 1945.

Frost, W., Chang, H., Shieh, C., and Kimble, K., "Two-Dimensional Particle Trajectory Computer Program", Interim Report for Contract NASA 3-22448., 1982.

Fred, J. Kohl, Gilbert, J. Santoro, Carl A. Stearns, and George, C. Fryburg, " Theoretical and Experimental Studies of the Deposition of Na_2SO_4 from Seeded Combustion Gases", Vol. 126, No 6, Journal Electrochem. Soc: SOLID-STATE SCIENCE AND TECHNOLOGY JUNE , 1979.

Gökoglu, S.A., "Thermophoretically Enhanced Deposition of Particulate Matter Across Nonisothermal Boundary Layers", Ph.D. Dissertation, Yale University, 1992.

Gökoglu, S.A., and Rosner, Daniel E., " Engineering Correlations of Variable-Property Effects on Laminar Forced Convection Mass Transfer for Dilute Vapor Species and Small Particles in Air", NASA Contractor Report 168322, 1984.

Gökoglu, S.A., and Rosner, Daniel E., "Correlation of Thermophoretically-Modified Small Particle Deposition Rates in Forced Convection Systems with Variable Properties, Transpiration Cooling and/or Viscous Dissipation", Int. J. Heat Mass Transfer, Vol. 27, No. 5, pp. 639-645, 1984.

Gordon, Sanford, and McBride, Bonnie J., "Computer Program for Calculation of Complex Chemical Equilibrium Compositions, Rocket Performance, Incident and Reflected Shocks, and Chapman-Jouget Detonations", NASA Lewis Research Center, NASA SP-273, 1971.

Hess, J.L. and Smith, A.M.O., "Calculation of Potential Flow About Arbitrary Bodies", Progress in Aeronautical Sciences, 8:1-138, (D. Kuchemann, editor). Elmsford, New York, Pergmon Press, 1967.

Israel, R. and Rosner, D.E., "Use of a Generalized Stokes Number to Determine the Aerodynamic Capture Efficiency of Non-Stokes Particles from a Compressible Gas Flow", Aerosol Science and Technology 2:45-51, 1983.

"Macintosh Programmer's Workshop Development Environment, Volume 1", Version 3.1, Apple Computer, Inc., 20525 Mariani Avenue, Cupertino, California 95014, 1989.

Mulcahy, M.F.R., Boow, J. and Goard, P.R.C., "Fireside Deposits and Their Effect on Heat Transfer in Pulverized Fuel Fired Boiler, Part 1-The Radiant Emittance and Effective Thermal Conductance of the Deposits, Part 2-The Effect of the Deposit on Heat Transfer from the Combustion Chamber Considered as a Continuous Well-Stirred Reactor", Jour. Inst. Fuel, 39, Part 1, p.385, Part 2, P.394, 1966.

Incropera, Frank P. and DeWitt Devid P., FUNDAMENTALS OF HEAT AND MASS TRANSFER, JOHN WILEY & SONS, 1990.

Kalmanovitch, David P. and Frank, Melvin, "An Effective Model of Viscosity for Ash Deposition Phenomena", Proc. Engineering Foundation Conference on Mineral Matter and Ash Deposition from Coal, Santa Barbara, edited by R.W. Bryers and K.S.Vorres, pp. 89-102, 1991.

Raask, Erich, Mineral Impurities In Coal Combustion, Behavior, Problems, and Remedial Measures, Hemisphere Publishing Corporation, New York ,1985.

Rao, A.K. and Whitby, K.T., "Nonideal Collection Characteristics of Single Stage and Cascade Impactors", American Industrial Hygiene Association Journal, pp. 174-179, (38) April, 1977.

Rao, A.K. and Whitby, K.T., "Non-ideal Collection Characteristics of Inertial Impactors-II. Cascade Impactors", J. Aerosol. Sci., Vol. 9., pp87 to 100, 1978.

Rao, S. S., The Finite Element Method in Engineering, pergamon press, second edition, 1988.

Reddy, J. N., An Introduction to the Finite Element method, McGraw-Hill Publishing Company, 1984.

Rosner, D.E., Seshadri, K., J. Fernandez de la Mora, Fryburf, G.C., Kohl, F.J., Stearns, C.A., and Santoro, G.J., "Transport, Thermodynamic and Kinetic Aspects of Salt/Ash Deposition Rates from Combustion Gases", National Bureau of Standards Special Publication 561, Proceedings of the 10th Materials Research Symposium on Characterization of High Temperature Vapors and Gases held at NBS, Gaithersburg, Maryland, September 18-22, 1978

Rosner, D.E., Chen B.K., Fryberg, G.C, Kohl, F.J., "Chemically Frozen Multicomponent Boundary Layer Theory of Salt and/or Ash Deposition Rates from Combustion Gases", Combustion Sciences and Technology, 1979, Vol. 20, pp. 87-106.

Rosner, D. E., "Thermal (Soret) Diffusion Effects on Interfacial Mass Transport Rates", PCH PhysicoChemical Hydrodynamic, vol. 1, no. 2-3, 1980, pp. 159-185.

Rosner, Daniel E., Gökoglu, S.A. and Israel, Rajasingh, "Rational Engineering Correlations of Diffusional and Inertial Particle Deposition Behavior in Non-Isothermal Forced Convection Environments", Fouling of Heat Exchange Surfaces, Engineering Foundation Inc., 1983, pp 235-256.

Rosner, D.E., and Kim, S., "Optical Experiments on Thermophretically Augmented Submicron Particle Deposition from "Dusty" High Temperature Gas Flows," The Chemical Engineering Journal, 29 (1984), pp. 147-157.

Rosner, D.E., Transport Processes in Chemically Reacting Flow Systems, Butterworths, 1986.

Schuh, M. J., Schuler, C.A., and Humphrey, J.A.C., "Numerical Calculation of Particle-Laden Gas Flows Past Tubes", AIChE Journal, March 1989, Vol. 35, No. 3, p. 466-480.

Smouse, S.M. and Walber, G.F., "Design of a Pilot-Scale Fuels Evaluation Facility," in Proceedings of the Engineering Foundation Conference on Mineral Matter and Ash in Coal, Bryers, R. and K. Vorres (Ed.), Hemisphere Publishing, New York, 1988.

Smouse, S. and Wagoner, C. L., "Deposit Initiation: Part 2 - Experimental Verification of Hypothesis Using a Simulated Superheater Tube", Proceedings of the Engineering Foundation Conference on Inorganic Transformations and Ash Deposition During Combustion, March 10-15, 1991, in Palm Coast, Florida.

Srinivasachar S., Helbel, J.J., Katz, C.B. and Boni, A.A., "Transformations and Stickness of Minerals During Pulverized Coal Combustion", Proceedings on the Engineering Foundation Conferences on Mineral Matter and Ash Deposition from Coal, February 22-26, 1988, Santa Barbara, California.

Srivastava, R. and Rosner, D.E., "A new Approach to the Correlation of Boundary Layer Mass Transfer Rates with Thermal Diffusion and/or Variable Properties", Int. J. Heat and Mass Transfer, vol. 22, Sept. 1979, pp. 1281-1294.

STEAM its generation and use, edited by S.C. Stultz and J.B. Kitto, Babcock & Wilcox a McDermott company, 1992

Strang, Gilbert and Fix, George J., "An analysis of the Finite Element Method", PRENTICE-HALL, INC., Englewood Cliffs, N.J., 1973.

Svehla, Roger A., " Estimated Viscosities and Thermal Conductivities of Gases at High Temperatures", NASA technical report R-132, 1962.

Szczygiel, Ireneusz, Szlek, Andrzej, Bialecki, Ryszard and Nowak, Andrzej J., "Identification of the boundary curves in 2D finite elements codes", Advances in Engineering Software, Volume 13 No 2, March 1991

Tsai, C.J., Pui, David Y. H., and Liu, Benjamin Y. H., " Capture and Rebound of Small Particles Upon Impact with Solid Surfaces", Aerosol Science and Technology 12:497-507, 1990.

Wagoner, C. L. and Wessel, R. A., "Ash Deposits-Initiating the Change From Empiricism to Generic Engineering Part 2: Initial Results", Presented at the Jt. ASME/IEEE Power Generation Conference, Portland, Oregon, 1986.

Wagoner, C. L., "Deposition of Flame-Transformed Particles: A Second Look At Staying After Contact," Proceedings of the Sixth Annual International Pittsburgh Coal Conference, Pittsburgh, Pa., 1989.

Wagoner, C. L., Dowdy, T. E. and Attig, R. C., "Progress Toward a Universal Approach For Predicting and Measuring Effects of Fire-side Deposits", Proceedings on the Engineering Foundation Conferences on Mineral Matter and Ash Deposition from Coal, February 22-26, 1988, Santa Barbara, California.

Wagoner, C. L., Foote, J.P., and Attig, R.C., "Advanced Coal-Combustion System for Retroftting Oil/Gas - Designed Industrial Boilers", Proceedings of the Fifteenth International Conference on Coal & Slurry Technologies, Clearwater, Florida, pp 507-517, 1990.

Wagoner, C. L., Yan, X., "Deposit Initiation Via Thermophoresis: Part 1 - Insight On Deceleration and Retention of Inertially-Transported Particles", Proceedings of the Engineering Foundation Conference on Inorganic Transformations and Ash Deposition During Combustion, March 10-15, 1991, in Palm Coast, Florida.

Wagoner, C. L., and Yan, X., "How Ash Impaction Changes Shape of a Superheater Deposit with Time" Presented at Engineering Foundation Conference on the Impact of Ash Deposition on Coal Fired Plants, June 20-25, 1993, Solihull, Birmingham, UK.

Waldmann, L., "On the Motion of Spherical Particles in Nonhomogeneous Gases." Rarefied Gas Dynamics, edited by Talbot, L., Academic Press, New York, 1961, pp. 323-344.

Wall, T. F., T. Mai-Viet, H. B. Becker, and R. P. Gupta, "Fireside Deposits and Their Effect on Heat Transfer in P. F. Boiler: The Emissivity and Thermal Conductivity of Deposits and Their Components," Victoria State Electricity Commission Report GO/79/11, Melbourne, Australia , 1979.

Wall, T.F, Bhattacharya, S.P. Zhang, D.K., Gupta, R.P., and He, X. "The Properties and Thermal Effects of Ash Deposits in Coal-Fired Furnaces: a REVIEW." Presented at Engineering Foundation Conference on the Impact of Ash Deposition on Coal Fired Plants, June 20-25, 1993, Solihull, Birmingham, UK.

Walsh, P. M., A.N. Sayre, D.O. Loehden, L.S. Monroe, J.M. Beer and A.F. Sarofim, "Deposition of Bituminous Coal Ash on an Isolated Heat Exchange Tube: Effects of Coal Properties on Deposit Growth," Prog. Energy Combust. Sci., 16, 1990.

Watt, J.D. and Fereday, F., "The Flow Properties of Slags Formed from the Ashes of British Coals, Part I, Viscosity of Homogeneous Liquid Slags in Relation to Slag Composition", Jour. Inst. Fuel, 42, 99, 1969.

Weast, Robert C., "CRC Handbook of Chemistry and Physics", 68th Edition, 1987-1988, CRC Press, Inc., Boca Raton, Florida.

Wessel, R. A. and Wagoner, C. L., "Ash Deposits-Initiating the Change From Empiricism to Generic Engineering Part 1: The Generic Approach", Presented at the Jt. ASME/IEEE Power Generation Conference, Portland, Oregon, 1986.

Wessel, R.A. and Righi, J., "Generalized Corrections for Inertial Impaction of Particles on a Circular Cylinder." Aerosol Science and Technology 9:29-60, 1988.

Wright, William B., "Advancements in the LEWICE Ice Accretion Model", NASA Contractor Report 191019, 1993.

APPENDICES

APPENDIX A

PROCEDURE FOR MEASUREMENT OF PARTICLE DENSITY FROM MHD LMF5J TEST DATA

Equipment:

Pycnometer tube, calibrated and engraved for 50 ml at 20 °C, specific gravity

Nalgene© Multipurpose Jar and Vacuum Chamber

GAST diaphram vacuum pump, producing 23" mm Hg negative pressure

Balance

Oven, temperature controlled to 150 °C

Desiccator

Number two diesel fuel

Soapy water

Acetone

Procedure:

1. Dry the collected ash sample in the oven for one hour, then move it into desiccator.

2. Weight the clean pycnometer tube. Fully fill the tube with #2 diesel fuel, and then weight the tube and diesel fuel.

3. Empty the tube. Then wash in soapy water and rinse in acetone.

4. Weight the clean tube again. Take the ash sample out of desiccator and put it into the tube. Then weight the tube and ash. There should be as much as 25 cc ash sample in the vessel.

5. Add the diesel fuel into the tube, but do not fully fill the tube. Then put it into vacuum chamber and evacuate it for about 40 minutes or until there is no obvious air

bubbles coming out from the ash.

6. Take the tube out of the vacuum chamber, and fully fill the tube with diesel fuel. Slowly put a cap on the tube, wrap or seal the top of the tube, and clean up the outside of the tube. Then, weight the tube, ash and fuel together.

7. Clean up test site.

<u>Analytical Method for Particle Density:</u>

All of following data were obtained at a room temperature of 21.2 °C

Weight of tube, first time:	21.2276 g	(1)
Weight of the tube full of diesel fuel (tube+fuel)	(21.2276+43.0672) g	(2)
Density of diesel fuel (weigh of fuel / 50 ml)	0.86134 $g \cdot cc^{-1}$	(3)
Weight of the tube, second time	21.2290 g	(4)
Weight of the tube and ash (tube + ash)	(21.2290 + 4.994) g	(5)
Weight of the tube full of diesel and ash	67.4767 g	(6)
Weight of the tube	21.2290 g	(7)
Weight of the ash	4.9940 g	(8)
Weight of the fuel	41.2537 g	(9)
Volume of the tube full of fuel and ash	50 ml	(10)
Volume of the fuel (Weight / Density)	47.8948 ml	(11)
Volume of the ash (50 ml - Volume of the ash)	2.1052 ml	(12)

True particle density (equation 8 / equation 12) 2.372 $g \cdot cc^{-1}$

APPENDIX B

FIGURES

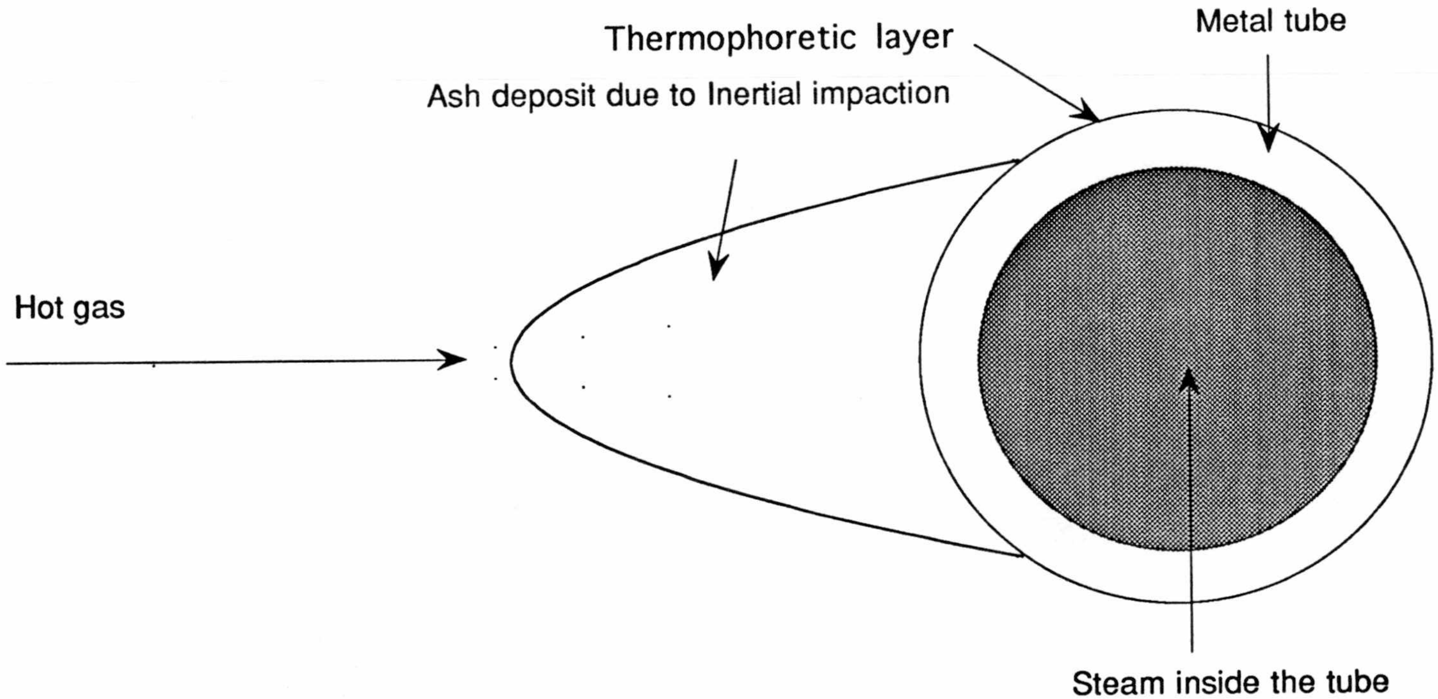

Figure 1.1 A Potential Cross Flow Over a Single Superheater Tube

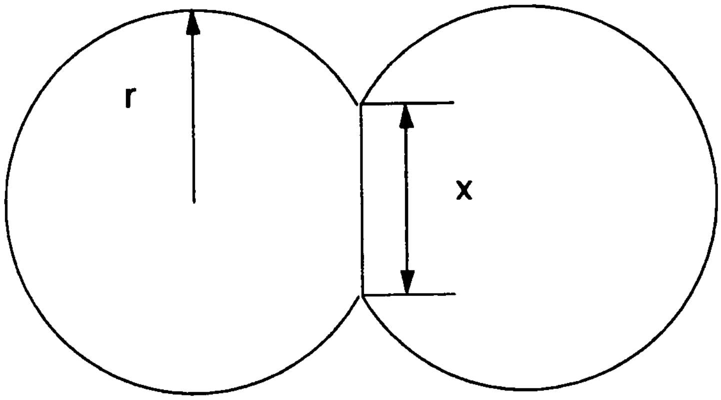

Figure 2.1 The Definition of Neck Bond Radius x and Particle Radius r

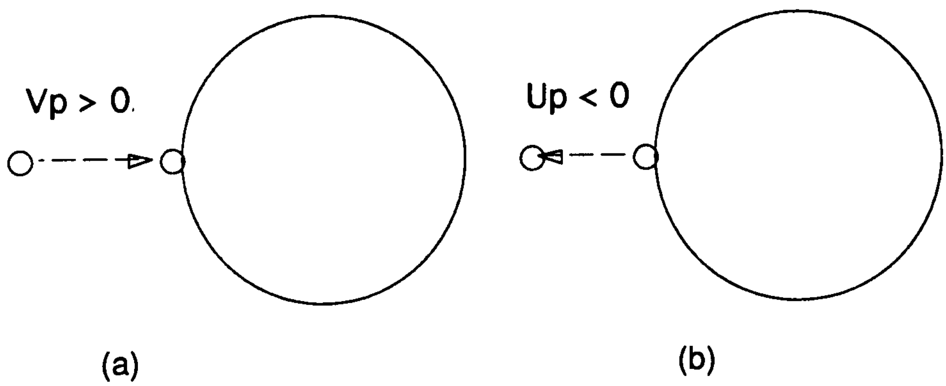

Figure 2.2 Normal Impaction of a Particle on a Tube. a) Particle Moves Forward to the Tube. b) Particle Rebounds from the Tube

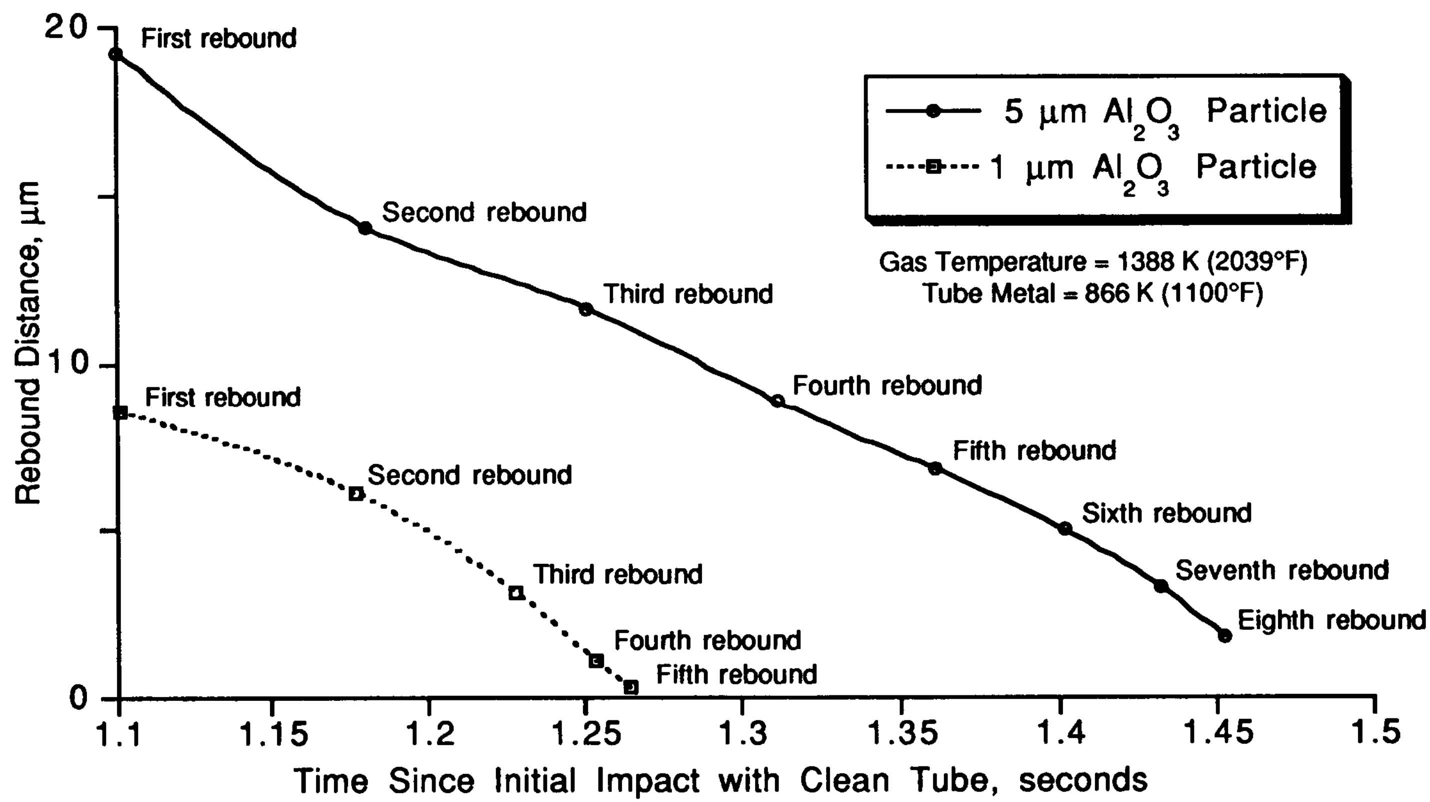

Figure 2.3 Thermophoretic Deceleration Between Elastic Collisions

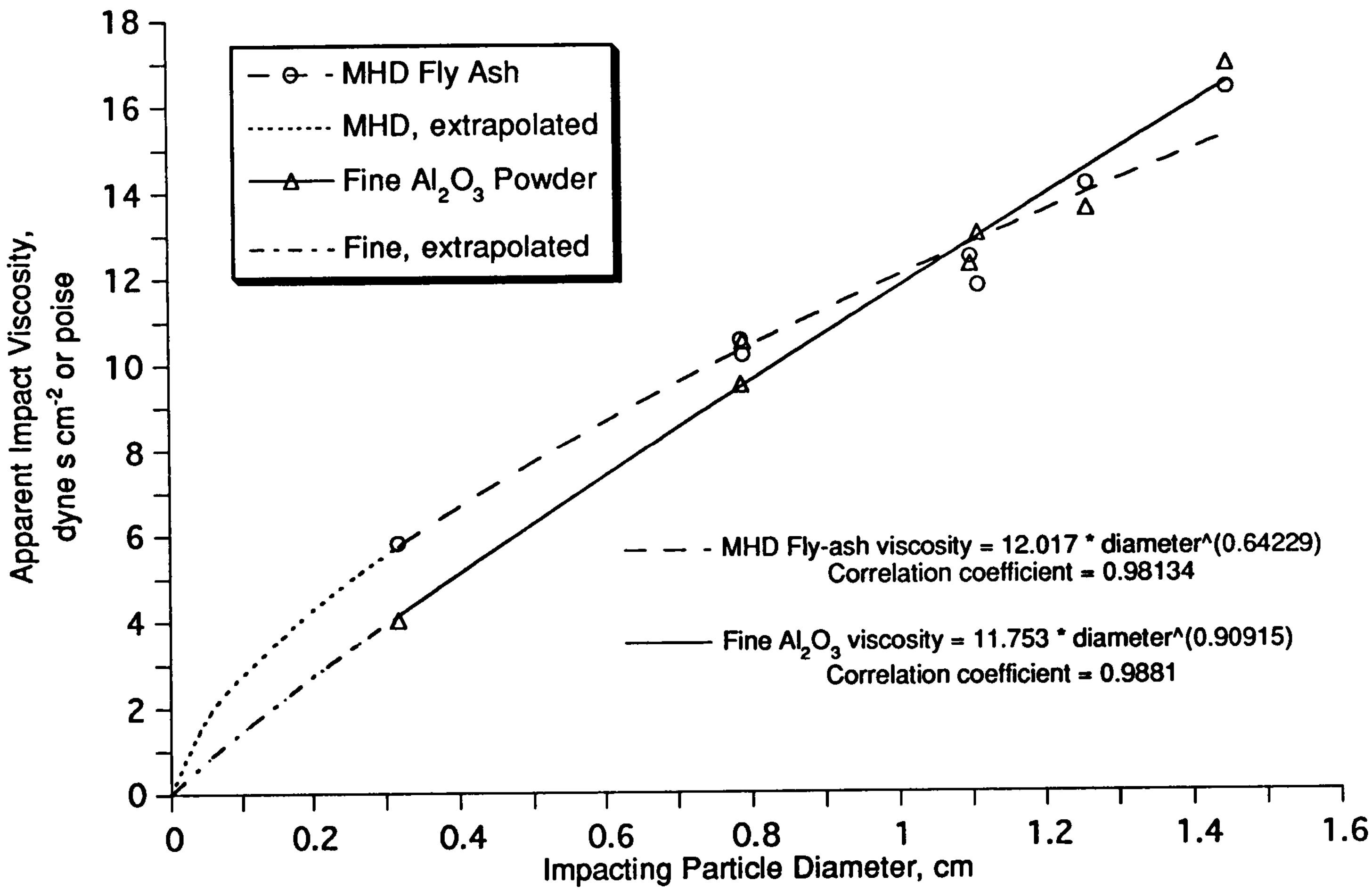

Figure 2.4 Comparison of Apparent Impact Viscosity of MHD Fly Ash and Fine Al_2O_3 Power Obtained by Ball Drop Experiments

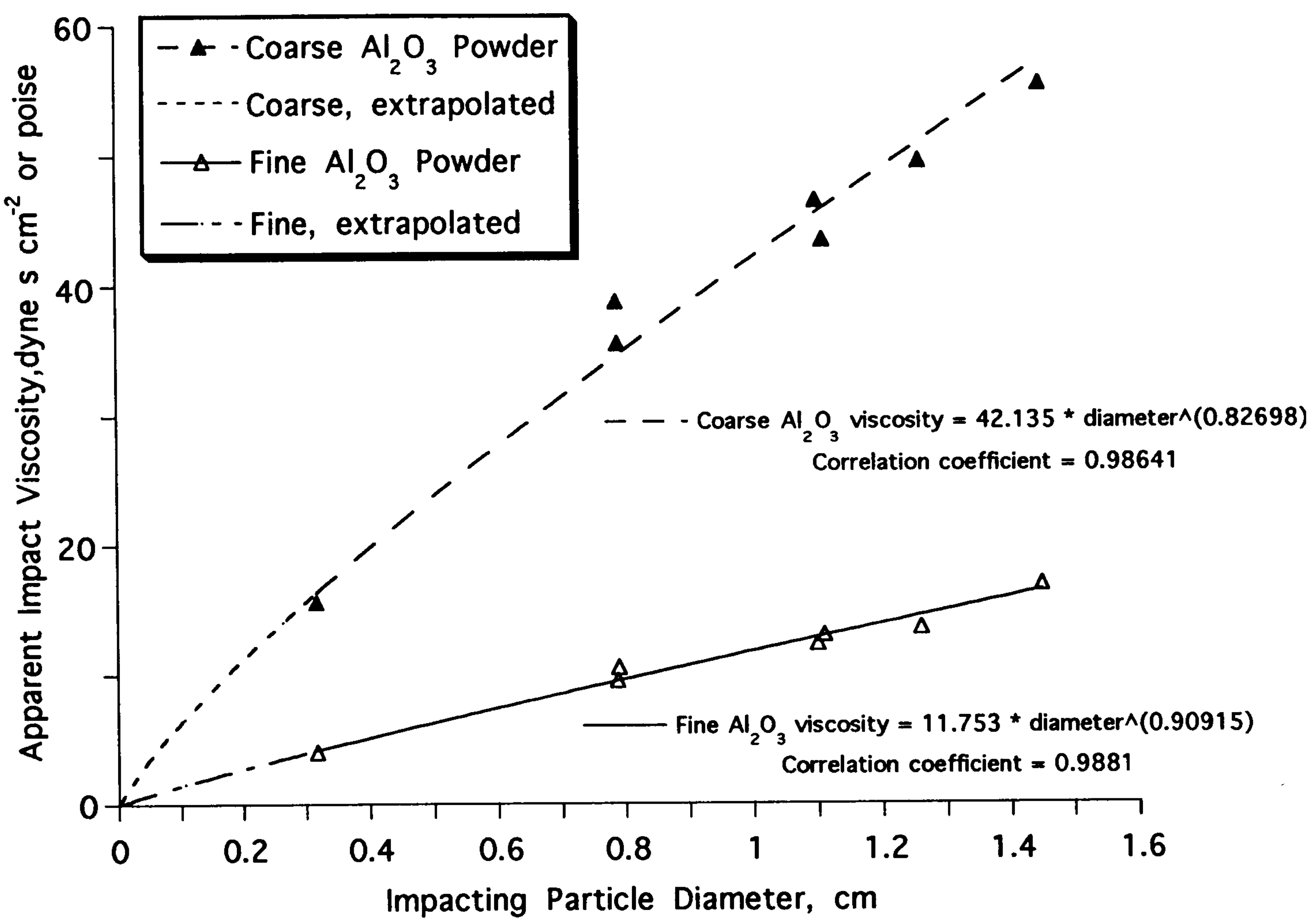

Figure 2.5 Comparison of the Apparent Viscosity of Coarse and Fine Al_2O_3 Powders Obtained by Ball Drop Experiments

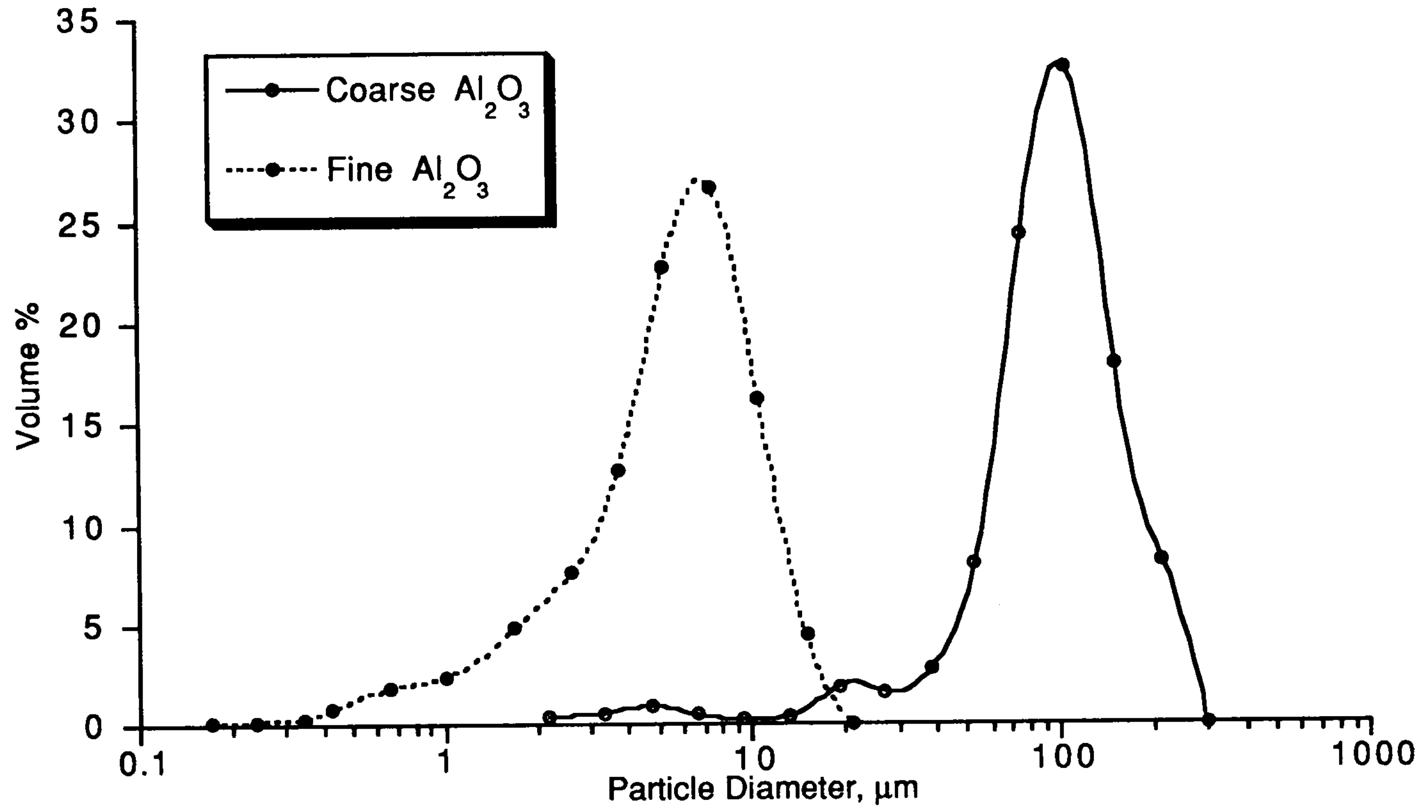

Figure 2.6 Aluminum Oxide Particle Size Distributions

Source: Smouse S. M. and Wagoner C. L., "Deposit Initiation: Part 2- Experimental Verification of Hypothesis Using a Simulated Superheater Tube." Proceedings of the Engineering Foundation Conference on Inorganic Transformations and Ash Deposition During Combustion, March 10-15, 1991

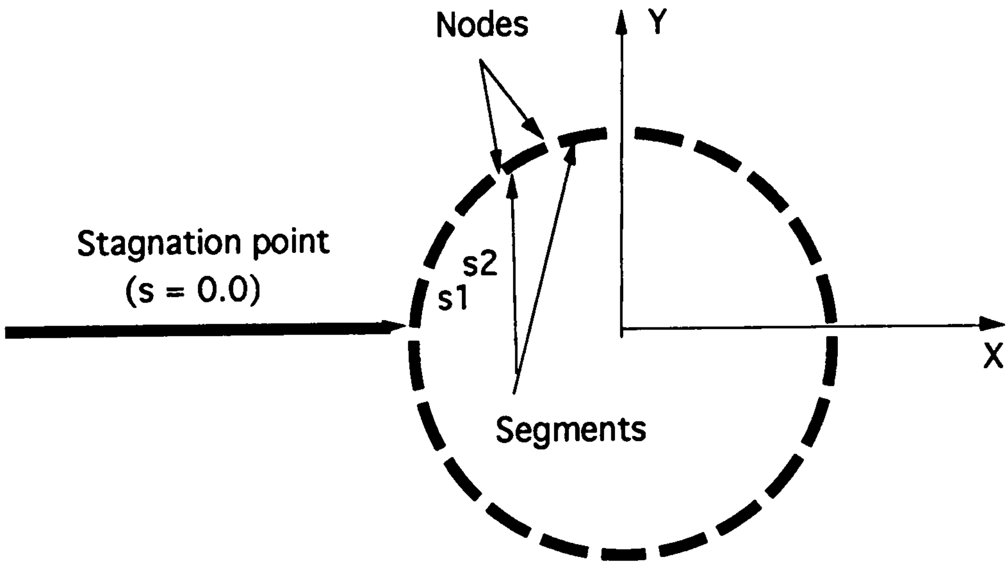

Figure 3.1 Geometry Defined by Segments Joining Body Coordinates

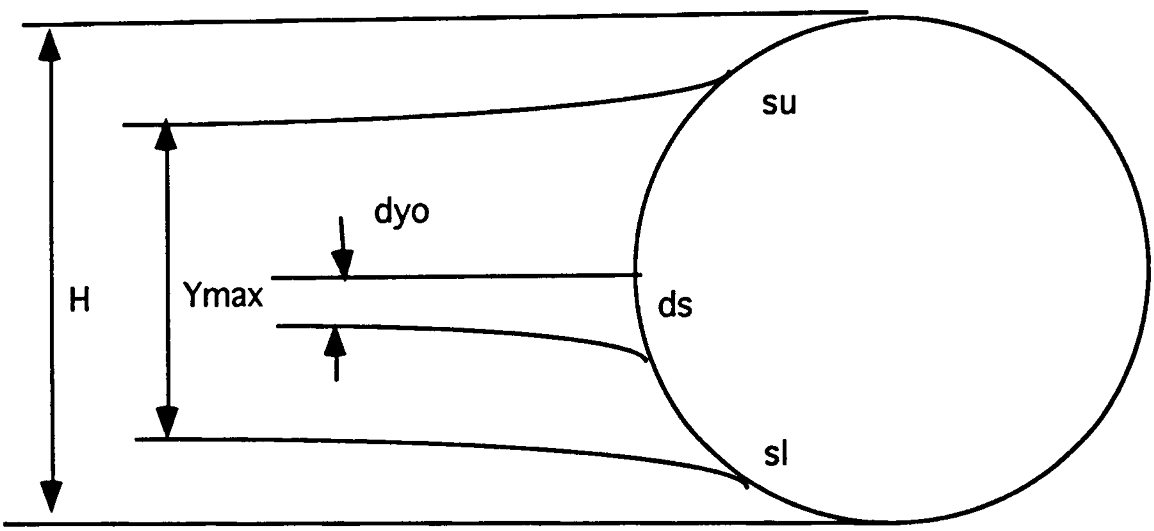

Figure 3.2 Geometric Quantities in Definition of Collection Efficiency

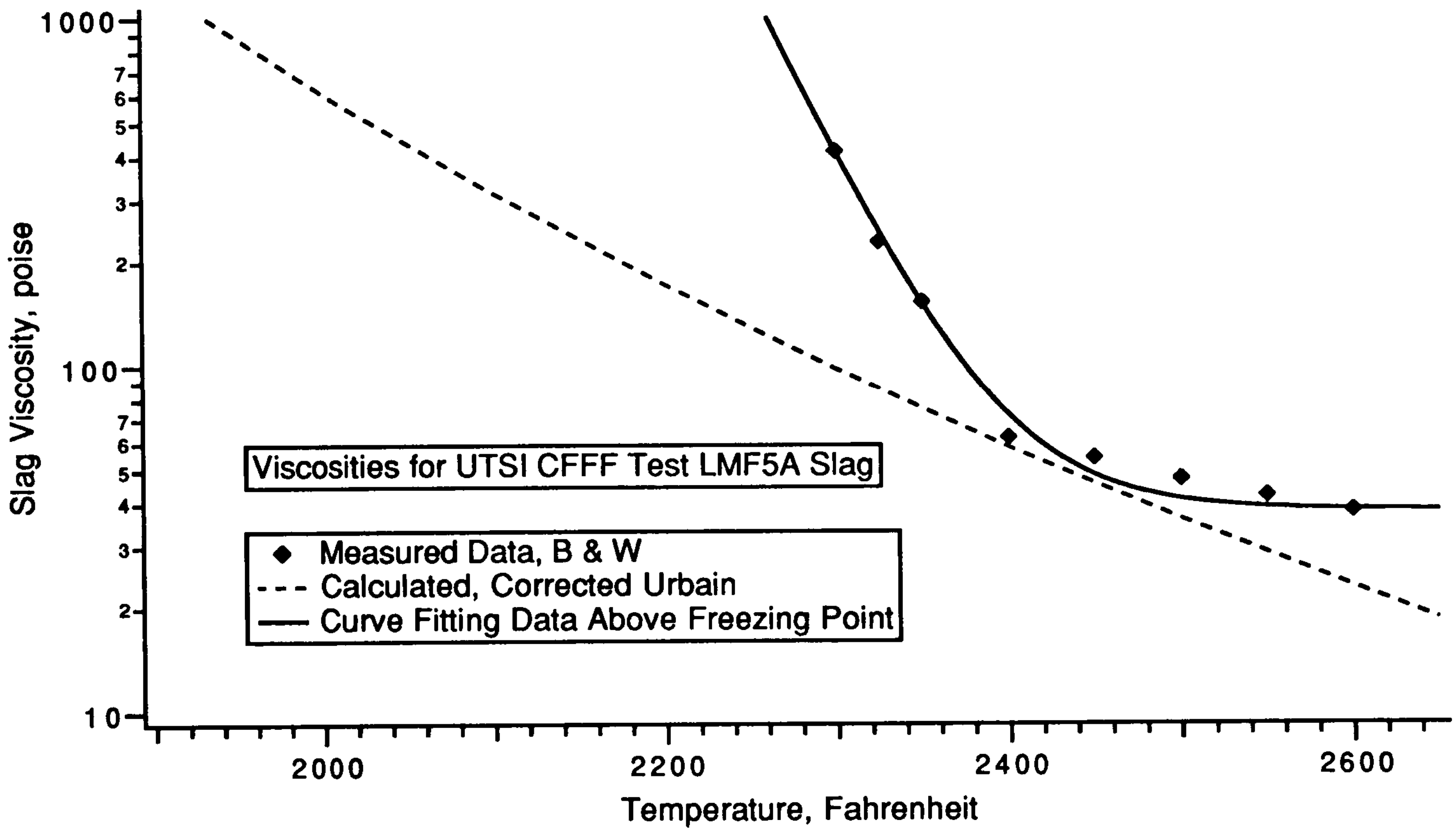

Figure 3.3 Comparison of Viscosity Data Obtained from Calculation and Measurement

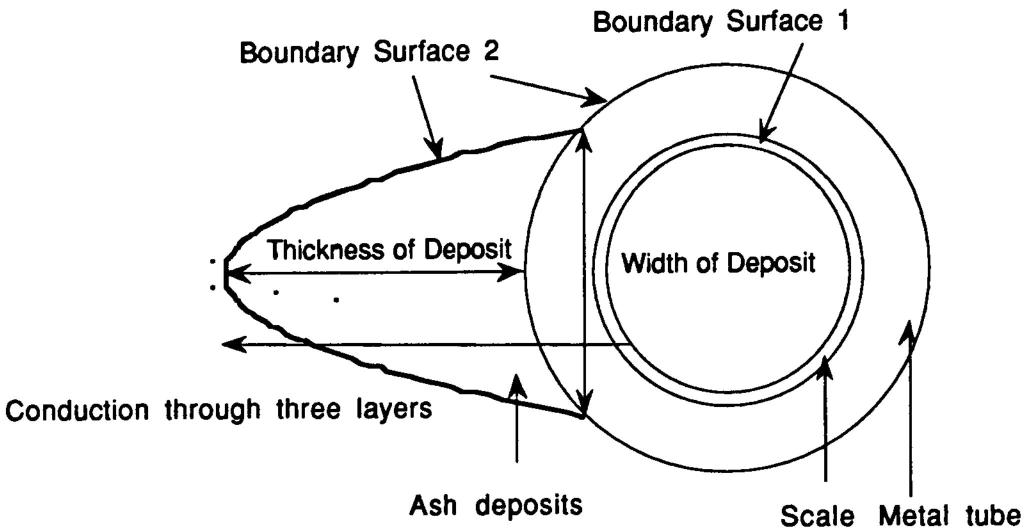

Figure 4.1 Heat Transfer Through Scale, Metal Tube and Ash Deposits

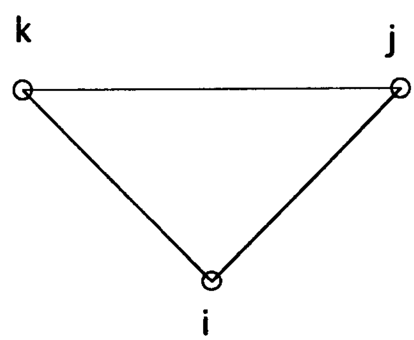

Figure 4.2 i, j and k Permute in a Counter-clockwise Direction

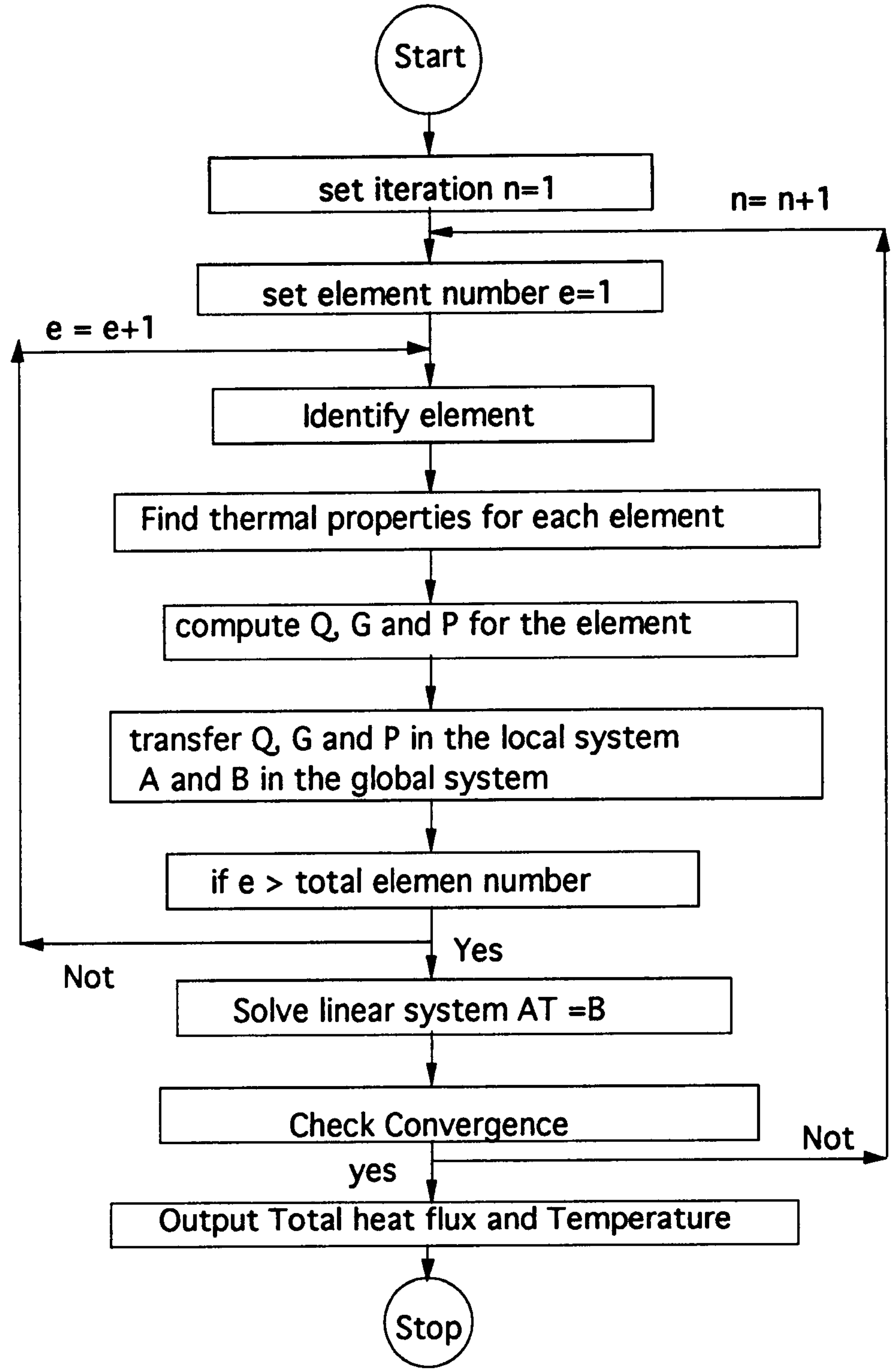

Figure 4.3 Flow Chart of FEM2D Program

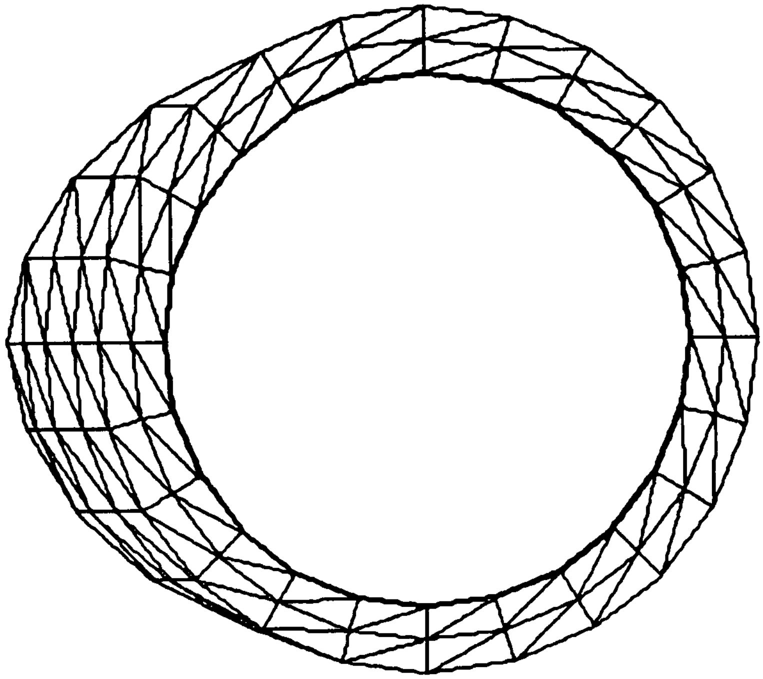

a. Crude Mesh Generated by MESHGEN Program.

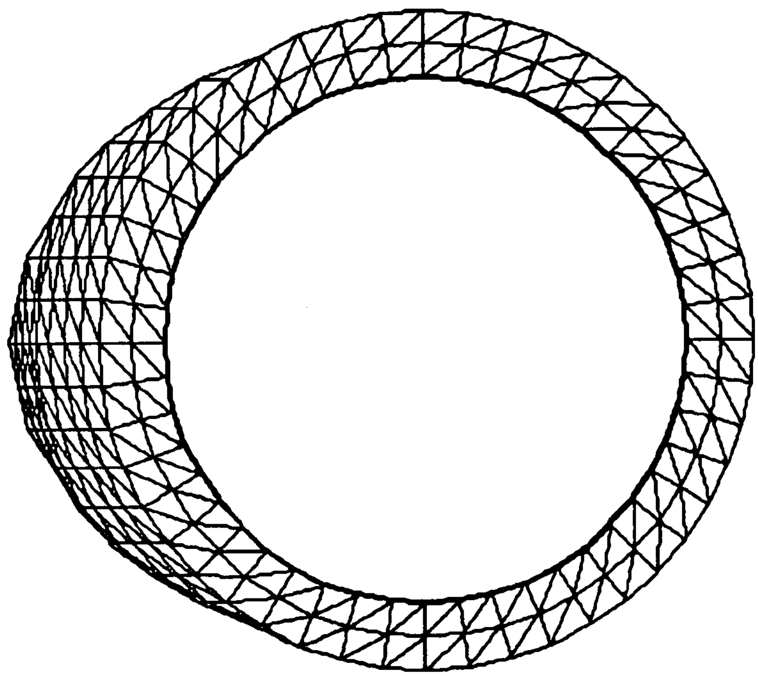

b. Fine Mesh Generated by MESHGEN Program
Figure 4.4 Mesh Generated by MESHGEN Promgram

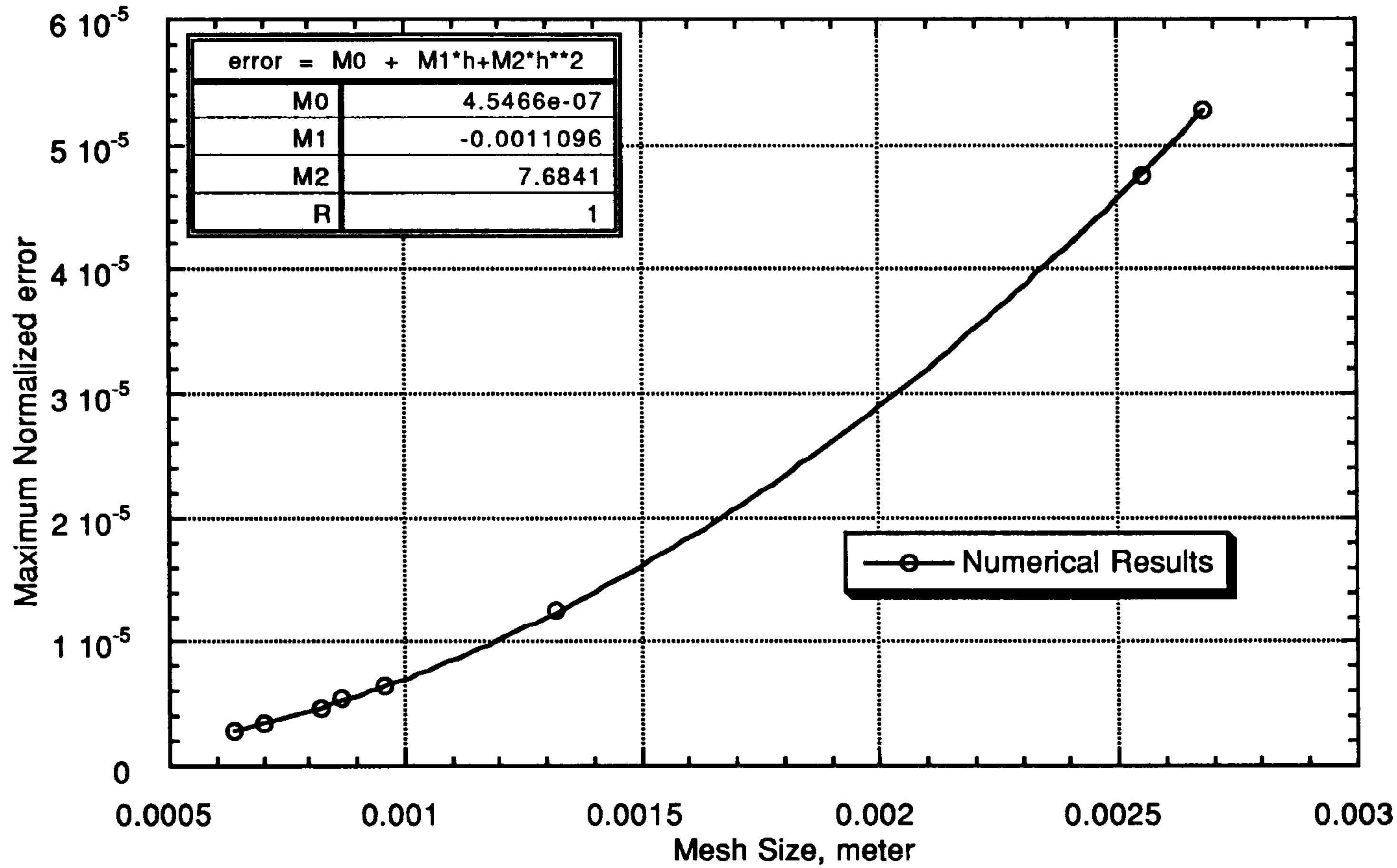

Figure 4.5 Convergence Test of FEM2D Program

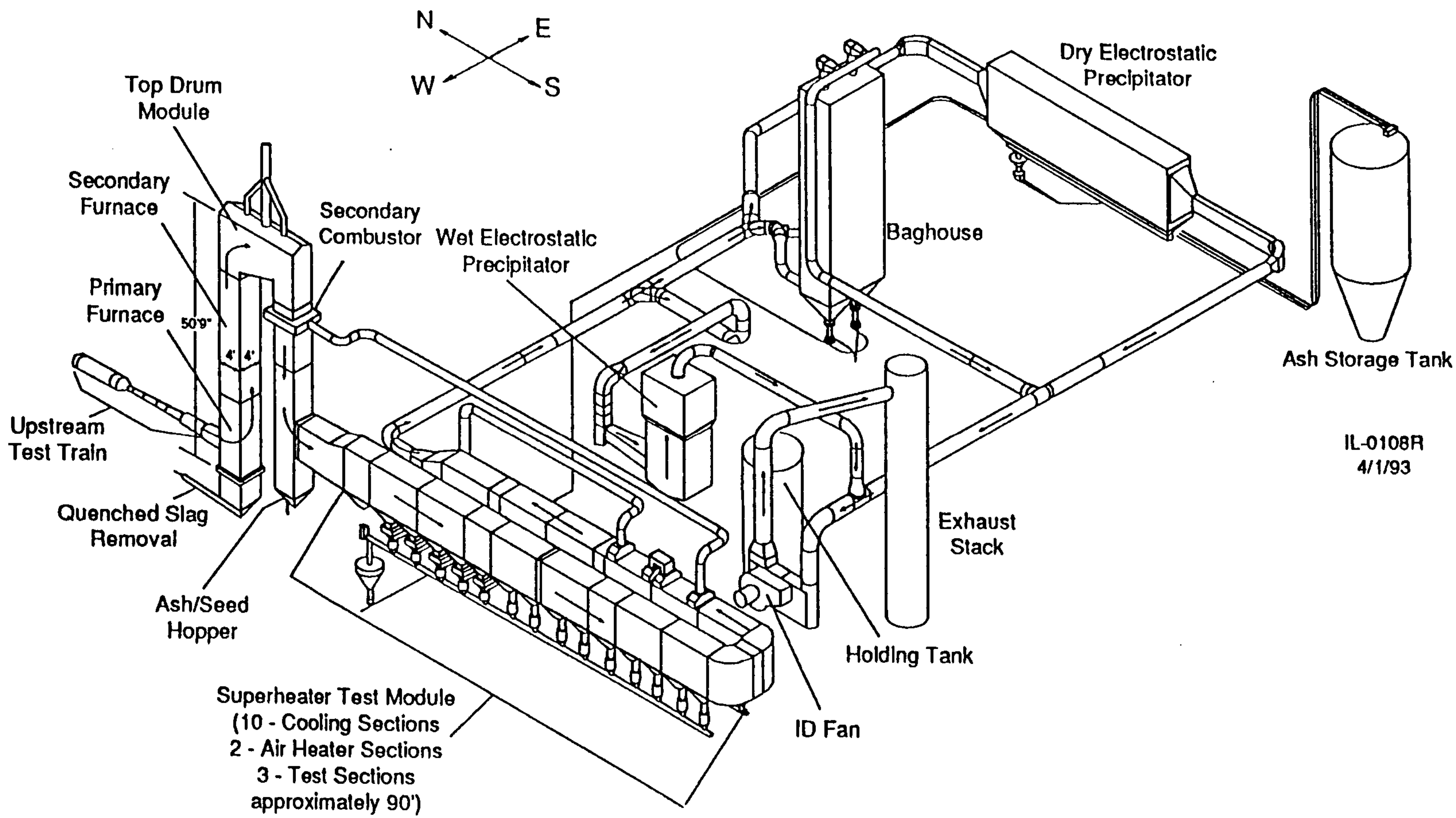

Figure 5.1 CFFF Integrated MHD Bottoming Cycle Schematic

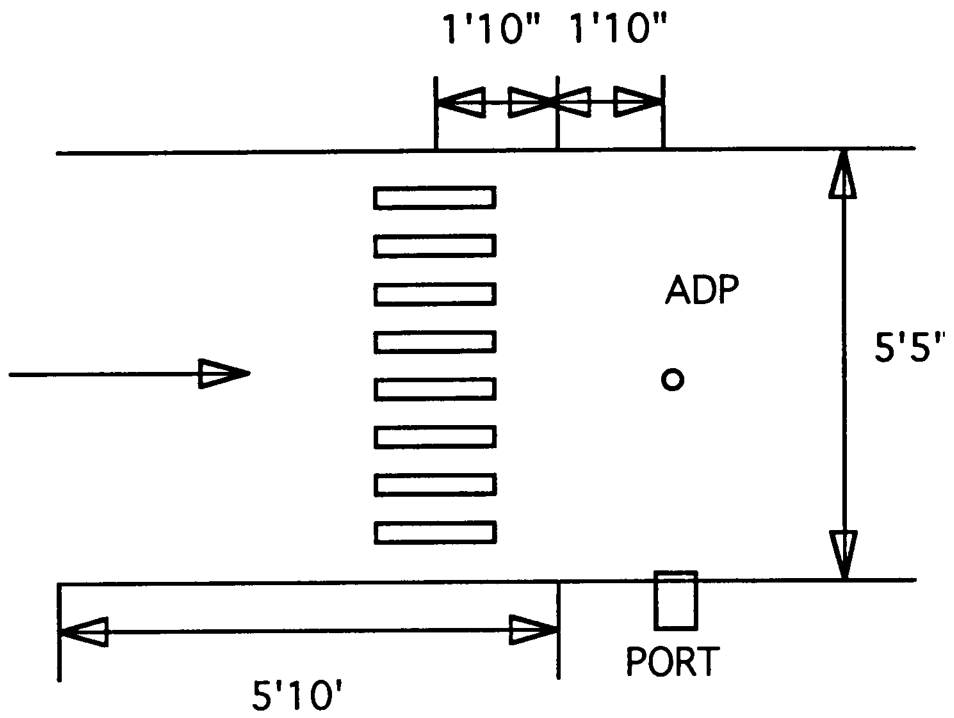

a. View from top to bottom

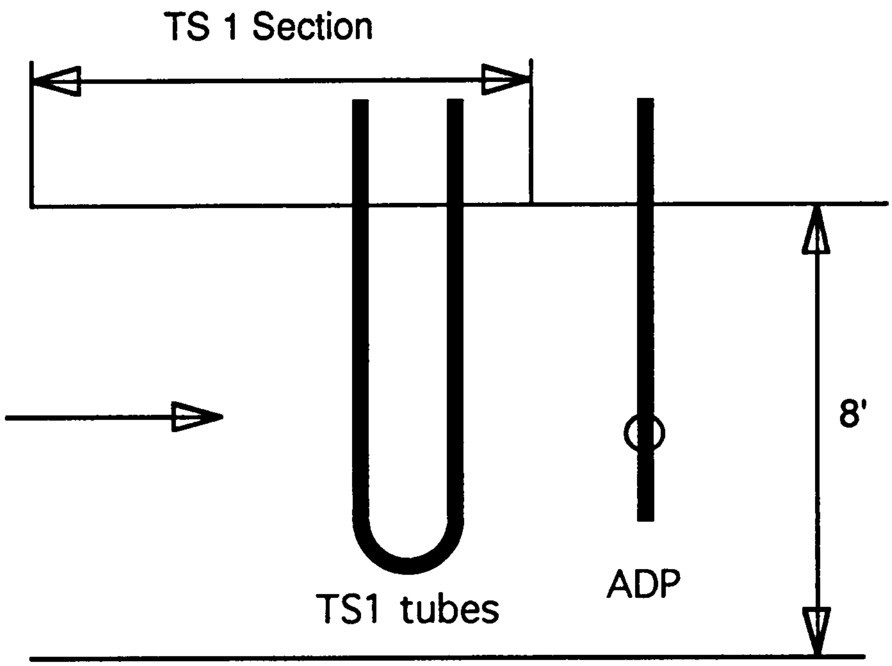

b. View from side

Figure 5.2 Location of ADP Tube and Port

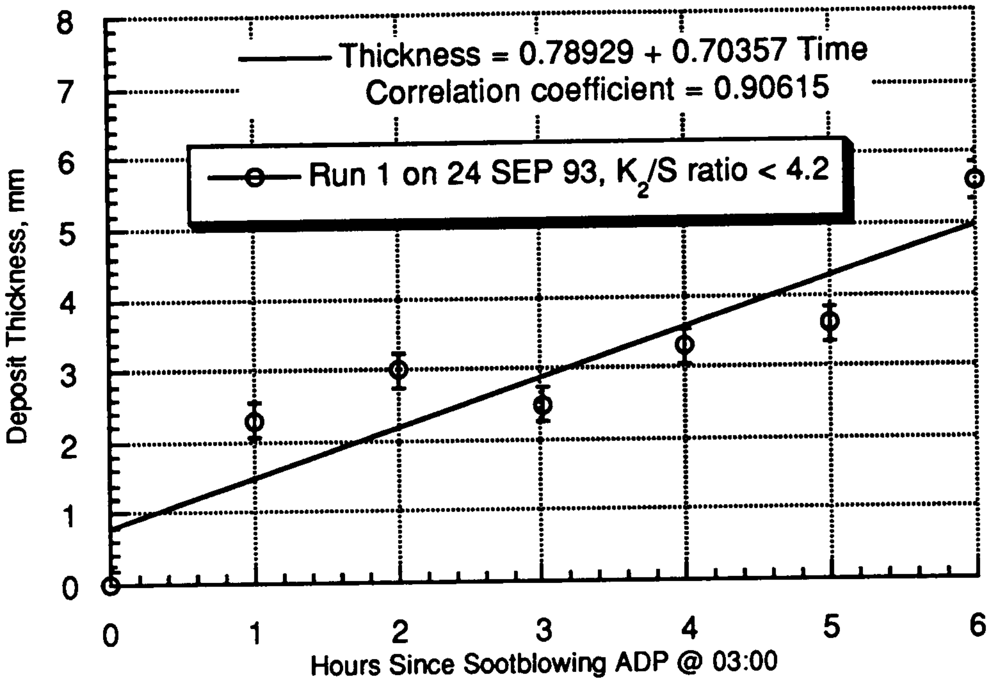

Figure 5.3 Measurement of ADP Ash Deposition Thickness for Run 1

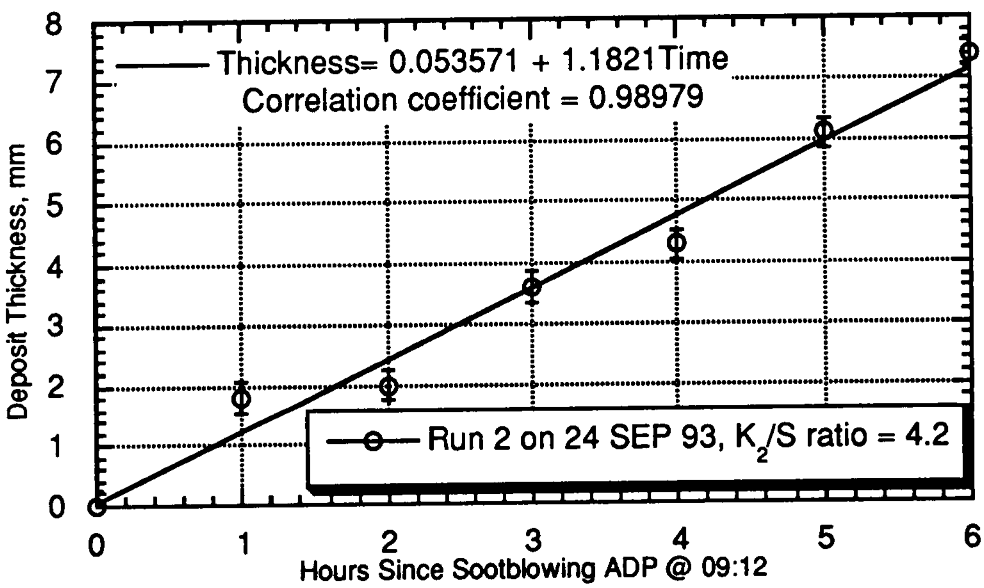

Figure 5.4 Measurement of ADP Ash Deposition Thickness for Run 2

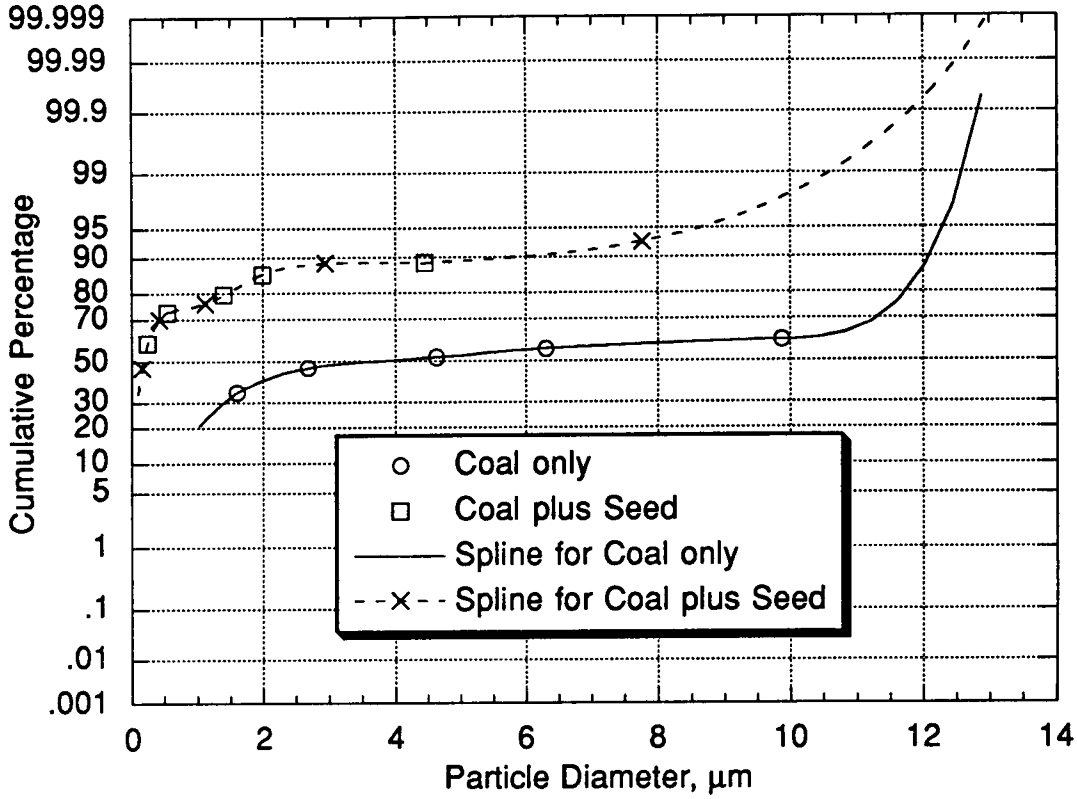

Figure 5.5 Particle Size Distributions of Fly Ash from Five-Stage Cyclone Data for MHD Samples While Burning Montana Rosebud Coal

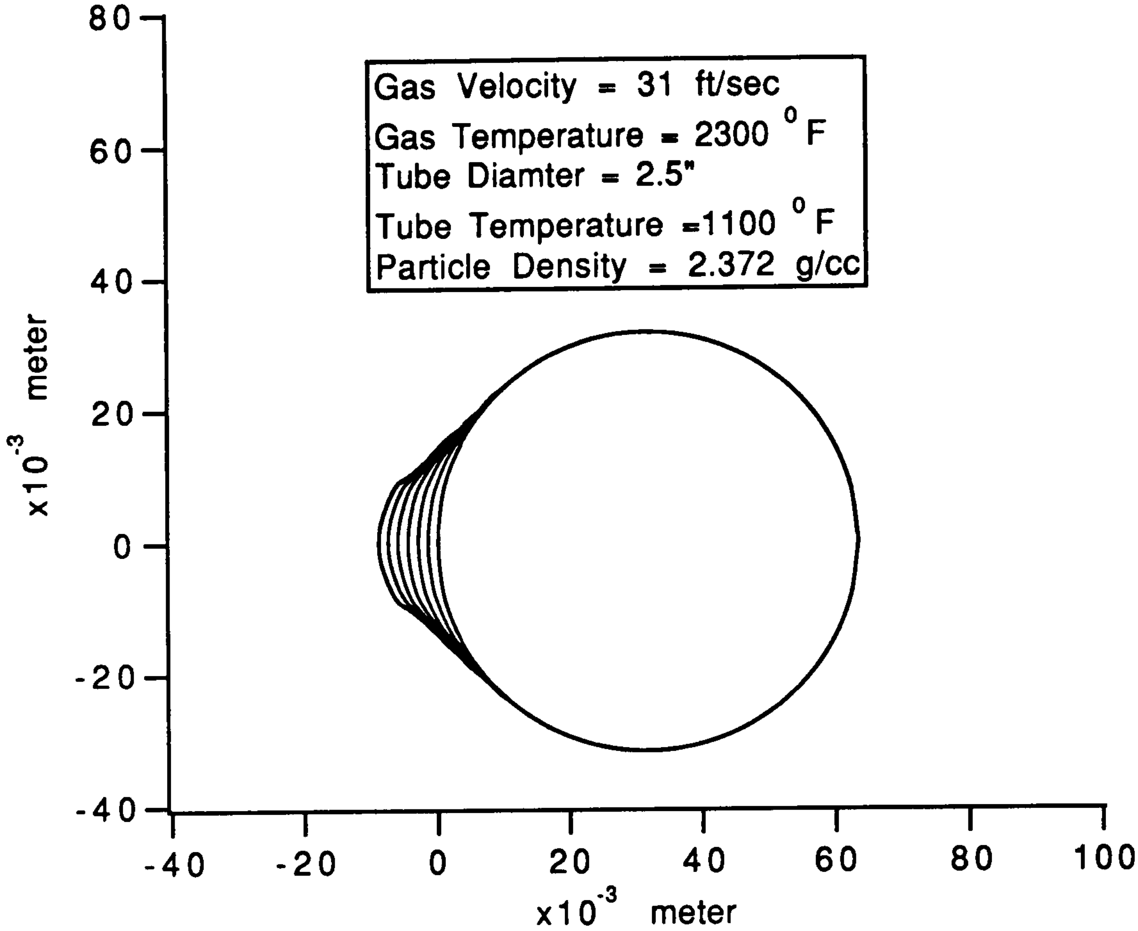

Figure 5.6 Calculated Deposit Growth on Clean ADP Tube Shown with One Hour Time Steps for Montana Rosebud Coal Plus Seed for Run 2

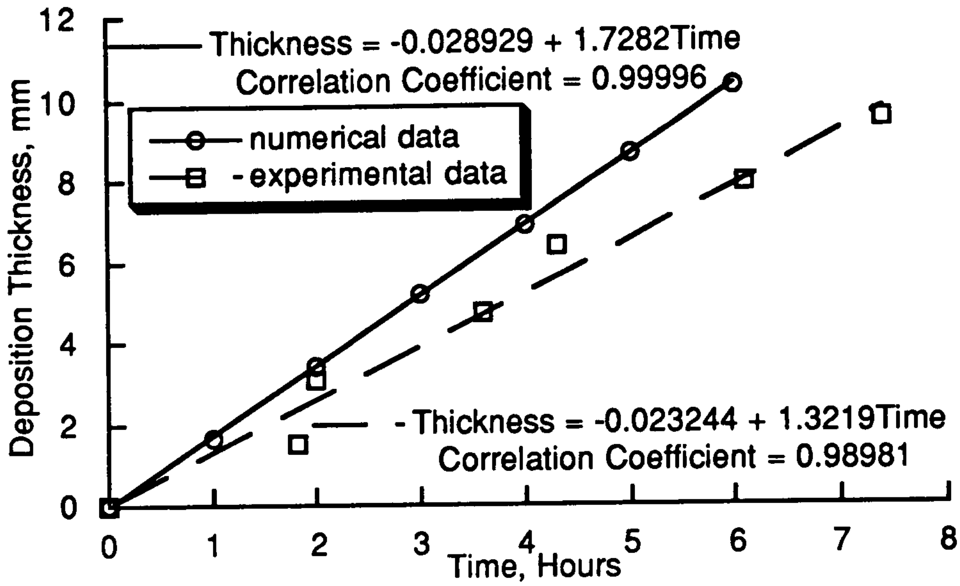

Figure 5.7 Thickness Comparison of Ash Deposition on ADP for Run 2

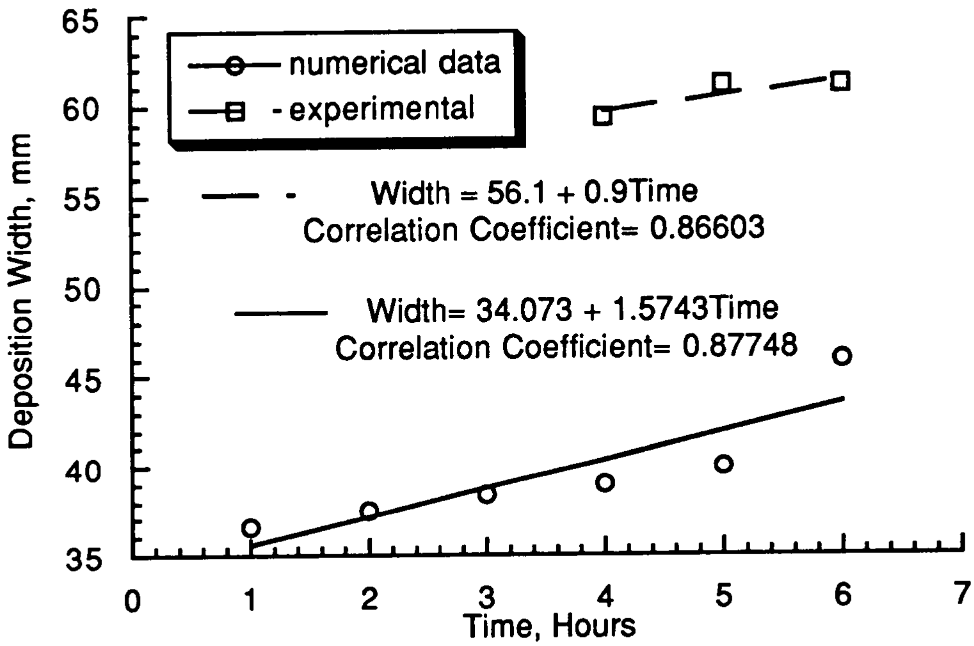

Figure 5.8 Width Comparison of Ash Deposition on ADP for Run 2

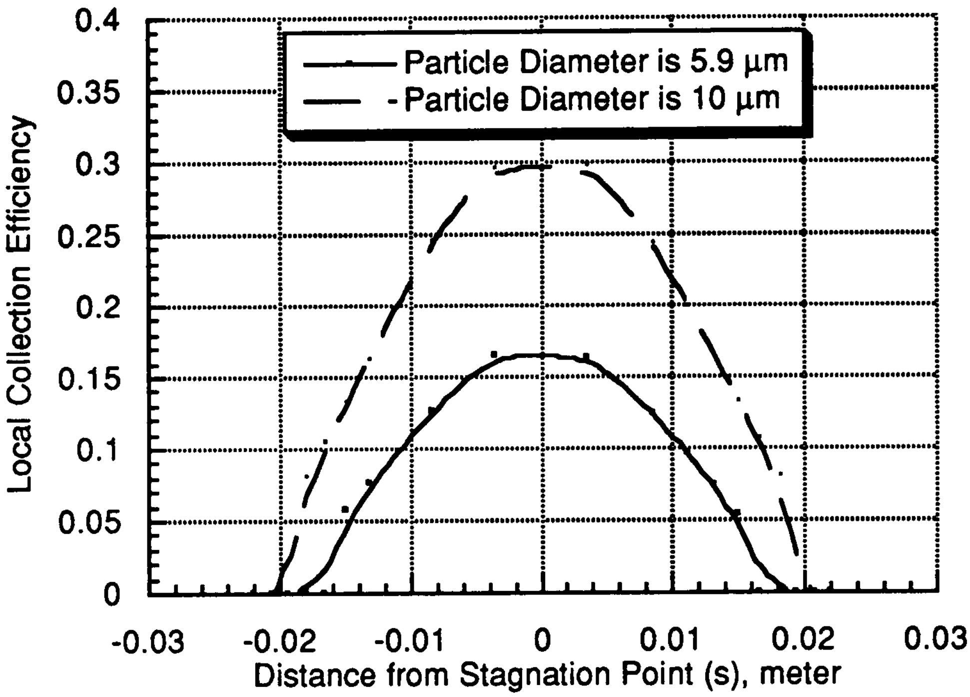

Figure 5.9 The Local Collection Efficiency of Particles on Clean 2.5" Diameter ADP Tube for Run 2

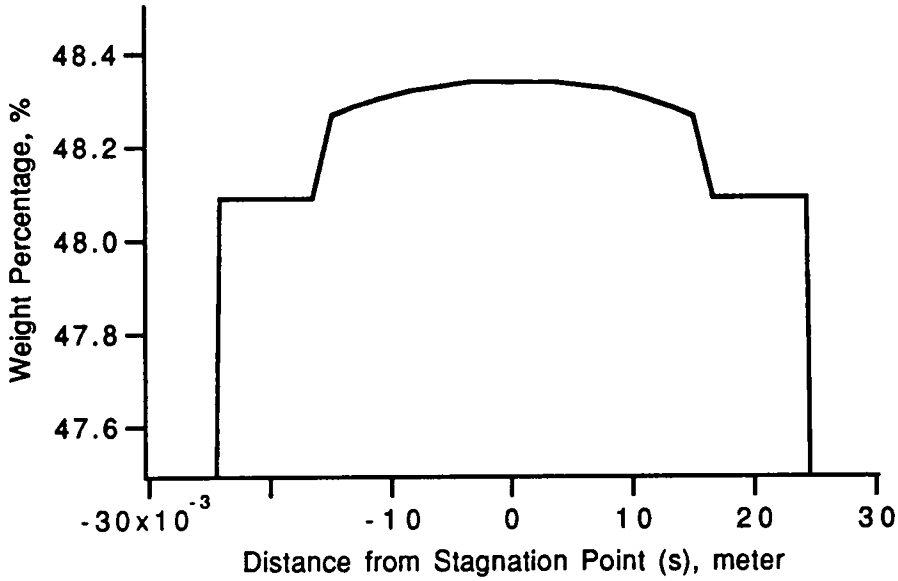

a. K_2O Distribution

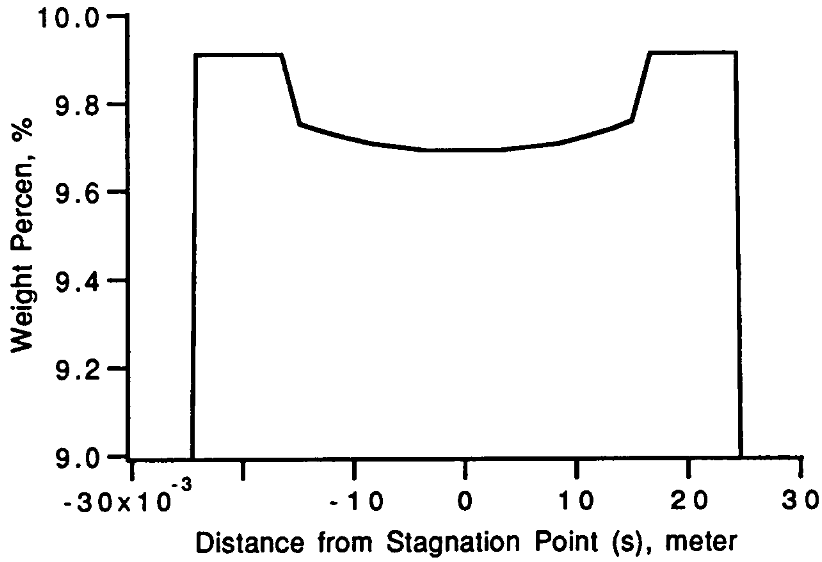

b. SiO_2 Distribution

Figure 5.10 The Distribution of Specific Chemical Species around Tube

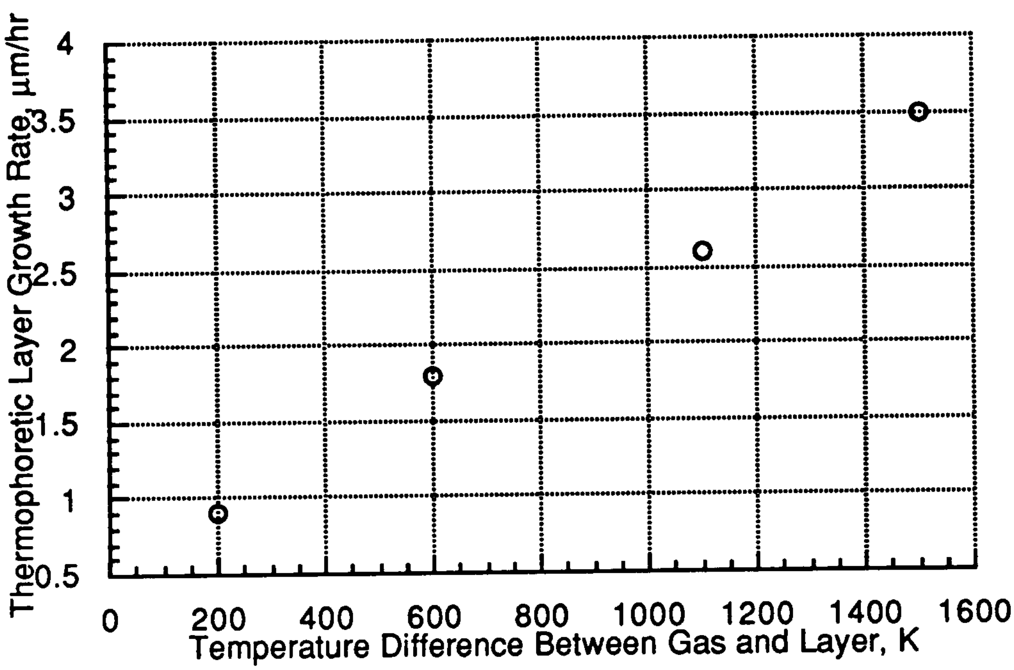

Figure 5.11 Thermophoretic Layer Growth Rate on the ADP Tube vs. Temperature Difference Between the Gas and Tube Surface

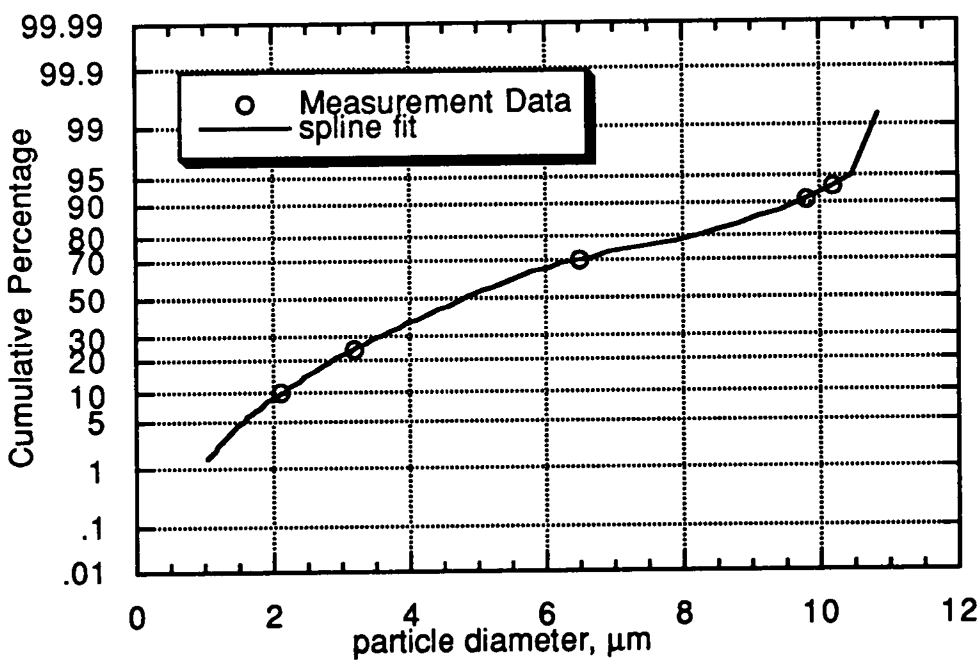

Figure 5.12 Particle Size Distribution of Fly Ash from Leeds & Northrup MICROTRAC Data for PETC Fuels Evaluation Facility with Gas Firing and Al_2O_3 Particle Injection

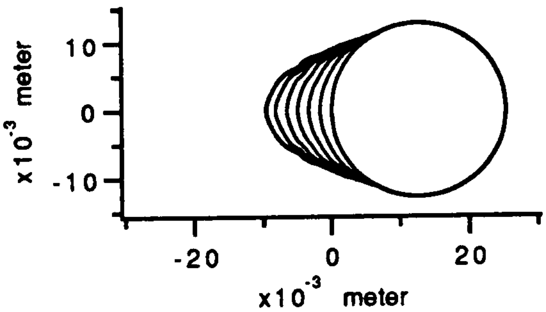

a. Dust Loading from Isokinetic Sample, 2.5 lb/hr

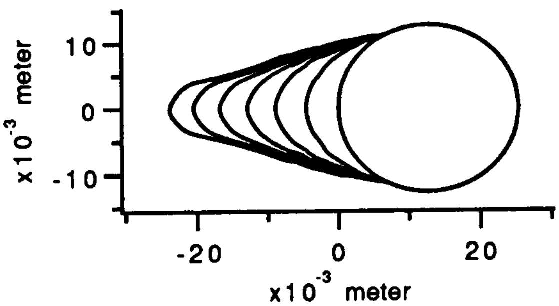

b.Dust Loading from Injection Rate. 4.1 lb/hr

Figure 5.13 Effect of Dust Loading of Refractory Al_2O_3 Particles Injected into the Flue Gas, while Burning Natural-Gas in the PETC Fuels Evaluation Facility, for the First-Hour Period

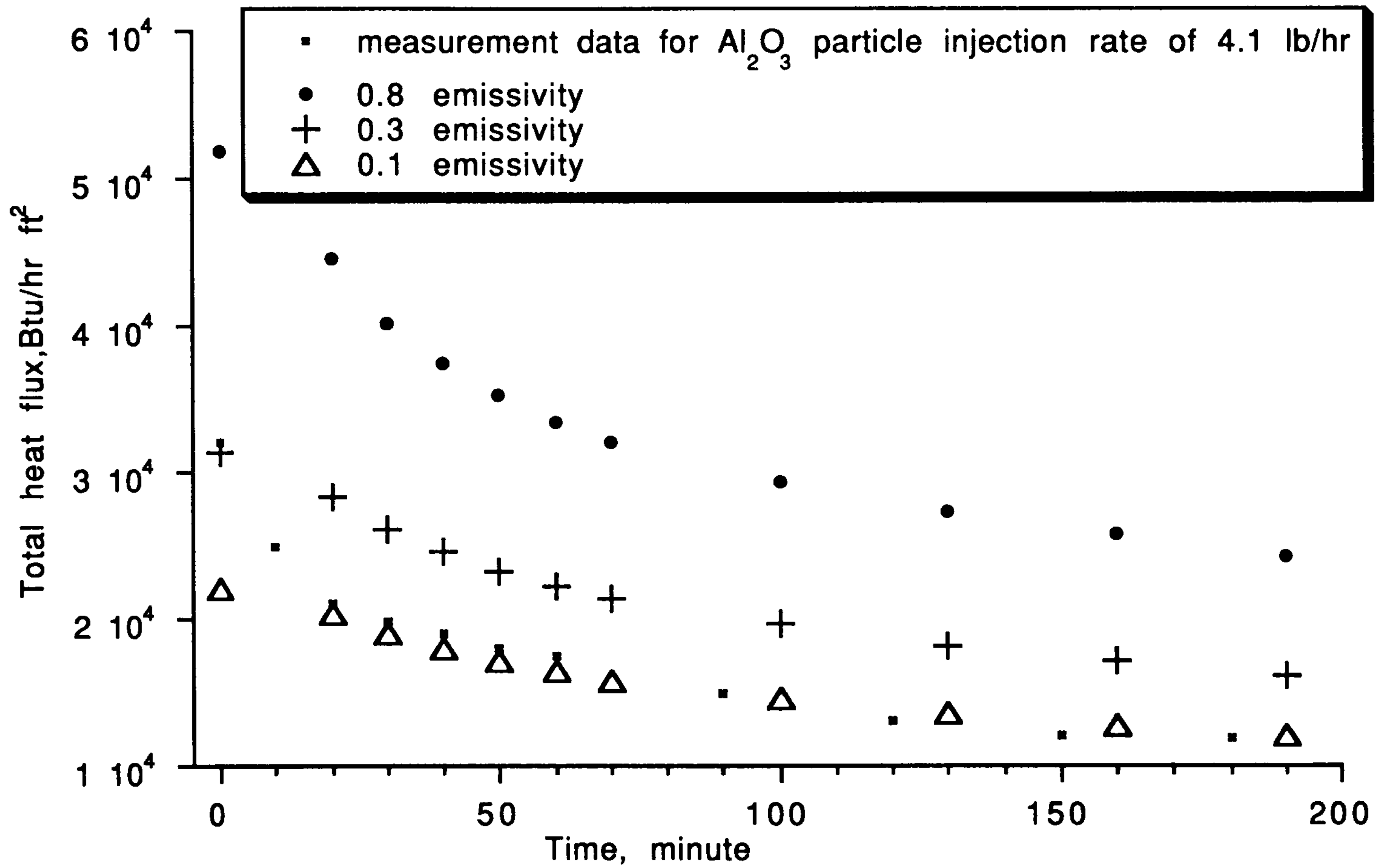

Figure 5.14 Effect of Thermophoretic Layer Emissivity on Predicted Total Heat Flux (no Inside Scale), Compared to Experiment

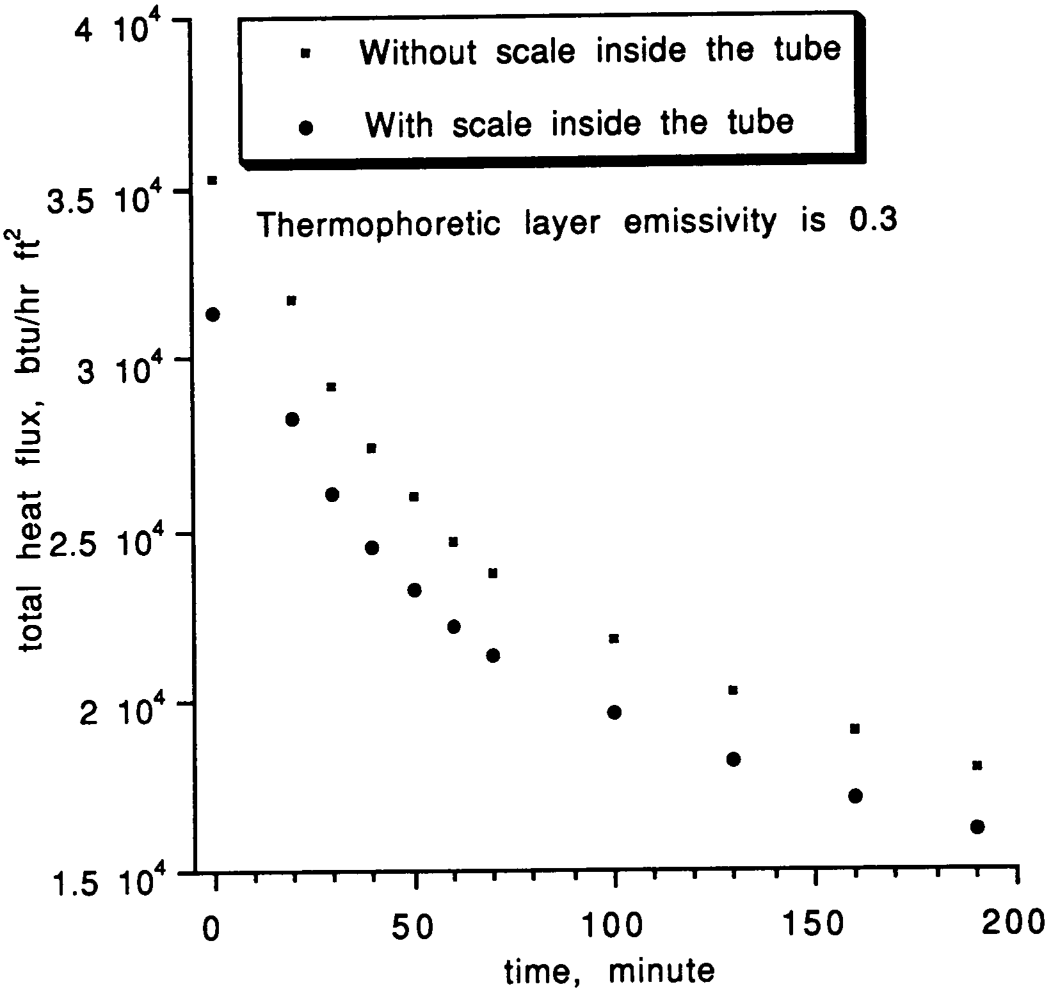

Figure 5.15 Effect of Thin Internal Film Scale on Predicted Total Heat Flux, for PETC Air-Cooled Deposition Probe

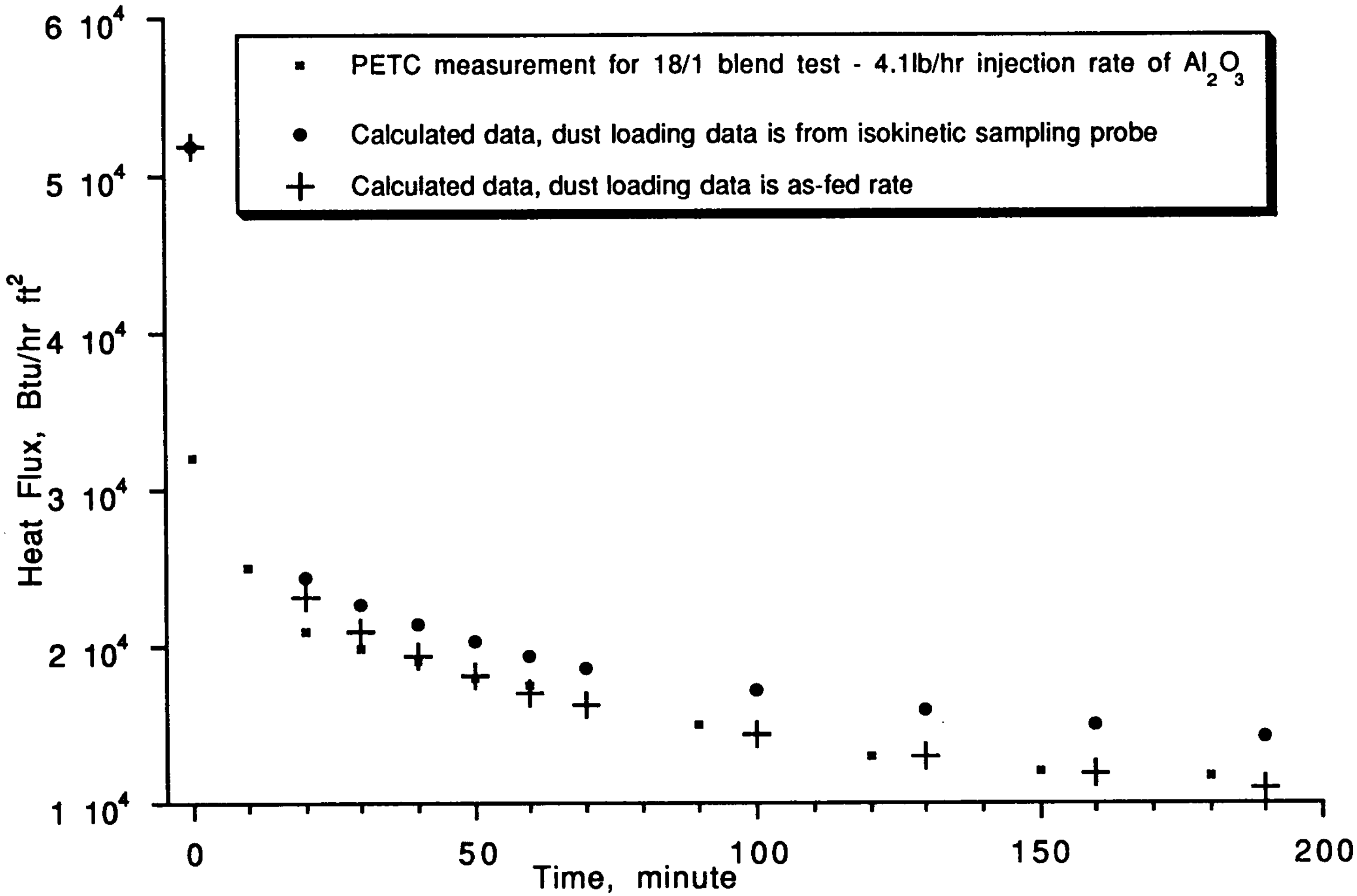

Figure 5.16 Comparison of Calculated and Measured Total Heat Flux for PETC FEF Test

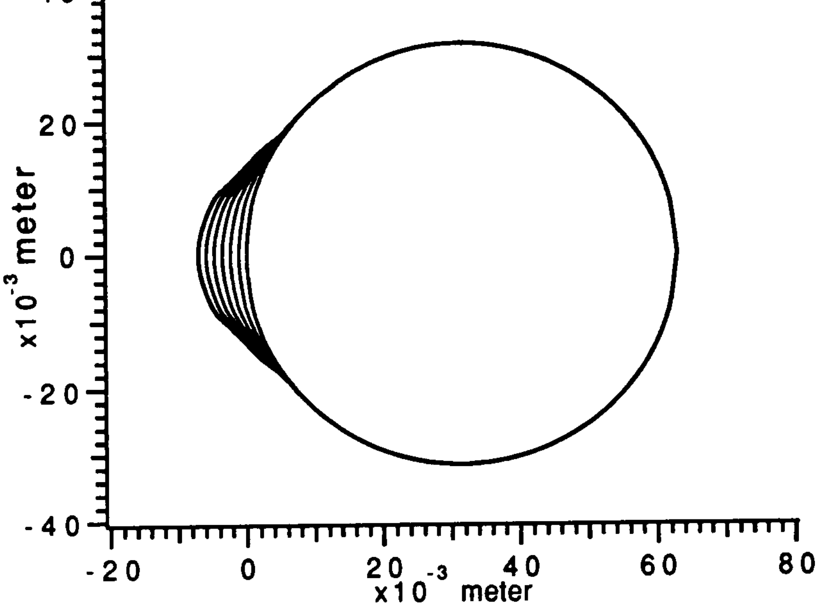

Figure 5.17 Calculated Growth of Ash Deposition Shape Starting with an Initially Clean CS3 Tube Based on One-Hour Time Steps

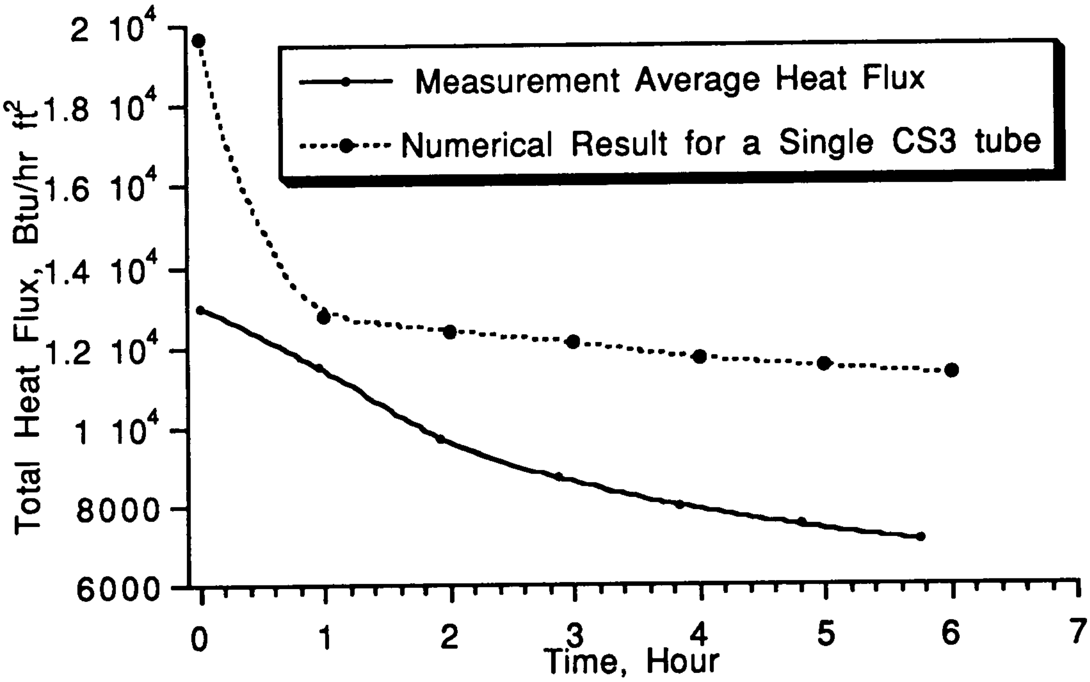

Figure 5.18 Comparison of Predicted and Measured Average Total Heat Flux for a Single CS3 Tube

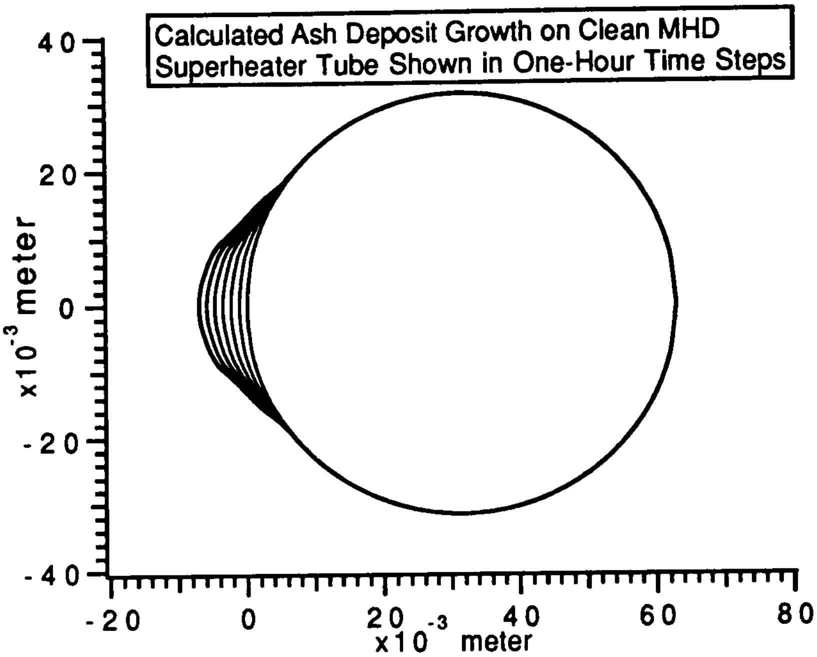

(a) 6.1 m/s gas velocity (20ft/s)

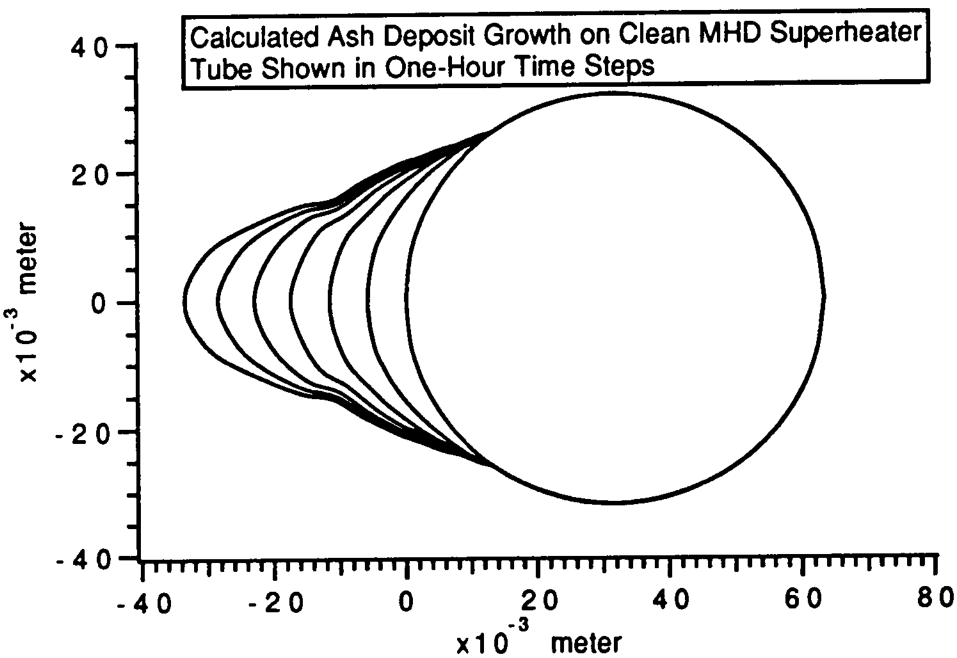

(b) 18.3 m/s gas velocity (60ft/s)

Figure 5.19. Effect of Gas Velocity on Ash Deposition during Six-Hour Period

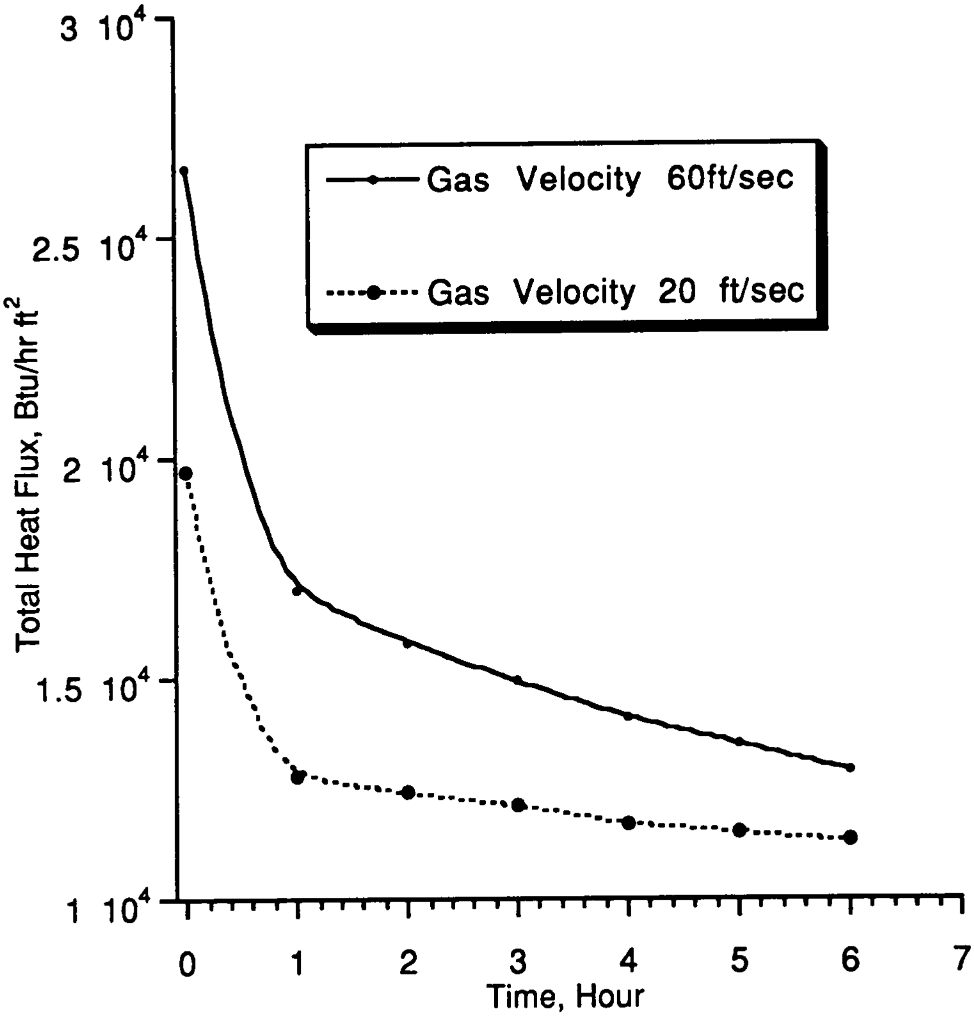

Figure 5.20 Effect of Gas Velocity on Calculated Total Heat Flux during Six-Hour Period

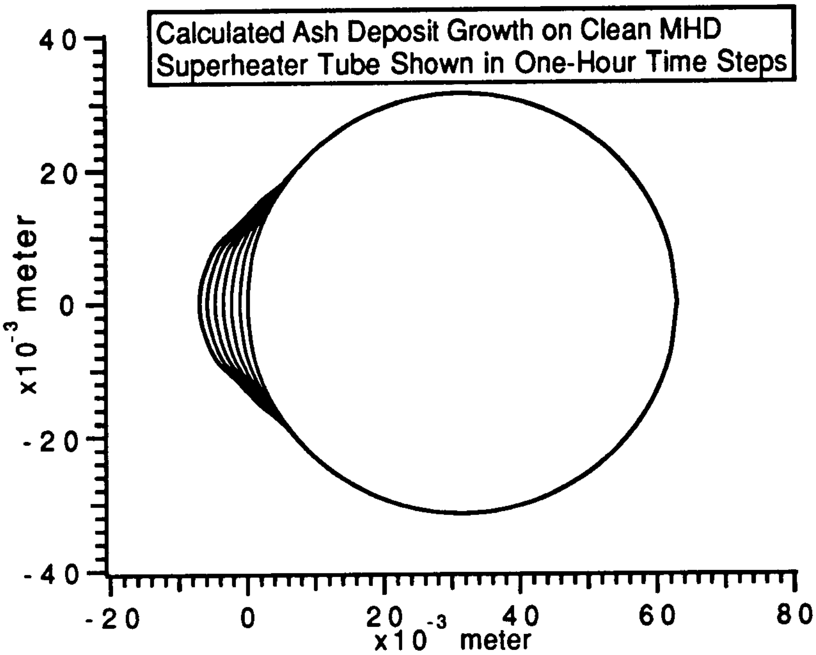

(a). Tube diameter is 2.5"

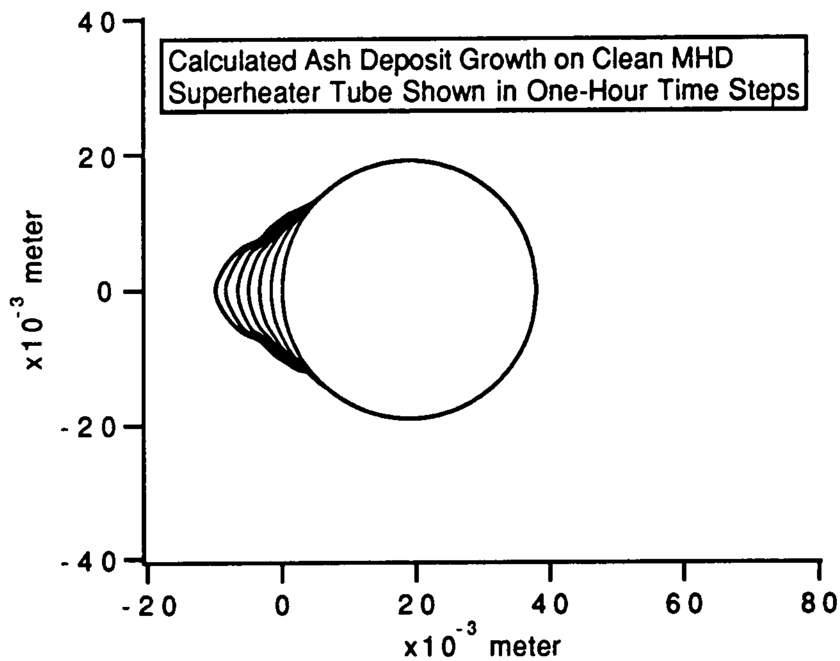

(b) Tube Diameter is 1.5"

Figure 5.21. Effect of Tube Diameter on Ash Deposition during Six-Hour Period

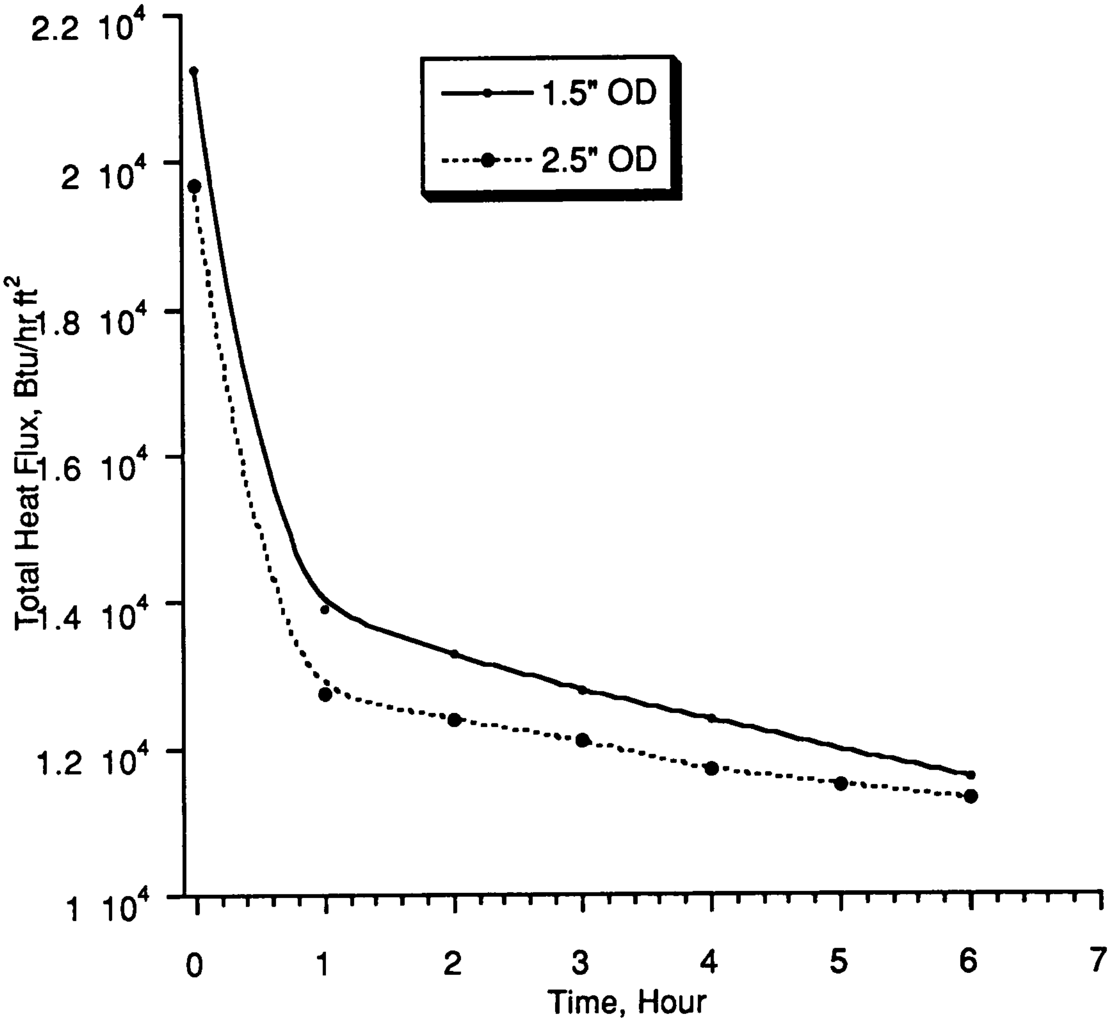

Figure 5.22 Effect of Tube Diameter on Calculated Total Heat Flux during Six-Hour Period

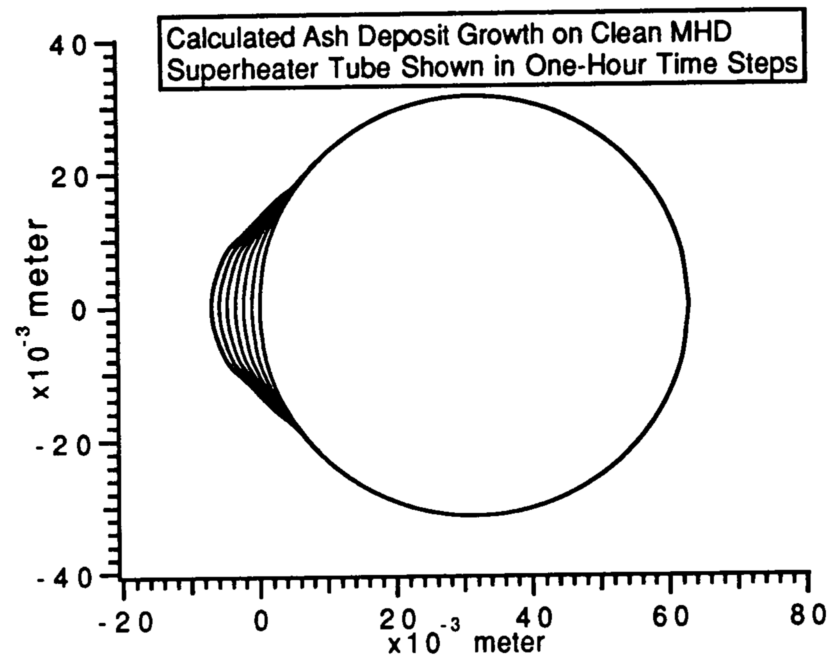

(a). Particle Density is 2.372 g/cc

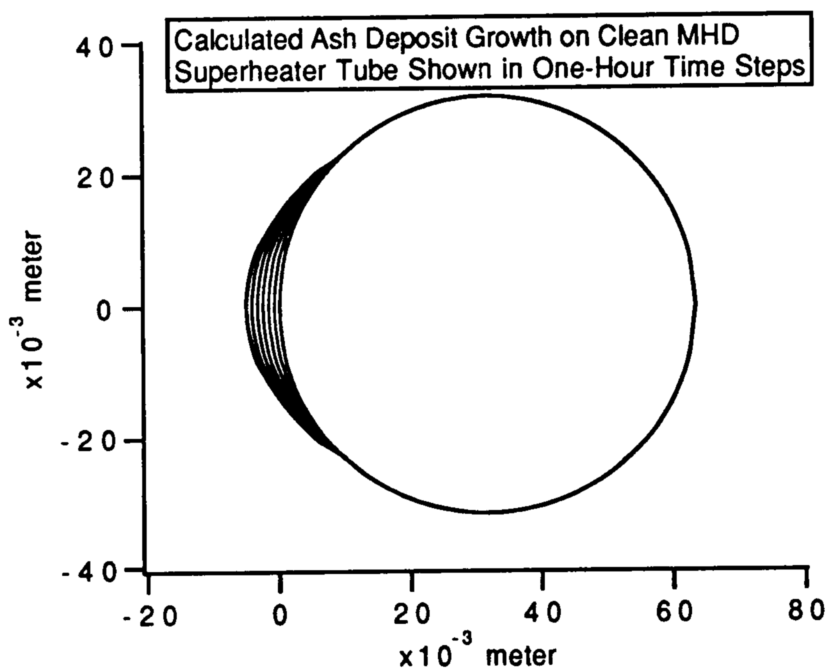

(b) Particle Density is 5.18 g/cc

Figure 5.23 Effect of Particle Density on Ash Deposition during Six-Hour Period

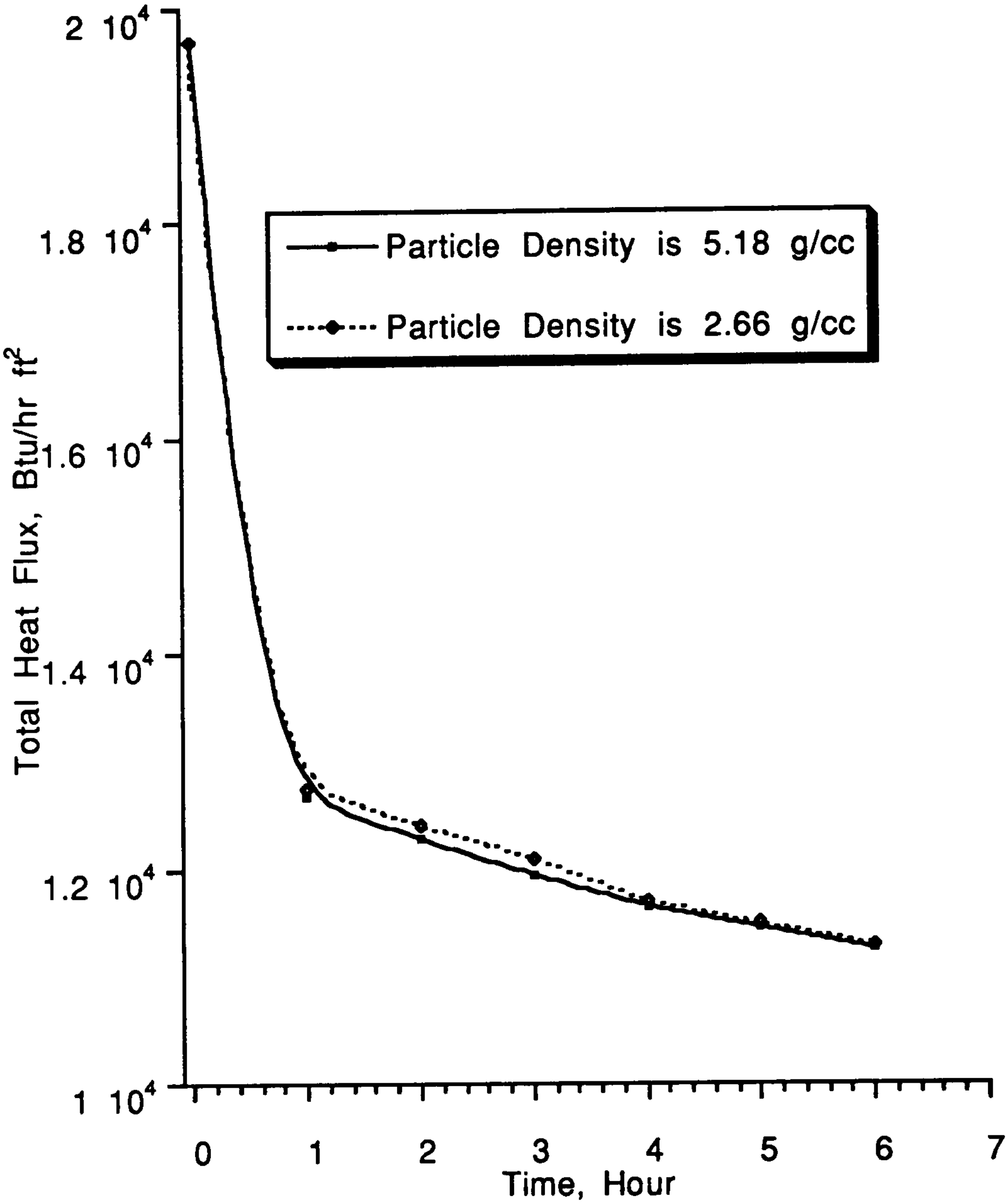

Figure 5.24 Effect of Particle Density on Calculated Total Heat Flux during Six-Hour Period

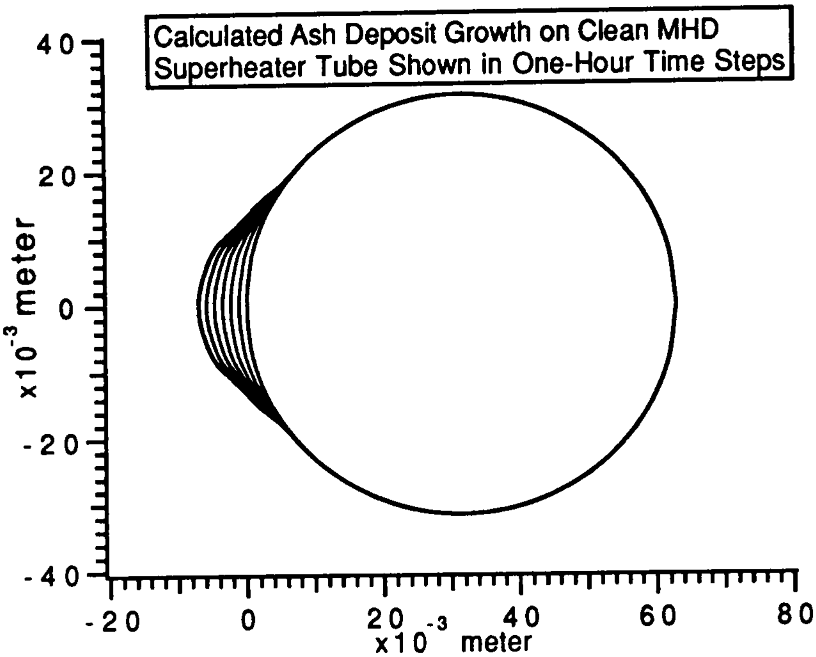

(a) Montana Rosebud coal plus seed.

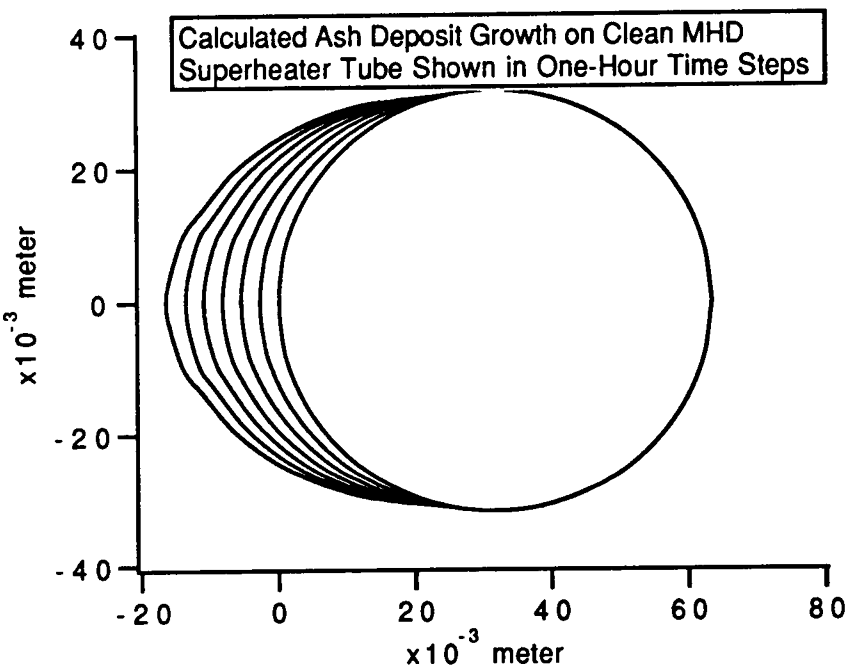

(b) Montana Rosebud coal only.

Figure 5.25 Effect of Particle Size Distribution on Ash Deposition during Six-Hour Period

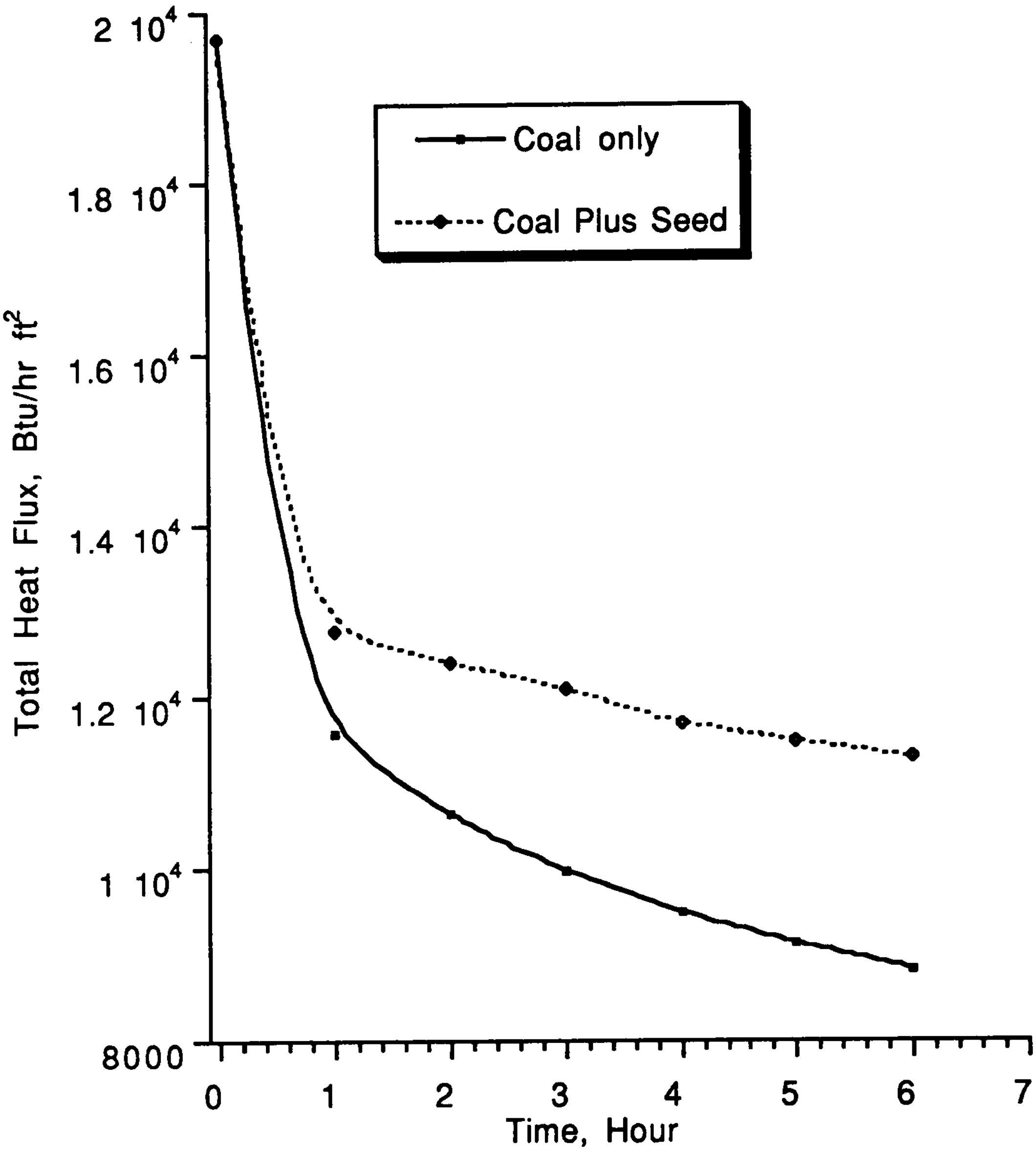

Figure 5.26 Effect of Particle Size Distribution on Calculated Total Heat Flux during Six-Hour Period

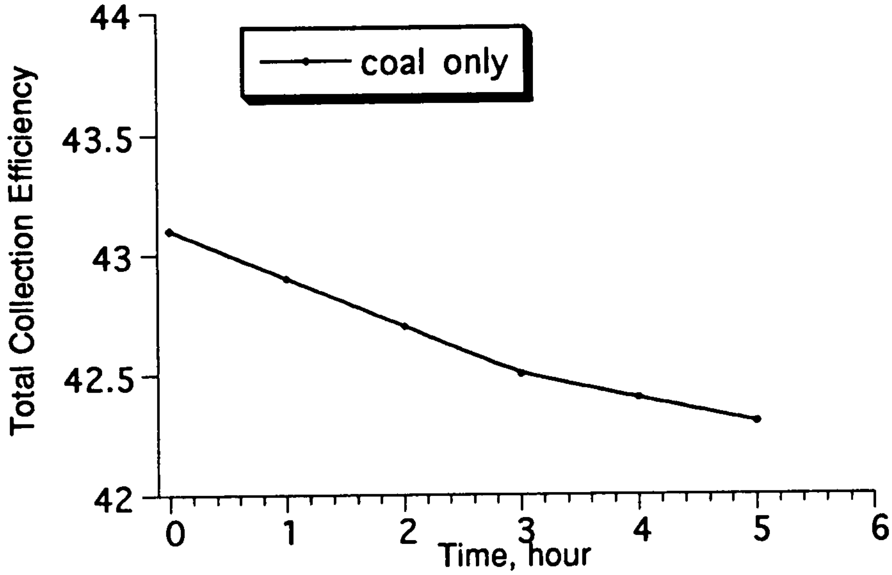

a. Total collection Efficiency for MHD Test Burning Coal only

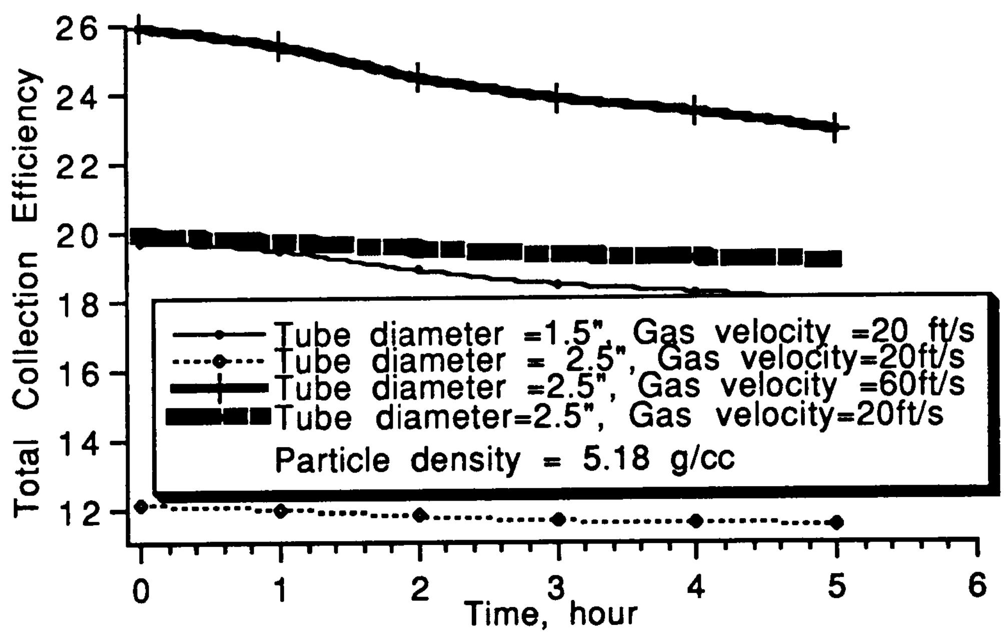

b. Total Collection Efficiency for MHD Test Burning Coal Plus Seed

Figure 5.27 Calculated Total Collection Efficiency of Superheater Tubes as a Function of Test Time and Tube Diameter, Based on Experimental Particle Size Distributions from UTSI CFFF Tests

VITA

Xiaoxiong Yan was born on January 17, 1962 in Chengdong, Sichen Province, P. R. CHINA. He grew up in Beijing and graduated from Dongzhimen High School in July 1980 and entered The University of Science and Technology of China in Hufei, Anhui Province the same year. In June 1985 he received a Bachelor of Science degree in Engineering Thermophysics. From August 1985 to July 1987, he worked in the Institute of Engineering Thermophysics in Beijing as a research engineer.

Mr. Yan came to the United States in August 1987 and entered the University of Notre Dame on a Teaching Assistantship with the Department of Mechanical Engineering. In the summer of 1989, he received a Master of Science degree. He then entered the University of Tennessee Space Institute on a Graduate Research Assistantship with the Energy Conversion Research and Development Programs. In May 1994, he received a Doctor of Philosophy degree from the University of Tennessee.